Titre: Improving the Accuracy of Nonlinear Potential Flow Methods for
Title: Aeronautical Applications

Auteur: Charles Le Pailleur
Author:

Date: 2025

Type: Mémoire ou thèse / Dissertation or Thesis

Référence: Le Pailleur, C. (2025). Improving the Accuracy of Nonlinear Potential Flow Methods for Aeronautical Applications [Mémoire de maîtrise, Polytechnique Montréal]. PolyPublie. https://publications.polymtl.ca/68726/
Citation:

URL de PolyPublie: https://publications.polymtl.ca/68726/
PolyPublie URL:

Directeurs de recherche: Éric Laurendeau
Advisors:

Programme: Génie mécanique
Program:

POLYTECHNIQUE MONTRÉAL
affiliée à l'Université de Montréal

Improving the Accuracy of Nonlinear Potential Flow Methods for Aeronautical Applications

CHARLES LE PAILLEUR
Département de génie mécanique

Mémoire présenté en vue de l'obtention du diplôme de *Maîtrise ès sciences appliquées*
Génie mécanique

Août 2025

POLYTECHNIQUE MONTRÉAL
affiliée à l'Université de Montréal

Ce mémoire intitulé :

Improving the Accuracy of Nonlinear Potential Flow Methods for Aeronautical Applications

présenté par **Charles LE PAILLEUR**
en vue de l'obtention du diplôme de *Maîtrise ès sciences appliquées*
a été dûment accepté par le jury d'examen constitué de :

Roberto PAOLI, président
Éric LAURENDEAU, membre et directeur de recherche
Matthieu PARENTEAU, membre

DEDICATION

À ma famille et mes amis…

ACKNOWLEDGEMENTS

First and foremost, I would like to give my thanks to Professor Eric Laurendeau for giving me the opportunity of working in his lab as well as for putting the well-being of his students first. His unwavering dedication to both my academic growth and industrial development allowed me to participate in a five-month internship at *Airbus Canada Limited Partnership* and a once-in-a-lifetime four-month experience in the city of *Toulouse, France*, where I had the opportunity to work at *Airbus Operations SAS*. Thank you for believing in my abilities and for your valuable advices.

I also give my thanks to François Bisson, Frédéric Plante, William Thollet and the whole team of Airbus Canada as well as to Xavier Bertrand and his colleagues of Airbus Operations for your welcome, time, expertise and guidance during my time within your respective work groups. It truly was a unique experience that would not have been possible without your efforts.

I want to thank my colleagues and friends at the lab: Baptiste, Guillaume, Justin, Karim, Lauren, Pablo, Samuel, Simon, Vincent... The technical nature of our subjects made you the only people who truly understood my daily rants, struggles and victories.

I would like to thank my family and friends who supported me through the ups and downs of my research project. Your encouragement is what kept me going through the various challenges I had to face during the past two years.

And finally, I would like to thank my partner, Colombe, who provided me with the best support I could have hoped for, even when separated by an ocean and multiple time zones. Thank you for your patience, your guidance and for your unconditional love.

This work would not have been possible without the financial support of *Le Fonds de Recherche du Québec en Sciences Naturelles et Génie* (FRQNT) and the *Mitacs* organization.

RÉSUMÉ

La modélisation de la performance aérodynamique des aéronefs demeure un domaine de recherche en constante évolution, soutenu par le développement continu de nouvelles méthodes numériques en mécanique des fluides. Parmi celles-ci, les approches dites haute fidélité, telles que les simulations basées sur la famille de modèles Reynolds-Averaged Navier-Stokes (RANS), se distinguent par leur grande précision. Toutefois, leur coût computationnel demeure à ce jour un facteur limitant, ce qui les rend peu propices pour le design préliminaire où plusieurs centaines voir milliers d'itérations de design sont analysées. À l'opposé, les méthodes basse fidélité reposent sur des hypothèses simplificatrices qui réduisent la précision des résultats, mais offrent une rapidité d'exécution supérieure de plusieurs ordres de grandeur. Entre ces deux extrêmes se trouvent les approches dites moyenne fidélité, qui visent à offrir un compromis entre précision et performance.

Parmi les méthodes à fidélité moyenne prometteuses figurent les modèles d'écoulement potentiel non linéaire, lesquelles ont démontré leur efficacité tant dans le milieu académique qu'industriel, produisant des résultats cohérents avec les simulations RANS et les essais en soufflerie. Ce présent travail s'appuie sur ces approches dans le but ddans le but de développer une méthode moyenne fidélité permettant l'analyse de configurations avion générales et complexes, avec un niveau de précision comparable à celui des méthodes RANS.

La méthode proposée repose sur le Nonlinear Vortex-Lattice Method (NL-VLM), permettant de capturer les principaux effets non linéaires. Elle s'appuie sur une base de données issue de simulations RANS 2.5D réalisées sur des sections d'aile prenant en compte les effets de flèche, ensuite couplées avec le solveur potentiel. Les effets du fuselage et des nacelles sont modélisés à l'aide d'une méthode des panneaux, tandis que les effets visqueux sont introduits à l'aide de corrections semi-empiriques. L'influence de surfaces portantes auxiliaires, telles que les empennages ou les supports, est également prise en compte. Une vérification des différentes composantes du solveur est présentée, et sa validation est effectuée sur plusieurs configurations du modèle Common Research Model (CRM) de la NASA, dans le cadre des ateliers Fifth High-Lift Prediction Workshop (HLPW5) et Sixth Drag Prediction Workshop (DPW6). Les résultats démontrent que cette approche est capable de reproduire les principaux effets non linéaires associés aux configurations complexes, bien que certaines limitations soient identifiées et discutées.

Dans un second temps, une tentative d'intégration des effets de l'effilement dans le processus de génération de la base de données RANS est proposée. Ce développement, fréquemment désigné comme méthode 2.75D, repose sur l'hypothèse d'une distribution radiale constante de l'écoulement, et s'appuie pour cela sur une discrétisation des équations d'Euler en coordonnées sphériques. Bien que la méthode permette de retrouver les cas limites attendus, elle présente des limites physiques importantes pour les ailes à fort effilement.

Enfin, une discussion sur le potentiel d'intégration de cette méthode dans un contexte industriel est proposée, et les limitations de celle-ci sont exposées.

ABSTRACT

The assessment of the aerodynamic performance of aircraft remains an active area of research, driven by the continued development of numerical methods in fluid mechanics. Among them, high-fidelity approaches such as the Reynolds-Averaged Navier-Stokes (RANS) family of solvers stand out for their high accuracy. However, their computational cost remains so significant that such methods still are inadequate for preliminary design endeavors, where several hundreds or even thousands of design iterations are performed. At the other end of the spectrum, low-fidelity methods rely on simplifying assumptions that affect accuracy, yet offer execution speeds several orders of magnitude faster. In between the two are medium-fidelity methods, which aim to balance accuracy with computational efficiency.

A promising class of medium-fidelity approaches is based on nonlinear potential flow models, which have demonstrated successful application in both academic and industrial contexts, yielding results consistent with RANS simulations and wind tunnel experiments. Building on these methods, the present work proposes a medium-fidelity framework for analyzing complex and general aircraft configurations, targeting a level of accuracy comparable to RANS.

The proposed method is based on the Nonlinear Vortex-Lattice Method (NL-VLM), which introduces key nonlinear effects into the solution process. A database of 2.5D RANS simulations taking the effects of sweep into account is generated for discrete wing sections and coupled with the potential solver. The aerodynamic effects of the fuselage and nacelles are modelled using a panel method, while viscous effects are introduced through semi-empirical corrections. The inclusion of auxiliary lifting surfaces, such as empennages and wing pylons, is also investigated. Each solver component is individually verified, and validation is performed on multiple NASA Common Research Model (CRM) configurations from the Fifth High-Lift Prediction Workshop (HLPW5) as well as the Sixth Drag Prediction Workshop (DPW6). The results demonstrate that medium-fidelity methods can capture most major nonlinear effects of complex configurations, though certain limitations remain are discussed thereafter.

Secondly, the integration of taper effects into the RANS database generation process is explored. This extension, referred to as the 2.75D method, assumes a constant radial flow distribution and discretizes the Euler equations in spherical coordinates. While the method recovers the expected limiting cases, its underlying assumptions lead to physical inaccuracies for highly tapered wings.

Finally, the possible applications of this framework within industrial context is discussed, and the limitations of the proposed methodology are highlighted.

TABLE OF CONTENTS

LIST OF TABLES

LIST OF FIGURES

LIST OF SYMBOLS AND ACRONYMS

ACRONYMS

ROM Reduced Order Model

CFD Computational Fluid Dynamics

DNS Direct Numerical Simulation

LES Large-Eddy Simulation

WMLES Wall-Modeled Large-Eddy Simulation

RANS Reynolds-Averaged Navier-Stokes

VLM Vortex-Lattice Method

LLM Lifting-Line Method

TAT Thin Airfoil Theory

PG Prandtl-Glauert Transformation

NL-VLM Nonlinear Vortex-Lattice Method

AIC Aerodynamic Influence Coefficient

JIT Just-In Time

MDO Multi-Disciplinary Optimization

BRW Bombardier Research Wing

CRM Common Research Model

PDE Partial Differential Equation

SFD Selective Frequency Damping

WLS Weighted Least-Square

SA Spalart-Allmaras

HPC High-Performance Computing

HLPW5	Fifth High-Lift Prediction Workshop
DPW6	Sixth Drag Prediction Workshop
HTP	Horizontal Tail Plane
VTP	Vertical Tail Plane
FTF	Flap Track Fairing
WB	Wing-Body
WBH	Wing-Body-HTP
WBHV	Wing-Body-HTP-VTP
WBSHV	Wing-Body-Slat-HTP-VTP
WBHNP	Wing-Body-HTP-Nacelle-Pylon

CHAPTER 1 INTRODUCTION

Despite a nearly eight-fold improvement in air transport efficiency over the past six decades, the aerospace industry has committed to reducing its environmental impact by 50% in accordance with the United Nations Convention on Climate Change [1]. In this regard, the improvement and development of new aircraft designs plays a key role in the quest for better overall efficiency. However, the inherent complexity of aerodynamic numerical models makes the analysis of complex aircraft configurations challenging, especially in preliminary design endeavors where thousands of design iterations are performed. Hence, a compromise on fidelity/accuracy and computational cost is often necessary to achieve fast turnaround time as well as to have enough confidence in the true performance of the generated designs.

An effective way of reducing the computational cost of a numerical method is to construct a Reduced Order Model (ROM) via the introduction of a set of idealized simplifying hypotheses. These hypotheses are constructed by neglecting behaviors that have low to no effects on the solution of the underlying physical law. Nonlinear effects are often selected as such as they are generally more expansive to evaluate in a numerical context. Aircraft aerodynamics is a tightly coupled field of engineering that involves several physical models, phenomena and geometries. Consequently, the choice of adequate simplifying hypotheses is critical for a successful physics-based ROM.

This research aims to assess the nonlinear behavior of a specific subset of ROMs used in aircraft aerodynamics: nonlinear potential flow methods.

1.1 Definition of Basic Concepts

1.1.1 Computational Fluid Dynamics

Computational Fluid Dynamics (CFD) describes the study of the behavior of fluids via the direct application of physical laws to a given problem. More specifically, the physical laws dictating the behavior of homogenous fluids are the Navier-Stokes Equations. They are generally expressed as conservation laws taking the form of a system of three Partial Differential Equations (PDEs), that is the conservation of mass, momentum, and energy.

$$\begin{cases} \frac{\partial \rho}{\partial t} + \nabla \cdot (\rho \mathbf{V}) = 0 \\ \frac{\partial \rho \mathbf{V}}{\partial t} + \nabla \cdot (\rho \mathbf{V} \otimes \mathbf{V}) + \nabla p - \nabla \cdot \tau = 0 \\ \frac{\partial \rho E}{\partial t} + \nabla \cdot (\rho \mathbf{V} H) - \nabla \cdot (\tau \cdot \mathbf{V}) = 0 \end{cases} \tag{1.1}$$

where the three primitive variables are the density of the fluid ρ, its velocity $\mathbf{V}$ and its pressure p. The nonlinear nature of the Navier-Stokes equations makes them almost always impossible to be solved analytically, except in extremely simplified and idealized conditions (e.g. Couette and Poiseuille flow). For more practical cases, they need to be solved numerically by subdividing the fluid continuum in a finite number of primitive elements. This step is denoted as *discretization* and results in a *mesh* of the simulation domain. Common numerical approaches for solving the Navier-Stokes equations are the Finite Difference, Finite Volume and Finite Element methods.

Computational Aerodynamics is defined as a subset of CFD where the studied fluid is generally a compressible fluid of low viscosity such as air. These two properties makes aerodynamic problems especially hard to solve, as they both tend to increase the occurrence of highly nonlinear phenomenons in the solution:

- **Shock Waves:** Apparition of sharp discontinuities in the solution field when the local velocity approaches the sonic point
- **Turbulence:** Apparition of strong and chaotic gradients in the solution field when inertial forces dominate over viscous forces

Thus, these phenomenons have to be properly included and modelled, creating additional computational overhead within the solution process.

1.1.2 Fidelity of Numerical Methods

The fidelity of a computational method is defined as its capacity to accurately produce solutions that are coherent with experimental data for given flow conditions. CFD methods are hierarchized into families depending on what simplifying hypotheses they include in their formulation. Figure 1.1 summarizes this hierarchy.

Navier-Stokes-Based Approaches

Direct Numerical Simulation (DNS) is the method with the highest fidelity level. As its name suggests, it solves the Navier-Stokes system directly without any additional assumption. For turbulent flows, DNS must solve turbulence on all scales, thus requiring prohibitively refined meshes (at the order of billions of unknowns). Combined with the unsteady and three-dimensional nature of turbulence itself, DNS is extremely expensive to evaluate and is currently inadequate for most common applications.

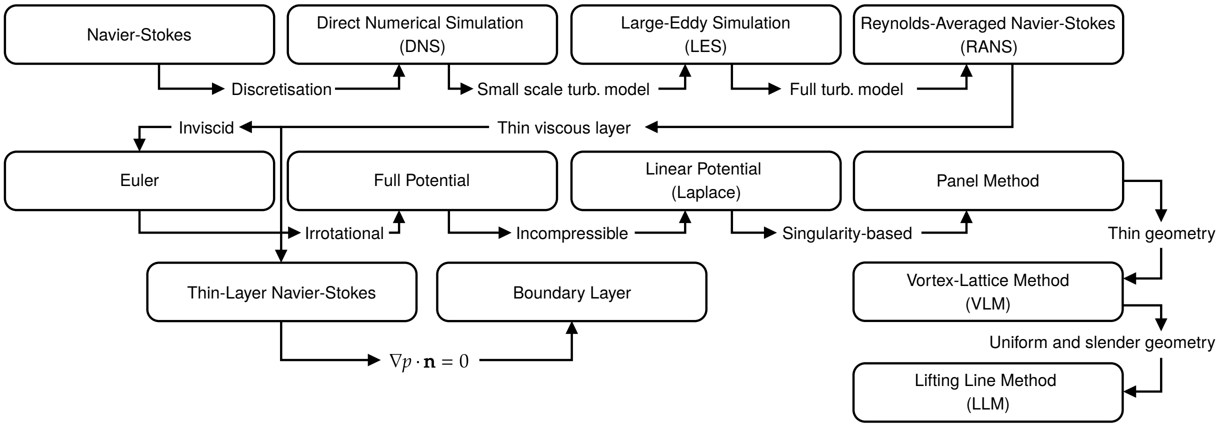

Figure 1.1 Hierarchy of the fidelity of numerical methods in Computational Aerodynamics

Instead of solving turbulence on all scales, Large-Eddy Simulation (LES) methods solves large scale turbulence in the same way as DNS while small scale turbulence is modelled using a closure/turbulence model. While becoming more accessible in recent years due to the availability of High-Performance Computing (HPC) resources, LES methods are still very expensive for high Reynolds number applications in aerodynamics and are yet unsuitable for rapid development.

Reynolds-Averaged Navier-Stokes (RANS) greatly reduces computational costs by solving only the mean flow, while chaotic perturbations due to turbulence are entirely modelled using a closure. RANS-based methods are quite accurate and provide more modest computational costs, and are therefore state-of-the-art methods for most aerodynamic applications. The success of a RANS simulation however still highly depend on mesh quality, which is generally a time-consuming, iterative and difficult task especially when complex and variable geometries are involved.

By completely neglecting viscosity, the Navier-Stokes system is reduced the Euler equations. A notable advantage of the Euler equations is that they obviate the need for supplementary modeling and, furthermore, the absence of thin shear layers yields significantly improved mesh conditioning, which in turn enhances convergence properties and reduces execution time. However, the effects of viscosity are most often non-negligible except for simple geometries at very low angles of attack.

Potential-Based Approaches

By assuming that the flow of interest has no vorticity, that is,

$$\omega \equiv \nabla \times \mathbf{V} = \mathbf{0} \tag{1.2}$$

the velocity field $\mathbf{V}(x, y, z)$ can be described by a scalar potential function $\Phi(x, y, z)$ where

$$\mathbf{V} = \nabla\Phi \tag{1.3}$$

By formulating the Euler equations in terms of the potential instead of (ρ,$\mathbf{V}$,p), the so-called Full Potential equations are obtained.

$$\frac{\partial \rho}{\partial t} + \nabla \cdot (\rho \nabla \Phi) = 0 \tag{1.4a}$$

$$\rho = \left[1 - \frac{\gamma - 1}{\gamma + 1}|\nabla\Phi|^2\right]^{1/(\gamma-1)} \tag{1.4b}$$

The potential formulation is highly efficient as it only requires the solution of a single scalar PDE instead of a system of two scalar and one vectorial equations. Furthermore, it is in compressible form with the hypothesis of isentropic flow, allowing the capture of weak shocks in the solution. Due to the absence of vorticity, all potential formulations do not intrinsically yield any lift force. However, by artificially prescribing a stagnation point at the trailing edge, the correct flow topology is recovered (Figure 1.2). This is known as the Kutta condition.

Lastly, if the flow is assumed fully incompressible ($\partial\rho/\partial t = 0$, $\nabla\rho = \mathbf{0}$), the Full Potential formulation reduces to the Laplace equation.

$$\nabla^2\Phi = 0 \tag{1.5}$$

The Laplace equation has the form of a *Poisson* equation and is therefore a linear homogenous PDE. Hence, according to the superposition theorem, the solution space can be represented as a superset of solutions to the Laplace equation.

$$\Phi^* = \sum_{i=1}^{N} \alpha_i \Phi_i \tag{1.6}$$

where Φ^* is the total potential, while Φ_i and α_i are elementary solutions and weights composing the global solution space. This fact alone allows the solution process to be performed using a linear combination of basic elementary solutions to model complex flow topologies.

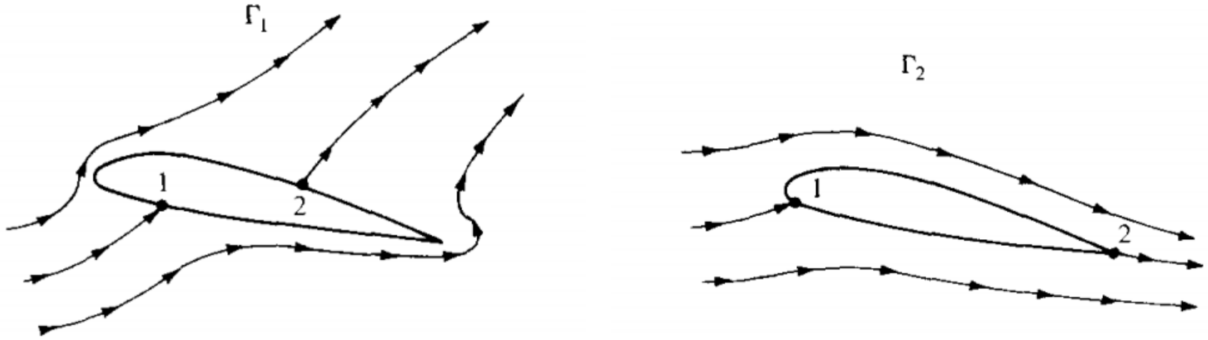

(a) Without Kutta condition (b) With Kutta condition at the trailing edge

Figure 1.2 Effect of the Kutta condition on the position of stagnation points and streamlines - [2]

This kind of approach is referred to as *singularity-based*, as the elementary solutions are perceived as singular perturbations in the flow:

$$\Phi^*(\mathbf{x}) = \Phi_\infty + \Phi(\mathbf{x}) \tag{1.7}$$

with Φ the perturbation potential caused by the presence of the aerodynamic body in the freestream flow Φ_∞. Linear potential flow methods are one of the fastest physics-based approaches in aerodynamic analysis due to their linear nature combined with the absence of volume/farfield meshes. They however are the lowest fidelity methods as they neglect critical physical nonlinear phenomena that appear throughout the flight envelope of most commercial aircraft.

Coupled Methods

Since the most computationally challenging phenomenons are due to viscous and compressibility effects, an effective way to limit the computational cost of a flow solver is to segregate highly nonlinear effects using a coupled approach. Since they involve some level of approximation, this kind of methods generally sits between Navier-Stokes-based and potential-based approaches in terms of accuracy.

Popular choices of coupled methods include:

- **Inviscid / Boundary Layer:** The computational domain is subdivided into a viscous region, at the boundary of the body, and an inviscid region around it. The viscous region is modeled with a Boundary Layer solver, while the inviscid region is modeled with an inviscid method. The coupling is done iteratively on the thickness of the boundary layer region.

- **Singularity-based Potential Flow / Sectional RANS:** Considering a sufficiently slender geometry, the latter can be discretized in a finite number of streamwise airfoil sections. Each section is thereafter modeled using higher-fidelity RANS simulations based on local flow properties determined by a fast three-dimensional potential flow solver. The coupling is done iteratively on the local load distribution (e.g. the local lift coefficient $Cl(y)$).

1.1.3 Dimensionality of the Navier-Stokes Equations

The Navier-Stokes equations are most commonly solved in three-dimensional or two-dimensional form. The former involves a 5×5 system of equations, whereas the latter involves a 4×4 system since the momentum perpendicular to the computational plane is uniformly zero. Other simplifications of a similar nature can be performed when flow quantities are assumed constant according to given conditions. For example, in the special case of the infinite swept wing, all primitive flow quantities are known to be constant along sweep lines. Hence, the three-dimensional Navier-Stokes equations can be reduced to a two-dimensional problem, while still involving five equations and unknowns to solve for. Since the infinite swept wing problem sits between a two-dimensional and a three-dimensional problem, this simplification is referred to as 2.5D. In addition to effects caused by sweep, one could also consider a series of geometrically similar (but of different chord lengths) wing sections in order to attempt to introduce taper into the simplified Navier-Stokes model. Techniques that incorporate tapering are often denoted as 2.75D methods, as they endeavor to approximate most of the original three-dimensional system with increased fidelity compared to 2.5D. A schematic representation of this hierarchical framework is provided in Figure 1.3.

1.2 Definition of the Problem

1.2.1 Preliminary/Conceptual Design

As the last sections suggest, the core challenge of preliminary design lies in the balance between fidelity and computational cost. Indeed, the necessity of generating several design configurations necessitates fast simulation execution times, lest the simulation process itself becomes a limiting factor in the design optimization workflow. Conversely, high-fidelity simulations are essential to ensure that the accuracy of the results does not impede decision-making.

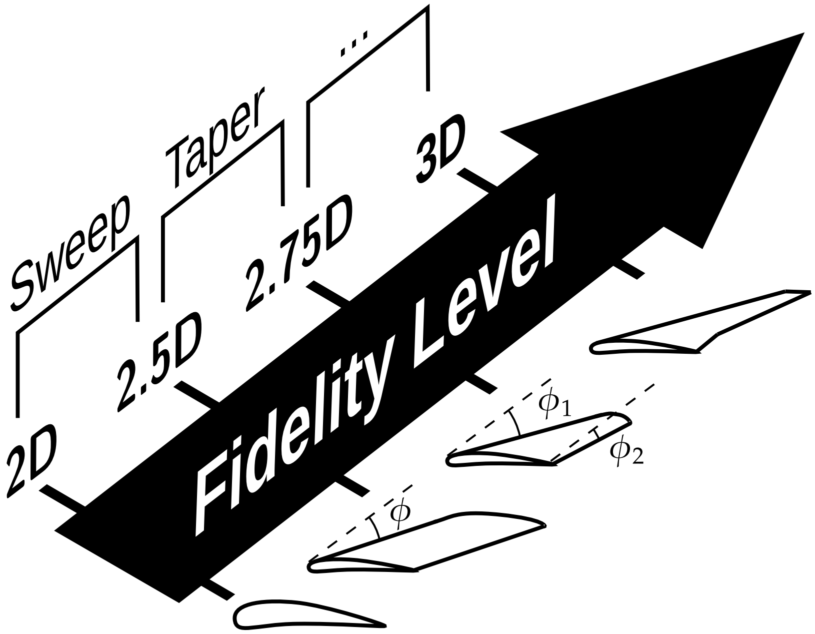

Figure 1.3 Dimensionality of the Navier-Stokes equations

Furthermore, several nonlinear multiphysics (aeroelasticity, maneuvers) and geometrical (wing-body and wing-tail interactions) effects are tightly coupled together. As a result, designing aircraft components separately is rarely an adequate option. Hence, the idea of a fast medium-fidelity method incorporating most of the components and behavior of the real aircraft is desirable. This allows for a fast turnaround time as it would provide a better understanding of the design configurations prior to the detailed design phases involving detailed three-dimensional simulations.

1.2.2 Multi-Fidelity Methodologies

Both high-fidelity and low-fidelity methods have distinct roles in the aircraft design process. The choice of the most appropriate method depends on the requisite level of detail and computational resources required and available at each stage. Combined, they unify the analysis process to form *multi-fidelity* methodologies.

Nonlinear potential flow methods share properties specific to both high-fidelity and low-fidelity methods. They are therefore compatible with higher fidelity methods and thus insert themselves well in the multi-fidelity workflow as a bridge between the high and low-fidelity realms. The challenge of multi-fidelity methods is to find an equilibrium between the required level of accuracy and computational cost.

1.2.3 Complex Aircraft Configurations

As mentioned previously, the design of aircraft components is a tightly-coupled endeavor. [3] illustrates this principle in the attempt of finding minimum induced drag for canard wing configurations. It is shown that the lift distribution leading to maximum efficiency deviates from the classical elliptical shape when the interaction with other aerodynamic bodies is non-negligible. In the particular context of canard configurations, the optimal load distribution on the main wing should take into account the contribution in lift of the canard in the inboard portion of the span so that the global lift distribution is optimal (Figure 1.4). In fact, optimizing the isolated wing would lead to suboptimal performance once the full aircraft is considered. This rationale can be extended to complex configurations, wherein the inclusion of additional interactions yields results that increasingly approximate the actual optimal design solutions. This is critical in a multi-fidelity design context.

1.3 Research Objectives

Based on the underlying problematic raised throughout the precedent sections, this research aims at developing a medium-fidelity numerical solver than can model general aircraft configurations as well as nonlinear behavior with increased fidelity. Having proved its validity and maturity in the past, singularity-based potential flow methods are selected to handle the three-dimensional modeling of the geometry of interest, while coupled sectional data is used to include nonlinear effects. A balance between accuracy, modelling complexity and computational cost is sought for the development of the solver.

In this regard, the following research objectives are proposed:

1. Introduce and investigate general aircraft configurations using a nonlinear singularity-based potential flow approach;
    (a) Assess the modeling of fuselage effects;
    (b) Assess the impact of auxiliary lifting surfaces on the resulting lift distributions;
2. Investigate the fidelity of the 2.5D RANS hypothesis for full aircraft configurations in separated and transonic flow conditions compared to 3D RANS and wind tunnel data;
3. Introduce and investigate the modeling of taper effects in the sectional data (2.75D RANS);
    (a) Propose a solver methodology for 2.75D RANS
    (b) Assess the impact of the 2.75D hypothesis on the convection of flow quantities

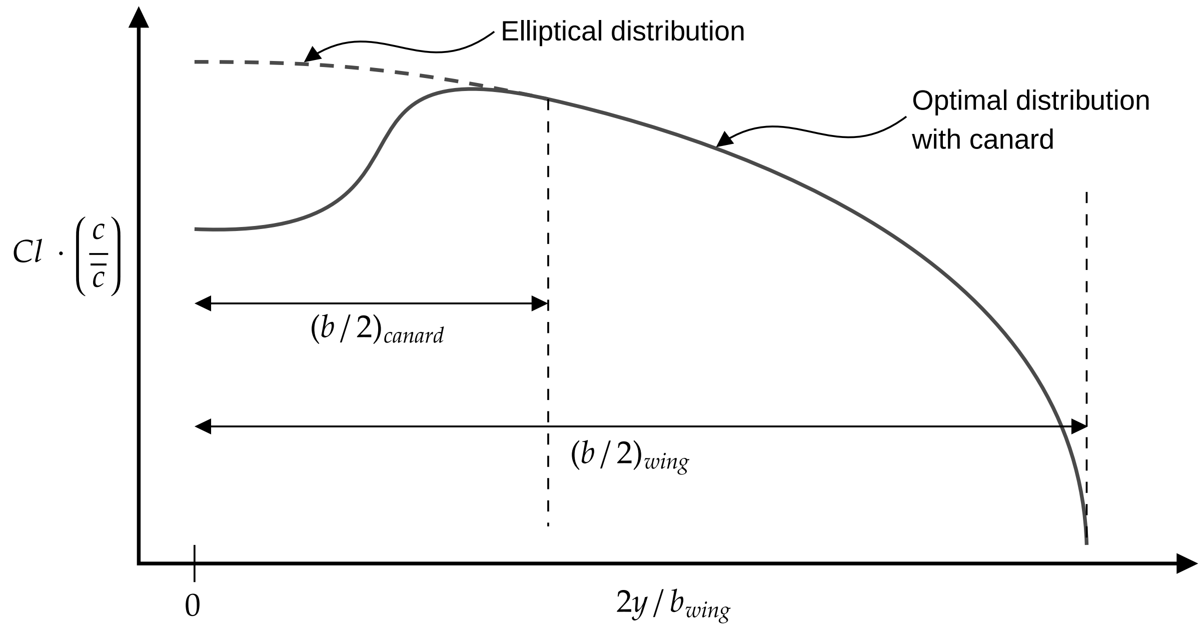

Figure 1.4 Optimal load distribution for a wing placed downstream of a canard wing of shorter span - Adapted from [3]

1.4 Plan of Thesis

To address the research objectives, the remainder of this work is organized into three primary sections. Firstly, a review of the literature is presented, focusing on the state-of-the-art in medium-fidelity methods. This includes a fundamental review of linear potential flow theory, where the development of singularity-based numerical methods is highlighted. Subsequently, an overview of cutting-edge coupling methods that incorporate viscous effects into initially inviscid flows is provided. Finally, the underlying physical assumptions governing the computation of sectional data used in nonlinear coupling algorithm are detailed.

In Chapter 3, the formulation of the potential solver is elaborated upon. The baseline linear potential flow solver is verified through a series of unit tests, specifically designed to assess the impact of horizontal and vertical lifting surfaces, as well as fuselage effects. Thereafter, the coupling algorithm introducing nonlinear effects is detailed. The algorithm is then verified through canonical 2D and 2.5D cases. Finally, a validation of the complete nonlinear potential flow solver is performed, and the outcome is compared with higher fidelity CFD results as well as with wind tunnel data.

Chapter 4 addresses the issue of wing taper in the generation of the sectional coupling data used in the nonlinear potential flow solver. A general methodology for tackling 2.75D is proposed leveraging the conical flow assumption within the spherical form the of Navier-Stokes equations. A spherical coordinates discretization scheme of the Euler Equations is detailed.

In conclusion, the present study is summarized, and its limitations are discussed, while avenues for future research are identified and highlighted.

CHAPTER 2 LITERATURE REVIEW

2.1 Potential Flow Theory

Singularity-based potential flow methods have proven successful, particularly in an era where computational resources were limited and unable to match the numerical and physical complexity of higher fidelity models such as the RANS family of solvers. Even today, these methods remain integral to fast iterative workflows. Although these approaches are feasible in two dimensions, they are especially prevalent in three-dimensional applications because of their significant computational efficiency relative to RANS/Euler solvers. In addition, they provide critical insight on various aerodynamic phenomena, such as the estimation of the induced drag force. The following section explores how singularity-based potential flow methods can estimate the aerodynamic behavior of finite wings and bodies of arbitrary shapes.

2.1.1 Lifting Line/Surface

The first major application of potential flow theory to finite wings through Prandtl's Lifting-Line Method (LLM). The idea behind the LLM can be visualized by considering the concept of effective angle of attack. For a finite wing of span b, where $-b/2 < y < b/2$, the effective angle of attack at a given spanwise location y_0 is defined as:

$$\alpha_e(y_0) = \alpha - \alpha_i(y_0) \tag{2.1}$$

where α_i is the induced angle of attack, which is associated with a spanwise variation of the local lift force. Consequently, the local lift for a wing section at position y_0 is given by $Cl(y_0) = f(\alpha_e(y_0))$, with $f(\alpha)$ representing the lift polar of the local 2D airfoil section. For thin uncambered airfoils, this relationship is commonly approximated as $f(\alpha) = 2\pi\alpha$. The induced angle of attack also plays a crucial role in the estimation of induced drag.

The LLM represents a finite lifting entity as a vortex segment of strength Γ, producing lift via the Kutta-Joukowski theorem. However, formulating a wing as a single vortex segment violates the Helmholtz vortex theorem, which establishes two fundamental conditions:

1. The circulation Γ must remain constant throughout the vortex segment.
2. A vortex segment must extend to the farfield, either by positioning at least one end at infinity or by looping the segment back onto itself.

To satisfy these conditions, the LLM must be *bent* and trailed along the freestream direction to infinity, forming a horseshoe vortex of constant strength Γ. This vortex consists of a *bound* segment and two free *wake/trailing* segments (Figure 2.1). A spanwise variation of the lift is achieved by stacking infinitesimally small horseshoe vortices along the span.

The vortex segment is a fundamental solution to the Laplace equation, allowing the induced angle of attack $\alpha_i(y_0)$ to be expressed analytically as:

$$\alpha_i(y_0) = \frac{1}{4\pi V_\infty} \int_{-b/2}^{b/2} \frac{d\Gamma/dy}{y_0 - y}\, dy \tag{2.2}$$

By rearranging (2.1) and (2.2), and applying the Kutta-Joukowski theorem, the LLM equation is derived:

$$\alpha(y_0) = \frac{\Gamma(y_0)}{\pi V_\infty c(y_0)} + \frac{1}{4\pi V_\infty} \int_{-b/2}^{b/2} \frac{d\Gamma/dy}{y_0 - y}\, dy \tag{2.3}$$

This equation can be discretized and solved using N horseshoe vortices. Generally, this discretization is followed by a Fourier series decomposition to obtain a spectral representation of the lift distribution $\Gamma(\theta)$, where $y = -\frac{b}{2}\cos\theta$. Once the N coefficients of the series (denoted A_n) are obtained, the Kutta-Joukowski theorem and (2.2) can be used to compute the lift and induced drag forces:

$$\begin{cases} C_L &= \pi A_1 AR \\ C_{Di} &= \frac{C_L^2}{\pi AR}\left[1 + \sum_{n=2}^{N} n \left(\frac{A_n}{A_1}\right)^2\right] \end{cases} \tag{2.4}$$

Although the LLM is simple and practical for high-aspect-ratio ($AR \geq 4$) straight wings, it is less effective for more complex modern wing designs. In particular, it struggles to accurately model general planforms, such as swept wings with non-negligible dihedral, and fails to provide accurate estimates for highly cambered wings (thus leading to a very poor estimation of the pitching moment). Although variations of the original method, such as the Finite Step Method [4, 5], have been developed to address these limitations, alternatives such as the Lifting Surface Theory offer a more comprehensive approach by allowing a multidimensional variation of circulation.

One of the most widely used algorithms based on this theory is the Vortex-Lattice Method (VLM) [6]. Unlike the combination of N horseshoe vortices, the VLM discretizes the wing planform into a grid of $N \times M$ horseshoe vortices, allowing for a general circulation distribution $\Gamma(u(x,y,z), v(x,y,z))$ (Figure 2.2). Rather than directly using the effective angle of attack, the VLM enforces the flow-tangency boundary condition at the $N \times M$ collocation

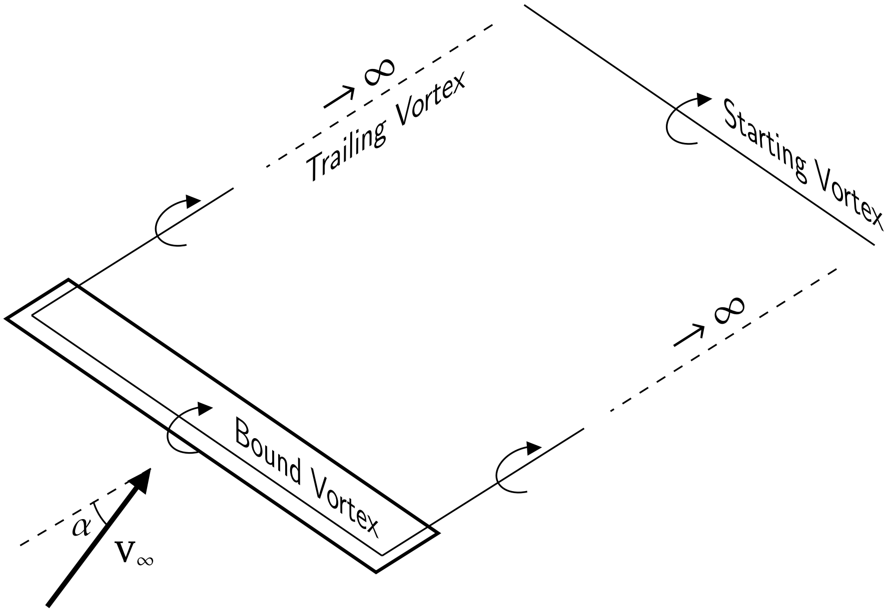

Figure 2.1 Modeling of a straight wing using a horseshoe vortex element

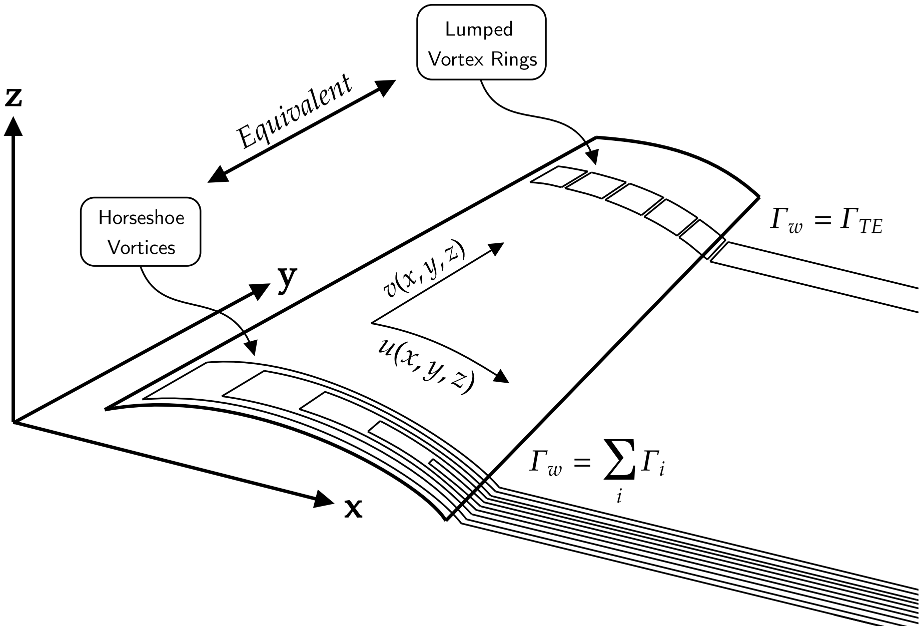

Figure 2.2 Modeling of an arbitrary-shaped wing using the VLM - The Kutta condition must be taken into account adequately depending on the type of element (*horseshoe/ring*)

points distributed on the surface of the wing.

$$\left(\sum_{j=1}^{N\times M} \mathbf{V}_{j\to i} + \mathbf{V}_\infty\right) \cdot \mathbf{n}_i = 0 \quad \forall\, i = 1, 2, \ldots, N \times M \tag{2.5}$$

where $\mathbf{V}_{j\to i}$ represents the velocity induced by the j-th horseshoe vortex at the i-th collocation point. (2.5) can be rearranged in a linear system of equations of the form $\mathbf{A\Gamma} = \mathbf{b}$, which is then solved for the unknown singularity strengths $\mathbf{\Gamma}$. The core of the method is therefore mainly based on the computation and inversion of matrix $\mathbf{A}$, which is commonly referred to as the Aerodynamic Influence Coefficient (AIC) matrix.

As with the LLM method, the trailing segments of each horseshoe vortex must extend to the farfield to satisfy the Helmholtz theorem, resulting in a semi-infinite vortex sheet composed of M streamwise sections. This vortex sheet maintains constant strength:

$$\Gamma_{w,j} = \sum_{i}^{N} \Gamma_i \quad \forall\, j = 1, 2, \ldots, M \tag{2.6}$$

Alternatively, the $N \times M$ planform-bound horseshoe vortex elements can be lumped into *vortex ring* elements, as proposed in [6] and illustrated in Figure 2.2. In this case, the trailing vortex sheet is also replaced by M vortex rings, with their circulation defined from the values at the trailing edge from which they have been shed:

$$\Gamma_{w,j} = \Gamma_{TE,j} \quad \forall\, j = 1, 2, \ldots, M \tag{2.7}$$

where $\Gamma_{TE,j}$ is the circulation at the trailing edge of the j-th streamwise section. The two aforementioned approaches are mostly equivalent and only differ slightly in implementation.

2.1.2 Panel Method

It is generally adequate to represent modern wing designs using LLMs or VLMs, since they generally feature high aspect ratios and low thickness. However, the modeling of blunt and low-aspect ratio bodies is often necessary for an accurate analysis of a complete aircraft. Those bodies range from the short delta-shaped wings of fighter jets to the conventional cylindrical fuselage and nacelles found on most commercial aircraft.

The Panel Method [7], although quite similar to the VLM, extends its capabilities by including thickness effects in its solution process. More generally, the body of interest is represented as a watertight surface subdivided into a set of N panels of arbitrary shape (generally triangular or quadrilateral) as shown in Figure 2.3. It also uses variations of the flow-tangency condition as its core to ensure the impermeability of the body.

In its most primitive form, each panel that makes up the body is made of a source singularity of constant-strength σ uniformly distributed on its surface. Depending on the sign of σ, a panel can act as source ($\sigma > 0$) or a sink ($\sigma < 0$). For example, a strong positive source will be found near an upstream stagnation point, and vice versa.

Although resulting in streamlines tangent to the body of interest, the absence of vorticity (Kutta condition) results in the method yielding zero lift. For this purpose, modern three-dimensional panel methods generally involve a combination of antisymmetric flow singularity types, such as the vortex ring and the distributed doublet panel. There is a significant number of combinations in that regard, each with their own advantages and drawbacks; the most common ones are detailed in [6] and are summarized in Table 2.1.

Table 2.1 Common singularity and boundary condition combinations for the panel method

Singularity	**Boundary Condition**	**Lifting?**	**Pros**	**Cons**
Source	Neumann ($\nabla\Phi^* \cdot \mathbf{n} = 0$)	No	-	-
Doublet	Neumann ($\nabla\Phi^* \cdot \mathbf{n} = 0$)	Yes	Simple implementation	Oscillations in velocity near-field
Vortex	Neumann ($\nabla\Phi^* \cdot \mathbf{n} = 0$)	Yes	Second order accurate	Ill-conditioned AIC matrix
Doublet	Dirichlet ($\Phi^*_i = 0$)	Yes	Numerically efficient	Convergence issues for large singularity values
Source + Doublet	Dirichlet ($\Phi^*_i = \Phi_\infty$)	Yes	Stable even for $N \gg 1$	Requires two AIC matrices

2.2 Nonlinear Coupling Algorithms for Potential Flow Methods

Although potential-flow-based methods are computationally and physically efficient in predicting the aerodynamic performance of an aircraft at idealized (linearized) flow conditions, their realm of application remains quite narrow, that is, for attached, low speed and mostly

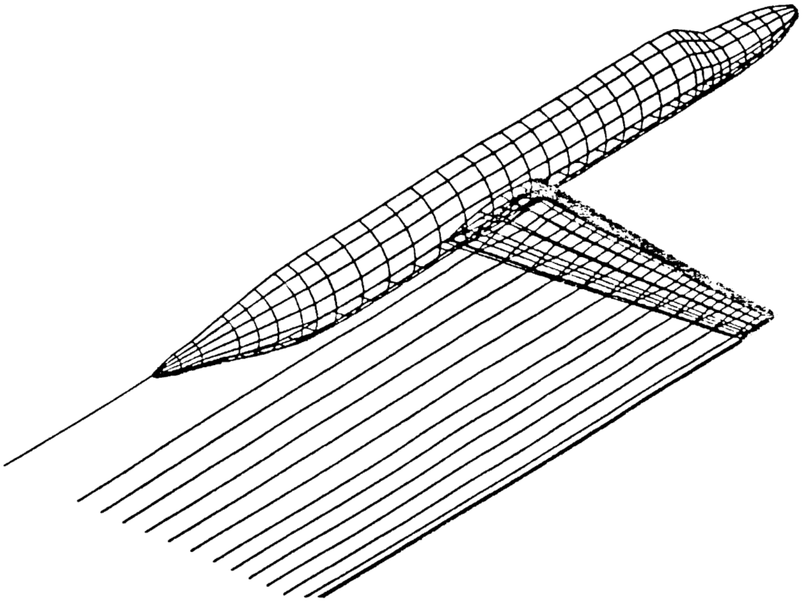

Figure 2.3 Panel method discretization of a wing-body configuration - Wake panels are shed from a sharp trailing edge and are modeled as thin vortex sheets - [8]

inviscid flows. The idea of many coupling algorithms is to introduce nonlinear effects via the integration of higher fidelity data within a potential-based (or generally inviscid) flow solver. This high-fidelity data, generally based on a set of simplifying hypotheses for computational efficiency, are obtained either in a Just-In Time (JIT) manner or precomputed and stored in a database. The coupling process is performed via a series of iterations following a common loosely-coupled algorithm. We define in Algorithm 1 $\mathcal{P}$ the model handling the coupling (the potential/inviscid flow solver in this case), $\mathcal{D}$ the coupled model accounting for nonlinear effects and $\mathcal{I}_{\mathcal{P}\rightarrow\mathcal{D}}$ and $\mathcal{I}_{\mathcal{D}\rightarrow\mathcal{P}}$ the interfaces between the two models.

In this procedure, $\mathcal{D}$ acts as the nonlinear counterpart of $\mathcal{P}$ for a quantity of interest, while the interfaces act as correctors for the inputs of each models/solvers. Consequently, for a given potential flow model $\mathcal{P}$, proper definitions of $\mathcal{D}$, $\mathcal{I}_{\mathcal{P}\rightarrow\mathcal{D}}$ and $\mathcal{I}_{\mathcal{D}\rightarrow\mathcal{P}}$ are required. The following section describes popular coupling algorithms for inviscid/potential flow solvers. They are also summarized in Table 2.2.

2.2.1 Boundary Layer Coupling

Boundary layer methods use the assumption that the shear layer near a body is infinitesimally thin, such that the Navier-Stokes equations can be simplified into a set of curvilinear PDE defined on the boundary of a body. The surrounding flow region can then be adequately mod-

Algorithm 1 General steps for nonlinear coupling algorithms with potential flow methods

```
Initialize $\mathcal{P}$ at its linear conditions
Define a convergence criterion $\mathcal{C}(\epsilon)$ where $\epsilon$ is the tolerance of the iterative process
Define an initial guess for $x_{\mathcal{P}}^0$
$y_{\mathcal{P}}^0 \leftarrow \mathcal{P}(x_{\mathcal{P}}^0)$
$x_{\mathcal{D}}^0 \leftarrow \mathcal{I}_{\mathcal{P}\rightarrow\mathcal{D}}(y_{\mathcal{P}}^0)$    ▷ An initial step is performed at linear flow conditions
for iteration $i$ in maxIterations do
    $y_{\mathcal{D}}^i \leftarrow \mathcal{D}(x_{\mathcal{D}}^i)$    ▷ The nonlinear coupled data is evaluated
    $x_{\mathcal{P}}^i \leftarrow \mathcal{I}_{\mathcal{D}\rightarrow\mathcal{P}}(y_{\mathcal{D}}^i)$    ▷ The coupling variable of $\mathcal{D}$ is mapped as an input for $\mathcal{P}$
    $y_{\mathcal{P}}^i \leftarrow \mathcal{P}(x_{\mathcal{P}}^i)$    ▷ The potential/inviscid solver is evaluated
    $\Delta y_{\mathcal{P}}^i = y_{\mathcal{P}}^i - y_{\mathcal{P}}^{i-1}$
    $\delta^i = \mathcal{C}(\Delta y_{\mathcal{P}}^i)$    ▷ The convergence criteria is evaluated
    if $\delta^i < \epsilon$ then
        break
    else
        $x_{\mathcal{D}}^i \leftarrow \mathcal{I}_{\mathcal{P}\rightarrow\mathcal{D}}(y_{\mathcal{P}}^i)$    ▷ The potential/inviscid solver is corrected for the next iteration
Compute quantities of interest
```

eled with an inviscid or panel method. The thickness of the boundary layer being unknown and dependent on pressure distribution along the walls, the coupling between the inviscid and boundary layer solvers is done iteratively. The direct form of the algorithm consists of iterating between each solver sequentially. At each iteration, the airfoil is thickened according to the boundary layer calculation, which in turn influences the pressure distribution. Convergence is reached when the difference in thickness between two successive iterations is small enough.

These methods generally yield good results for mostly attached flows. However, the parabolic form of the equations makes the algorithm unstable and generally inaccurate at the separation point when using the direct formulation (that is, when the local velocity changes direction). Strongly coupled algorithms such as the triple layer formulation of [9] and the fully coupled methodology of [10] are good alternatives because they offer increased stability for detached flows at the cost of slightly increased computational time per iteration.

2.2.2 Γ Coupling

The so-called Γ-coupling methods were the first invented for accounting for nonlinearities via sectional high-fidelity data. The original approach was first introduced by [11] and couples the spanwise lift distribution $\Gamma(y)$ (hence the name) to the local effective angle of attacks $\alpha_e(y)$. The high fidelity data is usually taken from two-dimensional RANS solutions of the sections of the wing. From a known lift distribution, the effective angles of attacks of each wing sections are found using a potential flow solver (for example, with (2.2)) and the corresponding local high-fidelity lift values are computed at their respective angles. The local circulation distribution is then updated using the Kutta-Joukowski theorem evaluated at the high-fidelity lift value. The iterative process is then repeated until the local lift outputs of the two solvers are close enough.

Although this method shows good agreement on simple cases when compared to reference data, significant convergence issues make the method impractical for more complex analyses [2, 12]. It was pointed out by [2] that a very low relaxation factor is necessary to reach a convergent solution, which requires several hundred iterations. Additionally, even with a prohibitively low relaxation value, the algorithm mostly fails to reach convergence in near and post stall regions. This phenomenon was studied by [13] and more recently with [14] and [15]. Once a local section reaches its Cl_{max} (that is when $dCl/d\alpha$ becomes zero), oscillating stall cells appear in the lift distribution and make the algorithm converge to a non-unique number of possible solutions. In this regard, [14] introduced an artificial dissipation factor into his algorithm in order to *smooth* the lift distribution and help converge to a unique solution. [15], on the other hand, applies a low-pass Gaussian filter in the goal of dissipating the high-frequency modes found in the lift distribution at high angles. This filtering, however, leads to two distinct lift distributions for a converged solution: the first obtained from the integrating the high-fidelity at the local effective angles of attack, and the other from the filtered lift distribution.

2.2.3 α Coupling

First introduced by [16], α-coupling methods replace the dependency on the local circulation value as a coupling variable by instead using directly the local effective angle of attack as its base. The effective angles of attacks are corrected by comparing the values of the lift coefficients obtained by the inviscid and reduced high-fidelity models. The updated angles of attacks are then applied in the potential flow solver as an artificial twist and the inviscid lift coefficient is re-evaluated. This principle is illustrated in Figure 2.4.

The idea of using the α-coupling algorithm with linear potential flow methods was popularized by [18], and for this reason this algorithm is often referred to as Van Dam's algorithm. A particularity of Van Dam's method is that the angle of attack correction $\Delta\alpha$ is computed directly using the differential relation bridging $Cl(y)$ and $\alpha(y)$.

$$\Delta Cl = Cl_{visc} - Cl_{inv} = \frac{dCl}{d\alpha}\Delta\alpha \tag{2.8}$$

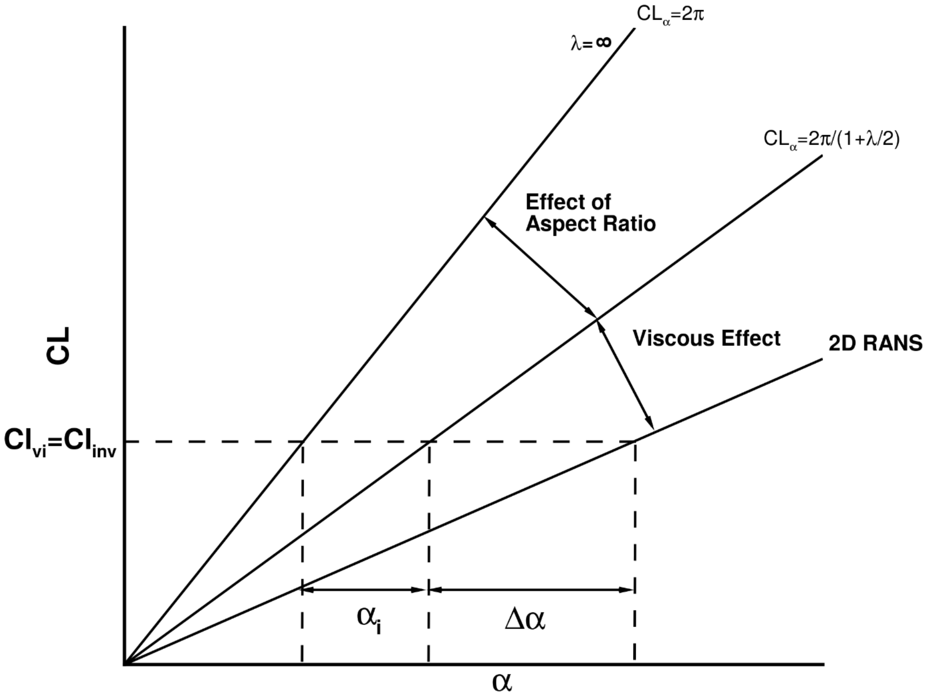

Figure 2.4 General principle of the α-coupling algorithm - The converged state of the algorithm is shown - [17]

However, the existence of two distinct lift polars makes the definition of $dCl/d\alpha$ ambiguous. In his initial proposition, Van Dam uses the local viscous lift slope. This however leads to stability problems near the stall region where the lift slope decreases to zero and changes in sign. Instead, [19] proposed using Thin Airfoil Theory (TAT) to predict the local lift polar derivative in the inviscid realm, such that $dCl/d\alpha = 2\pi =$ constant. This implies that the potential solver must not assume small angles so that the inviscid lift slope remains constant throughout the whole polar. Therefore, the angle of attack correction procedure must be modified to enforce a coherence between the predictions of the potential solver and TAT.

The α-coupling method family continues to be improved and extended to this day in the context of preliminary design and analysis. In more recent years, [17] extended this algorithm to Multi-Disciplinary Optimization (MDO) by introducing flow-dependent design criterion. For example, wing stall optimization was performed by utilizing the position of appearance of stall cells along the span as a design objective. The stall cell phenomenon was also further studied by [20] using a α-coupled lifting surface in the goal of investigating the discoveries of [15]. Good qualitative agreement in the number and wavelength of the cells with CFD and experimental results was observed. It was also mentioned that for the coupling algorithm to be stable, a local minima must be present in the lift polar after stall, with the lift converging asymptotically to a constant value being the limit case. This suggests that the high-fidelity database must cover a wide range of values in the post-stall regime for the algorithm to be stable in Cl_{max} studies. Finally, [21] extended the realm of application even further by applying this coupling algorithm to unsteady aerodynamics and aeroelasticity. His solver uses a frequency-domain formulation allowing an unsteady problem to be solved for given user-defined modes. Furthermore, this formulation still uses steady local high-fidelity data for the coupling, while the inertial terms due to the unsteady physics are treated in the potential flow solver.

Table 2.2 Summary of the components and interfaces used in the principal coupling algorithms for inviscid/potential flow methods.

Method	**Inviscid Solver ($\mathcal{P}$)**	**Interface $\mathcal{P} \rightarrow \mathcal{D}$**	**High-Fidelity Data ($\mathcal{D}$)**	**Interface $\mathcal{D} \rightarrow \mathcal{P}$**
Boundary Layer Coupling	Euler / Full Potential / Panel Method	Pressure/Velocity distribution	Parabolic Boundary Layer Solver	Geometry is thickened / Transpiration velocity
Γ-Coupling	LLM / VLM	$\alpha_e(y_0) = \alpha - \frac{1}{4\pi V_\infty} \int_{-b/2}^{b/2} \frac{d\Gamma/dy}{y_0 - y}\, dy$	2D RANS / Experimental / ...	$\Gamma = \frac{1}{2}\rho_\infty V_\infty^2 Cl_{visc}$
α-Coupling	LLM / VLM	$\alpha_e = \frac{Cl_{inv}}{dCl/d\alpha} - \Delta\alpha + \alpha_0$	2D RANS / Experimental / ...	$\Delta\alpha = \frac{Cl_{inv} - Cl_{visc}}{dCl/d\alpha}$

2.3 Computation of High Fidelity Coupling Data

The accuracy of nonlinear potential flow methods is highly dependent on the quality of the high-fidelity data used in the coupling. For example, the introduction of a non-zero $Cl_{viscous,0}$ in lift-based coupling algorithms will be directly reflected in the converged solution, even though the linear potential flow solver has no notion whatsoever of the camber of the individual wing sections. Hence, the hypothesis used in the computation of the local high-fidelity data must be as close of the actual resultant three-dimensional flow as possible. This section highlights the physical and numerical considerations on the generation of adequate sectional high-fidelity data.

2.3.1 Infinite Swept Flow Theory

The generation of sectional high-fidelity data for the Γ-coupling and α-coupling algorithms generally consists in two-dimensional RANS solutions taken at the local Mach and Reynolds numbers. This is however a significant simplification that results in poor agreement for highly-swept wings. This is due to the fact that different flow topologies come into play when a non-negligible sweep angle is introduced. Firstly, a stagnation line is observed rather than a stagnation point (Figure 2.5a). Secondly, oblique shocks are observed in transonic conditions rather than normal shocks (Figure 2.5b).

[23] introduced a simple way to correct 2D line-of-flight solutions using incompressible and inviscid transformations (2.9) based on the flow conditions perpendicular to the sweep line. The corrected lift coefficient is obtained via (2.10).

$$\begin{cases} M_{x'} &= M_\infty \cos\phi \\ M_{y'} &= M_\infty \sin\phi \end{cases} \tag{2.9}$$

$$\frac{Cl'}{Cl} = \frac{M_\infty^2 \cos\phi}{1 - M_\infty^2 \cos^2\phi} \tag{2.10}$$

Using this transformation recovers the correct local lift slope Cl_α, and must be used within the α-coupling algorithm instead of 2π in order to obtain an accurate solution for swept wings. Furthermore, this approximates the magnitude of the crossflow velocity as constant (which is true for inviscid flows).

Another possible approach to tackle swept wings is the integration of sweep effects directly into a RANS flow solver by introducing the hypothesis that flow quantities are constant along the sweep line ($\partial/\partial y' \simeq 0$). This approach is commonly referred to as 2.5D RANS, as it allows

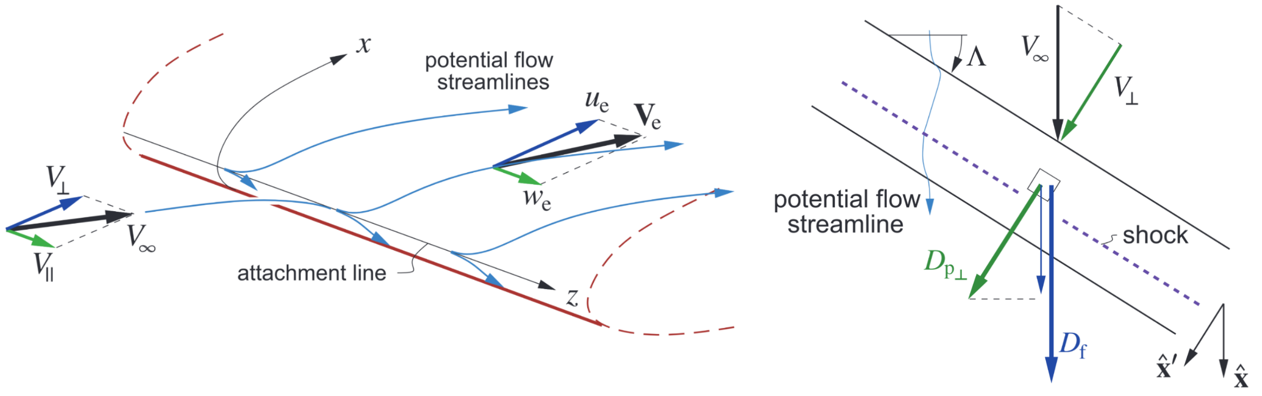

(a) Stagnation line

(b) Oblique shock

Figure 2.5 Main features of infinite swept flows in viscous and transonic conditions - [22]

reducing the three-dimensional Navier-Stokes system of equations to a two-dimensional one combined with an extra equation for the momentum in the crossflow. Figure 2.6 illustrates two common ways of handling 2.5D problems.

In the sheared-cell approach (Figure 2.6a), the full 3D RANS equations are used on a tridmensional mesh. The 2.5D mesh is made of a standard 2D mesh of the airfoil which is then extruded by exactly one cell according to the sweep line. A periodic boundary condition is then applied on both longitudinal surfaces. The β approach (Figure 2.6b) uses a coordinate transformation (2.11) to keep the topology of the mesh two-dimensional [24]. The topology, however, remains three-dimensional due to the sideslip angle β of the freestream velocity in the transformed simulation domain. Hence, the momentum equation in the transverse direction can be decoupled from the system and solved in a loosely-coupled fashion.

$$\begin{Bmatrix} x' \\ y' \\ z' \end{Bmatrix} = \begin{bmatrix} \cos\phi & -\sin\phi & 0 \\ \sin\phi & \cos\phi & 0 \\ 0 & 0 & 1 \end{bmatrix} \begin{Bmatrix} x \\ y \\ z \end{Bmatrix} \tag{2.11}$$

Applying both these approaches to various flow conditions showed excellent agreement with both 3D CFD and experimental results, where the expected flow topologies are recovered. Although the results yielded by both methods are similar, it was pointed out by [24] that the β approach is both more computationally efficient and accurate than its 3D counterpart. In fact, the loosely-coupled strategy uses 4×4 instead of 5×5 Jacobian matrices when using an implicit time-stepping scheme and remove the need of adding two layers of ghost cells on both periodic planes for the computation of the boundary conditions. Furthermore, only two

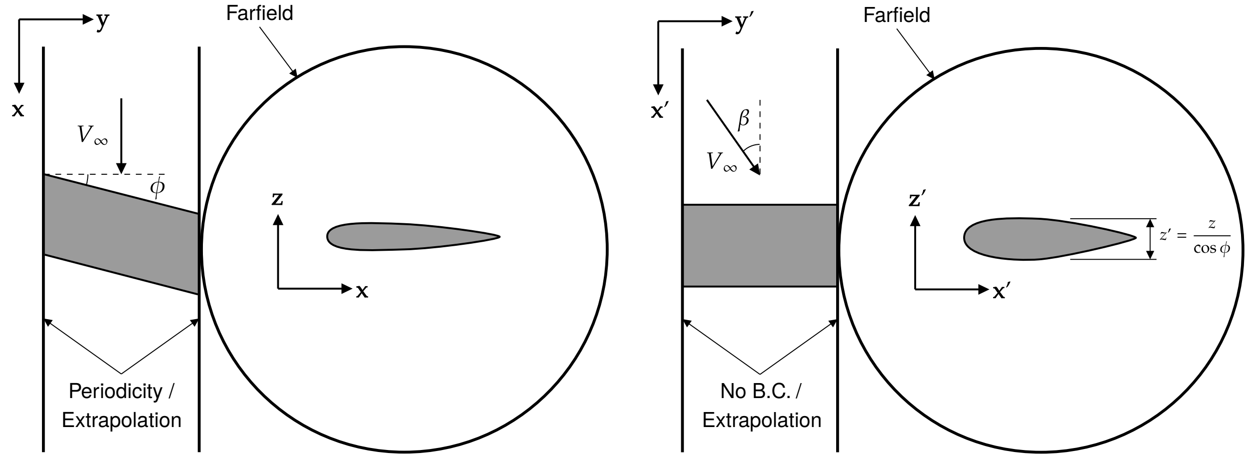

(a) Sheared-cell approach

(b) β approach

Figure 2.6 Two common ways modeling infinite swept flow problems using a two-dimensional geometry - Note that method (b) can be achieved using a 2D mesh topology by specifying no boundary conditions on the lateral sides.

instead of three eigenvalues are used in local time-stepping and artificial dissipation schemes. Hence, the sheared-cell approach is known to yield slightly more dissipative solutions.

2.3.2 Considerations for Tapered Wings

The core idea of infinite swept flow theory is to assume that variations of flow quantities perpendicular to the local isobars are negligible. While this is mostly valid for high aspect-ratio wings, this hypothesis becomes invalid as the taper ratio of the wing $\lambda = c_{tip}/c_{root}$ is far from unity. In this case, the isobars follow a conical distribution rather than a series of parallel lines. This is also true for wings presenting a *Yehudi* break, where the sweep angle at the trailing edge of the inboard portion of the wing is significantly reduced.

When taper is significant, the choice of an adequate sweep angle is crucial as it directly dictates the apparition of the main flow features, and thus significantly impacts the resulting solution. The chosen sweep angle is referred to as the effective sweep angle ϕ^*. [17] and [19] both made interesting studies on the influence of the sweep angle on the results obtained from α-coupling method coupled with 2.5D RANS data. On the Bombardier Research Wing (BRW), it was found that the results correlates with reference data best when ϕ^* is evaluated at the quarter chord point. For inboard wing sections, it was found that the half chord point is often preferred, presumably because of the reduced transversal flow in the separation topology at the trailing edge. On the DLRF4 in transonic flow conditions, ϕ^* is chosen

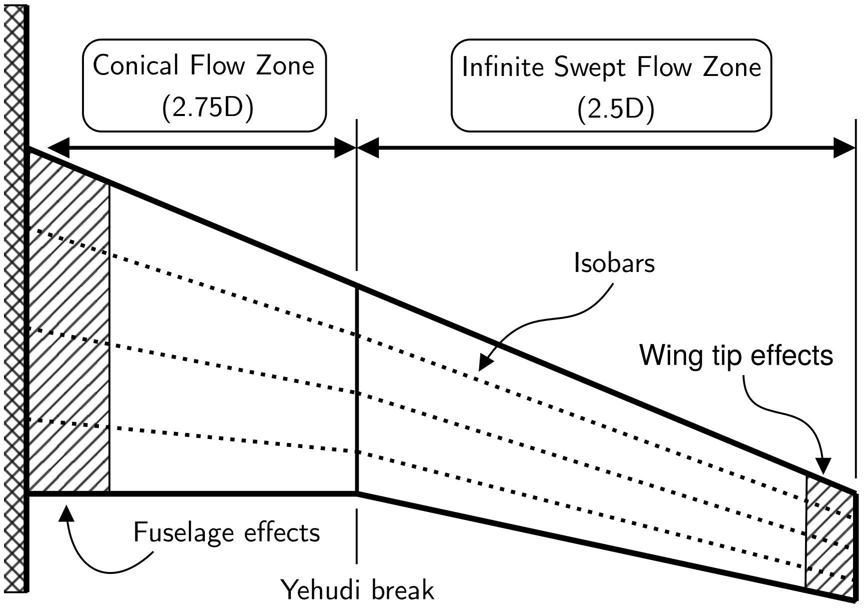

Figure 2.7 Conventional commercial aircraft wing presenting a Yehudi break. The inboard region with non-negligible taper is subject to the conical flow assumption.

at the location of the oblique shock (located between the quarter and half chord points), since the local isobars are mostly aligned with it. Thus, generating 2.5D data in transonic conditions requires knowledge about the location of the shock *a priori*.

It is in this regard that methods based on the conical flow assumption have been developed. These methods are based on the fact that the isobars are defined parallel and constant to the local sweep lines. Two families of approaches are presented in the following section.

Relations Between 2D and 3D Pressure Distributions

[25] first introduced the idea of relating three-dimensional pressure distributions to equivalent two-dimensional pressure distributions. The concept of his method is heavily inspired on the work of [23], where the pressure distribution obtained from a 2D RANS simulation is corrected so that the chordwise local Mach number distribution $M_{2D,n}$ equals the local Mach number of a conical wing normal to the isobars $M_{3D,n}$. This is done using the following isentropic relation:

$$\frac{1+\frac{1}{2}(\gamma-1)(M_{3D}\cos\phi(x'))^2}{1+\frac{1}{2}(\gamma-1)M_{2D}^2} = \left[\frac{1+\frac{1}{2}\gamma M_{3D}^2 Cp_{2.75D}}{1+\frac{1}{2}\gamma M_{2D}^2 Cp_{2D}}\right]^{(\gamma-1)/\gamma} \tag{2.12}$$

where Cp_{2D} and $Cp_{2.75D}$ are respectively the input 2D and output 2.75D pressure coefficients, $\phi(x')$ is the local sweep angle, and $M_{2D} = M_{3D}\cos\phi^*$ is a reference Mach number for the local two-dimensional section taken at a nominal sweep angle ϕ^* (evaluated at the quarter chord point or at the location of the shock). In other words, whereas the normal Mach number is constant for an infinite swept wing, this method essentially translates a tapered wing as a series of infinite swept wings where the local normal Mach number varies along the chord. This methodology was used by [26] for supercritical wing design. Their analysis showed that the isentropic hypothesis on which the transformation is based still holds in the presence of a shock wave if it is aligned with the local sweep lines.

This approach was enhanced by [27] to model more accurately regions of subsonic flows, where according to them the initial assumptions of Lock are not satisfied. Their idea is to eliminate the need for a reference Mach number M_{2D} by instead using the local value $M'_{2D}(x') = M_{3D}\cos\phi(x')$. The 2D RANS flow simulation is computed at M_{2D}; $Cp_{2D}(x')$ is transformed to match $M'_{2D}(x')$ using the Karman-Tsien compressibility correction. The results of [27] seemed to be in quite good agreement with their in-house 3D CFD solver for low angles of attack. However, this solution is still limited by its isentropic hypothesis, and it is unclear whether the geometrical shape of the airfoil section and its angle of attack can be directly determined without prior knowledge of the 3D pressure distribution.

2.75D Flow Solvers

Analogous to the benefits observed with 2.5D, the incorporation of sweep and taper effects directly into a 2.75D flow solver is advantageous, as it enables the accurate representation of diverse topological features specific to conical flow. Such methods, for instance, would allow the possibility of a stagnation point (not line) at the leading edge while also allowing for crossflow separation at the trailing edge.

The initial emergence of 2.75D approaches manifested in the form of boundary layer methods. [28], [29] and more recently [30] proposed similar coordinate transformations to the standard compressible boundary layer equations (Figure 2.8). The polar coordinate system (r,θ) is used such that r is defined from an apex point r_0 and is oriented along the isobars towards the root of the wing. After formulating the equations in full polar non-axisymmetric form, $\partial p/\partial r = 0$ is enforced according to the conical flow hypothesis. The simulation domain consists of the curvilinear boundary defined by the intersection of a sphere of radius r with the conical wing surface. The simulation process is then performed by marching downstream from the leading edge stagnation point.

Attempts to extend conical flow assumptions to full RANS solvers have also been made, nonetheless with mixed results. The main difficulty arising from applying conical flow assumption to those methods is the fact that hyperbolic PDEs require a simulation domain

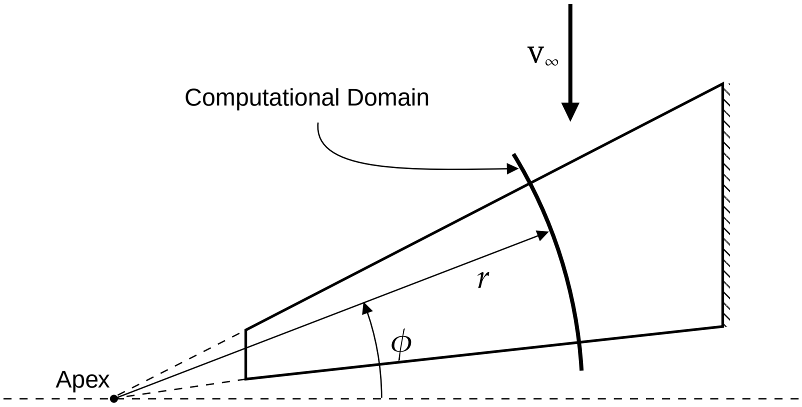

Figure 2.8 Theoretical representation of the conical flow assumption - The isobars are following rays radiating from the apex

extending up to the farfield. It is however unclear how this hypothesis must be handled when $\phi \to \infty$. In their structured RANS solver, [31] used what they refer to as a *relaxed conical flow boundary condition*, where the apex of the cone moves to infinity along $\phi = (\phi_{LE} + \phi_{TE})/2$ when the distance to the nearest wall is large. Hence, the farfield points behave like an infinite swept flow, while the points near the airfoil behave according to the full 2.75D hypothesis. [31] also showed that for slender cones, the flow asymptotically converges to a solution satisfying the conical flow hypothesis.

[32] used a similar methodology is his study of the DLRF4 aircraft in transonic flow conditions, where poor agreement with the inboard shock location was observed using regular 2.5D. His solver consisted in a generalization of the sheared-cell approach, where the computational plane is extruded and shrunk following the local isobars towards the apex of the conical wing. Using this methodology, the location of the inboard shock was improved, but an overestimation of the total drag was observed in addition to the fact that the temporal scheme relied significantly on the usage of Selective Frequency Damping (SFD) schemes to achieve proper convergence. In addition, it was noticed that changing the length of the extrusion of the computational domain lead to different results. Yet, the solution was found to converge to constant value as this length approached zero.

CHAPTER 3 MODELING OF FULL AIRCRAFT CONFIGURATIONS USING NONLINEAR POTENTIAL FLOW

Modern commercial aircraft are composed of several distinct components, each with their own purpose and characteristics. As their aerodynamic behavior is tightly coupled, it is desirable to include as much of them as possible in the context of preliminary design/analysis. Singularity-based potential flow methods are especially suitable for these endeavors, since they only require surface meshes rather than full field discretizations. Wings can be further simplified by projecting the full geometries into their planforms. Other components, such as nacelles, have non-negligible thickness and must be shaped according to their actual representations in three-dimensional space. The following sections present a hybrid potential flow solver with nonlinear capabilities and with the purpose of modeling various aircraft components.

3.1 Singularity-Based Potential Flow Solver

The idea behind a *hybrid* potential flow solver is to couple different modeling strategies in a single solver. In this work, thin and thick/blunt surfaces are modeled respectively using a VLM and Panel method. These methods were implemented in the CHAMPS [33] multidisciplinary aerodynamic framework using the Chapel programming language [34].

3.1.1 Thin Surface Modeling

Thin lifting surfaces such as wings and tail planes are modeled using a standard VLM leveraging lumped vortex ring elements (Figure 2.2) and following closely the implementation of [6]. In contrast to lifting line methods, the VLM relies on the flow-tangency condition (2.5) to compute the multivariate lift distribution $\Gamma(u, v)$. This condition is applied numerically by evaluating the total velocity induced at collocation points. By using as many collocation points as there are vortex rings, the linear system formed by (2.5) can be solved for $\mathbf{\Gamma}$.

As the vortex segments forming the rings are themselves singularities ($V_{ind} \to \infty$), the location of the collocation points must be chosen cleverly. By positioning the collocation point at the center of each vortex rings, this interference is minimized. Furthermore, by shifting back each vortex rings by a quarter-chord length, the local lift slope is guaranteed to be 2π and is then coherent with two-dimensional TAT. This statement is however based on the assumption of small angles of attack. For analysis at high angles of attack (e.g. for

Cl_{max} studies), the collocation point must be corrected using the following correction [19]:

$$r = \frac{c}{2}\frac{\alpha_e}{\sin\alpha_e} \tag{3.1}$$

where r is the distance between the center point of the leading vortex segment to the collocation point and c the full length of vortex ring and α_e is the local effective angle of attack taking wing twist and camber into account.

Once the location of the vortices and collocations points are fixed, the induced velocity at each collocation point is computed, summed and stored into an AIC matrix. The AIC matrix is computed using the Biot-Savart solution for a vortex segment [6]:

$$\nabla\Phi_{vortex} = \frac{\Gamma}{4\pi}\frac{\mathbf{r}_1 \times \mathbf{r}_2}{|\mathbf{r}_1 \times \mathbf{r}_2|^2}\mathbf{r}_0 \cdot \left(\frac{\mathbf{r}_1}{|\mathbf{r}_1|} - \frac{\mathbf{r}_2}{|\mathbf{r}_2|}\right) \tag{3.2}$$

where $\mathbf{r}_1$ and $\mathbf{r}_2$ are the vectors between each of the endpoints and $\mathbf{r}_0$ is the director vector of the vortex segment. With four segments per vortex ring, each entry of the linear system of equation is then given by

$$\begin{aligned} a_{ij} &= (\nabla\Phi_1^{j\to i} + \nabla\Phi_2^{j\to i} + \nabla\Phi_3^{j\to i} + \nabla\Phi_4^{j\to i}) \cdot \mathbf{n}_i \\ b_i &= -\mathbf{V}_\infty \cdot \mathbf{n}_i \end{aligned} \tag{3.3}$$

The Kutta Condition is included in the linear system of equations via (2.7). This is applied numerically by adding the influence of wake panels to their trailing edge counterpart in the AIC. Wake panels are assumed to be parallel to the freestream and are propagated $1000c$ downstream.

Compressibility Correction

The VLM can be enhanced to approximate high-speed flow using various compressibility corrections. CHAMPS VLM solver uses the Prandtl-Glauert Transformation (PG) compressibility correction for this purpose. This correction works by applying the following change of variable [22].

$$\begin{Bmatrix} \overline{x} \\ \overline{y} \\ \overline{z} \end{Bmatrix} = \begin{Bmatrix} x \\ \beta y \\ \beta z \end{Bmatrix} \tag{3.4}$$

where $\beta = \sqrt{1 - M_\infty^2}$ is the PG factor and ($\overline{x}$,$\overline{y}$,$\overline{z}$) are the freestream-aligned coordinates (x,y,z) in the new PG space. Following the transformation in this space, the standard

VLM linear resolution process is performed. This process yields the circulation distribution $\overline{\Gamma}(\overline{x}, \overline{y}, \overline{z})$ in PG space, which then needs to be converted back to the solution space using the inverse transformation.

$$\overline{\Phi} = \beta^2 \Phi \Leftrightarrow \Gamma = \frac{\overline{\Gamma}}{\beta^2} \tag{3.5}$$

Although this formulation does not model nor allow shock waves near the sonic point, it allows the VLM to recover the correct modified linear lift polar slope, as shown in Figure 3.1. The PG correction is well suited for compressible flows at $|M_\infty \ll 1|$; however, as indicated in [35], there is a tendency for the predicted velocities near the sonic point to be underestimated.

Computation of Loads

The computation of the different forces acting on the thin geometry of interest is divided in two parts:

1. Computation of the lift force and aerodynamic moment
2. Computation of the induced drag

The computation of the local forces and moments is done via the Kutta-Joukwski theorem linking directly the circulation distribution to the local loads.

$$\begin{aligned} \mathbf{F}(u,v) &= \rho_\infty \Gamma(u,v) \mathbf{V}_\infty \times l\mathbf{d} \\ \mathbf{M}(u,v) &= \mathbf{r} \times (\rho_\infty \Gamma(u,v) \mathbf{V}_\infty \times l\mathbf{d}) \end{aligned} \tag{3.6}$$

where $\mathbf{F}$ is the total force vector and where l and $\mathbf{d}$ are respectively the length and the director vector of the leading vortex. For a planar wing, (3.6) reduces to the standard form of the Kutta-Joukowski theorem $dL = \rho_\infty V_\infty \Gamma$.

The computation of the induced drag D_i is more involved as it requires the integration of velocity perturbations infinitely far downstream. This is done by evaluating quantities at a plane (the Trefftz plane) sufficiently far from the body (about 1000 chords). In the case of thin wake sheets, the surface integral on the plane is reduced to a curvilinear integral (Figure 3.2).

$$D_i = -\frac{\rho_\infty}{2} \int_{\mathcal{I}} w(s) \Gamma(s) ds \tag{3.7}$$

where $\mathcal{I}$ is the curve formed by the intersection of the wake sheet with the Trefftz plane and w is the local downwash. First, the downwash normal to the wake is evaluated at the Trefftz

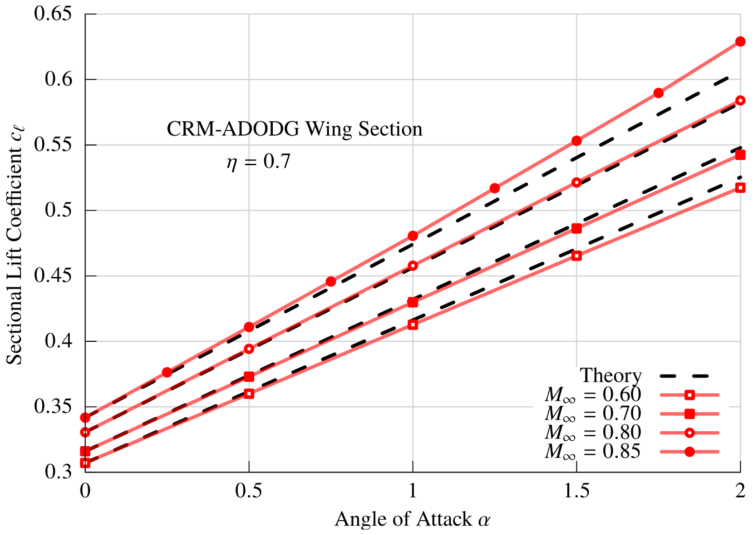

Figure 3.1 Impact of the PG compressibility correction on the lift polar slope. The PG correction (Theory) tend to underestimate compressibility effects at high Mach numbers - [36]

plane using the two-dimensional point vortex singularity kernel (3.9) for each of the $M+1$ wake trailing vortices. The integral is then carried on numerically.

$$D_i = -\frac{\rho_\infty}{2}\sum_{j=1}^{M}\sum_{k=1}^{M+1}(\nabla\Phi_{2D}^{k\to j}\cdot\mathbf{n}_j)\Gamma_j dl_j \tag{3.8}$$

with

$$\nabla\Phi_{2D}^{k\to j} = -\frac{\Delta\Gamma_k}{2\pi r_{kj}}\mathbf{e}_\theta = -\frac{\Gamma_{k+1}-\Gamma_k}{2\pi\sqrt{(\Delta y'_{kj})^2+(\Delta z'_{kj})^2}}(\mathbf{e}_r\times\mathbf{e}_{x'}) \tag{3.9}$$

where (x', y', z') forms a local coordinate system with $\mathbf{e}_{x'}$ aligned with the director vector of the kth trailing vortex.

The global lift force can also be obtained from Trefftz plane integration.

$$L = \rho_\infty V_\infty\sum_{j=1}^{M}(\mathbf{n}_j\cdot\mathbf{N})\Gamma_j dl_j \tag{3.10}$$

where $\mathbf{N}$ is the global lift axis of the aircraft.

An important note about (3.8) and (3.10) is that **only** values defined at the Trefftz plane are used for the computation (assuming that the Trefftz plane is positioned sufficiently far downstream of the lifting surface, that is about $1000c$). Consequently, this formulation is both more stable and efficient than computing the downwash directly at the aerodynamic body, since the calculation is independent of the chordwise resolution of the mesh in the nearfield.

3.1.2 Vertical Surface Modeling

Thin vertical surfaces such as vertical tail planes and wing pylons and fences play important roles in modern aircraft configurations. While they generally have minor effects on viscous lift and drag, their influence on lift-induced quantities such as the induced drag can be significant.

The case of wing pylons and fences is particularly interesting because their presence directly interferes with the resulting spanwise lift distribution. In the limit case where a wing pylon/fence is both perpendicular to the wing and parallel to the flow, the influence on the lift distribution is reduced to a point discontinuity (Figure 3.3), where a strong upwash is induced inboard, while a strong downwash is induced outboard of the vertical component. Similarly, this discontinuity creates variations in the effective angles of attack distribution, meaning that the resulting induced drag will be necessarily affected. The implementation of vertical surfaces in a VLM solver is quite straightforward. The vertical surface is discretized using vortex rings along the vertical axis. In addition, for the vertical to carry a side force, a vertical wake sheet is meshed in order to satisfy the Kutta condition. Finally, a connection boundary condition is used at the junction of the two trailing vortices at the planform.

$$\Gamma_{i,j_0}^{wing} = \Gamma_{i,j_0}^{pylon} \tag{3.11}$$

where the pylon is located at the j_0th wing station.

[5] was one of the first to study the effects of vertical surfaces within singularity-based potential flow theory using a Finite Step method. Several hypothetical cases were studied, where low-speed experimental data was used in some of them as basic validation data. These results are used therein as a verification exercise for the current implementation. From the results of Figure 3.4a, the implementation of the wing-pylon interaction in the VLM solver is in agreement with the observations of Blackwell. As expected, the upwash and downwash at the immediate inboard and outboard regions of the pylon are observed while the loads at the root and tip remains more or less unchanged. Figure 3.4b shows also good agreement with low-speed experimental data at the wing fence, where the magnitude of the lift discontinuity is of the same order.

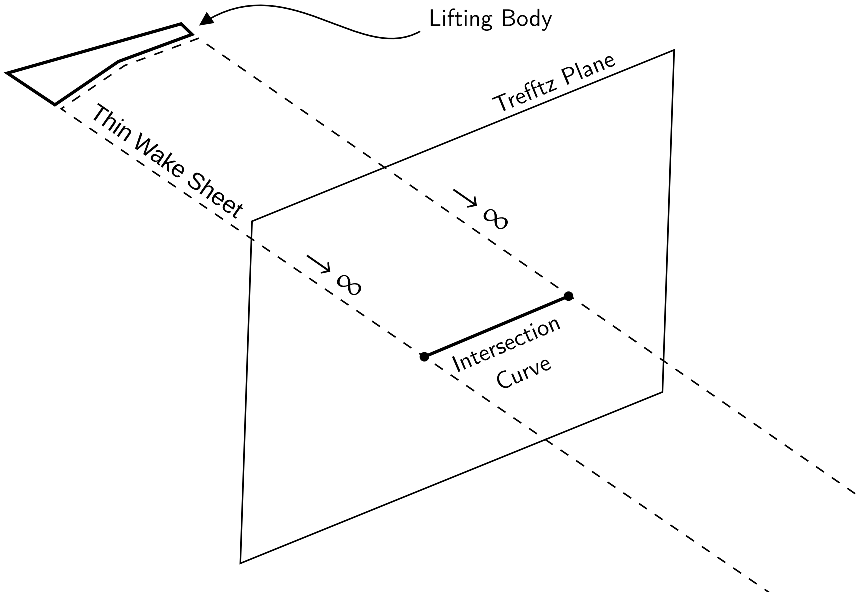

Figure 3.2 Representation of the Trefftz plane analysis for thin vortex sheet elements

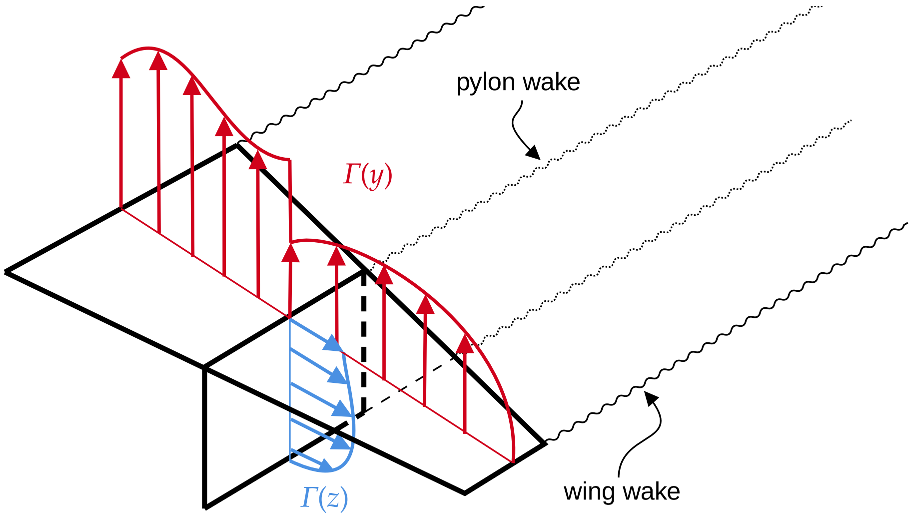

Figure 3.3 Discontinuity in the spanwise circulation/lift distribution caused by the presence of a thin wing pylon on a finite wing - [37]

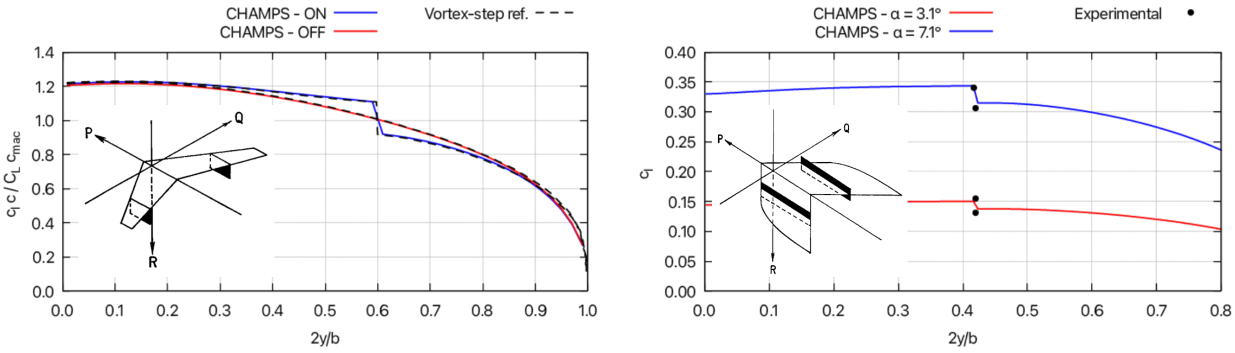

(a) Wing pylon ($M_\infty = 0$)

(b) Wing fence ($M_\infty \simeq 0.1$)

Figure 3.4 Comparison of the effects of thin vertical surfaces on the lift distribution - Graph taken from [37] - Geometry and reference data taken from [5]

3.1.3 Multi-Plane Drag

An advantage of the VLM is that the elliptical nature of potential flow makes the modelling of multi-plane/wing configurations very easy. Each of the lifting surfaces are represented as separate planforms with each their respective Kutta conditions and wakes. Numerically, this is done by subdividing the dense linear system into blocks.

$$\begin{bmatrix} \mathbf{A}_{1\to1} & \mathbf{A}_{2\to1} & \dots & \mathbf{A}_{n\to1} \\ \mathbf{A}_{1\to2} & \mathbf{A}_{2\to2} & \dots & \mathbf{A}_{n\to2} \\ \vdots & \vdots & \ddots & \vdots \\ \mathbf{A}_{n\to2} & \mathbf{A}_{n\to2} & \dots & \mathbf{A}_{n\to n} \end{bmatrix} \begin{Bmatrix} \mathbf{\Gamma}_1 \\ \mathbf{\Gamma}_2 \\ \vdots \\ \mathbf{\Gamma}_n \end{Bmatrix} = \begin{Bmatrix} \mathbf{b}_1 \\ \mathbf{b}_2 \\ \vdots \\ \mathbf{b}_n \end{Bmatrix} \tag{3.12}$$

where $\mathbf{A}_{i\to j}$ is the AIC of the ith lifting surface acting on the jth lifting surface and $\mathbf{b}_i$ is the standard boundary condition vector for the ith surface as shown in (3.3). Hence, the computation of the global AIC matrix is done by first computing the individual sub-matrices (generally using multithreading) and by assembling them in a dense block matrix.

Concerning the induced drag calculation, since there are as many distinct wakes as there are lifting surfaces, the Trefftz integral (3.7) is split among $N_{\mathcal{I}}$ intersection curves instead of only one.

$$D_i = -\frac{\rho_\infty}{2} \sum_{n=1}^{N_{\mathcal{I}}} \int_{\mathcal{I}_n} w_n(s) \Gamma_n(s) ds \tag{3.13}$$

From this formulation we note that this approach is coherent with Munk's stagger theorem [38] stating that the induced drag of a system is equivalent to the superposition of the loading of all surfaces. In fact, this analogy can be illustrated conveniently using Prandtl's biplane formula [38] for two elliptically loaded wings.

$$D_i = \frac{L_1^2}{q\pi b_2^2} + 2\kappa \frac{L_1 L_2}{q\pi b_1 b_2} + \frac{L_2^2}{q\pi b_2^2} \tag{3.14}$$

The first and last terms of this equation represent *self-induced drag* quantities, while the middle term acts as an *interference* term with $\kappa = f(b_1/b_2, 2h/b_1)$, a nonlinear parameter depending on the span and vertical gap ratios. Being based on the assumption of elliptically loaded surfaces, this equation consists in a valid approximation only for $b_1/b_2 \sim 1$ and/or $2h/b_1 \gg 0$. Table 3.14 illustrates a numerical comparison between the induced drag obtained via Trefftz plane integration (3.13) and the biplane formula (3.14) for two elliptical wings of the same span ($b_1/b_2 = 1$).

In addition to the induced drag calculation, special care must be taken when modeling aircraft presenting a conventional wing-tail or canard configuration. In fact, these configurations are at risk of presenting mesh intersections causing very large induced velocities when a collocation point is close to a strong wake vortex, as it is the case in Figure 3.5. This situation is mitigated by introducing the Vatista [39] relaxation to the vortex segment kernel (3.2) so that the resulting induced velocity is smoothed when the distance r to the singularity approaches zero, as shown in Figure 3.6. The Vatista smoothed kernel is defined as

$$\nabla\Phi_{vatista} = \frac{\Gamma}{4\pi} \frac{\mathbf{r}_1 \times \mathbf{r}_2}{\left(|\mathbf{r}_1 \times \mathbf{r}_2|^{2n} + |\sigma \mathbf{r}_0|^{2n}\right)^{1/n}} \mathbf{r}_0 \cdot \left(\frac{\mathbf{r}_1}{|\mathbf{r}_1|} - \frac{\mathbf{r}_2}{|\mathbf{r}_2|}\right) \tag{3.15}$$

where σ and n are user-defined parameters for controlling the radius and smoothing of the relaxed kernel in the vicinity of the singularity.

Table 3.1 Comparison of the induced drag for a biplane configuration with varying vertical gap ratio $2h/b_1$ (in drag counts) - [37]

$2h/b_1$	**CHAMPS VLM** (3.13)	**Biplane formula** (3.14)	**Error**
0.2	7.157	7.156	-0.001
0.5	6.811	6.877	-0.066
0.8	6.526	6.586	-0.060
1.0	6.389	6.386	0.003

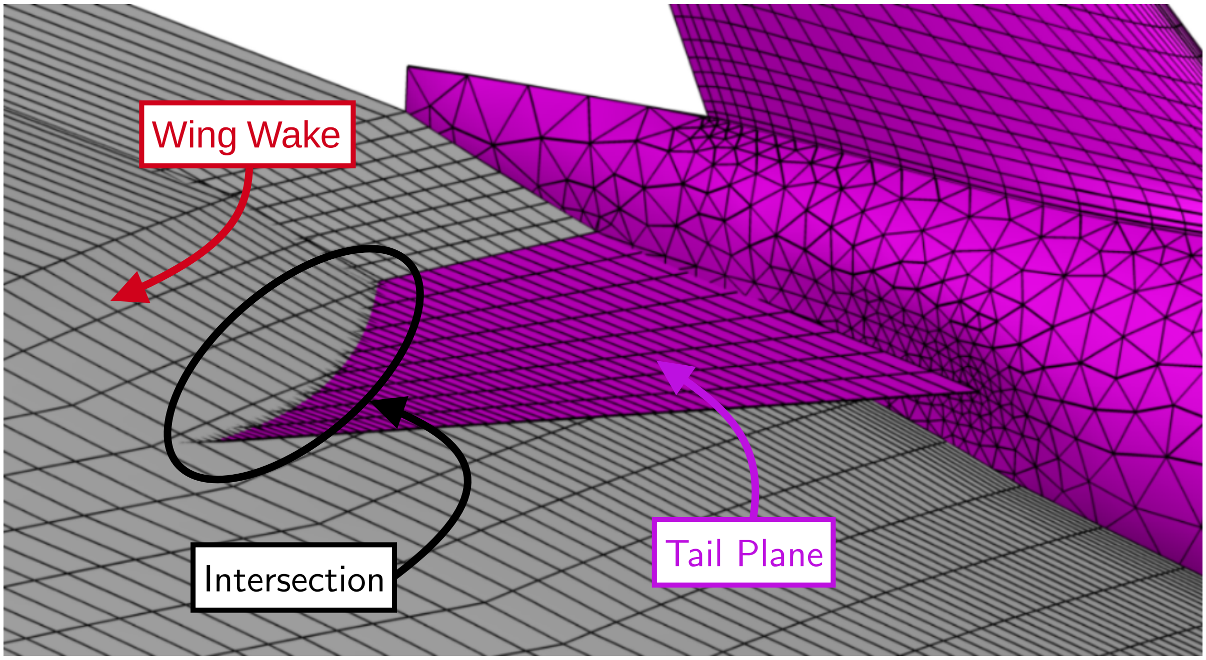

Figure 3.5 Mesh intersection caused by the wake of a wing with the horizontal tail plane

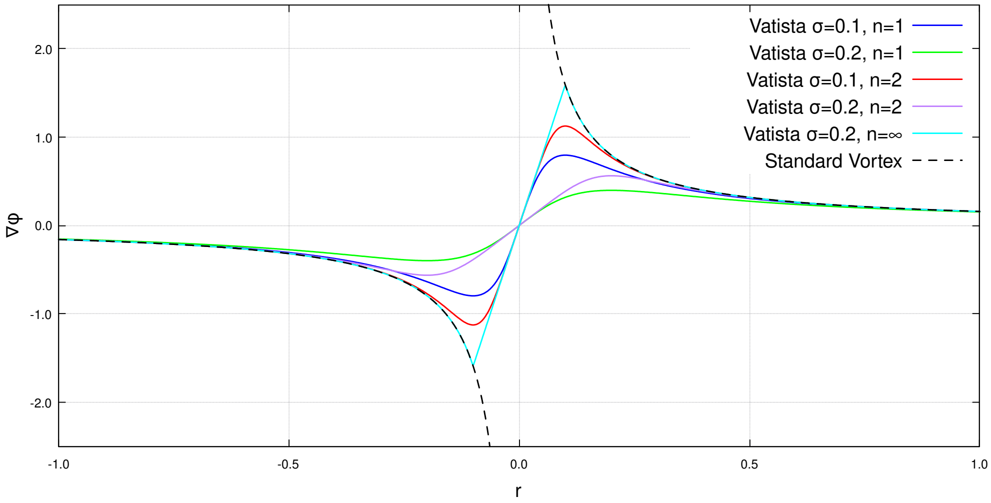

Figure 3.6 Comparison of the Vatista vortex singularity for different values of σ and n

3.1.4 Fuselage and Nacelle Modeling

For bodies for which thickness effects cannot be neglected, such as fuselages and nacelles, a three-dimensional panel method solver is used. The implementation of the panel method in the CHAMPS potential flow solver uses either source or a combination of source and doublet singularity elements. These panels are stored in an unstructured memory layout allowing for geometrically complex shapes to be meshed easily using arbitrary triangles and quadrilaterals.

As mentioned in section 2.1.2, the choice of singularity elements also comes with the choice of an adequate boundary condition defined at N collocation points on the surface of the aerodynamic body. This boundary condition can take a *direct* or *indirect* form. The direct form consists in a Neumann boundary condition where the flux of the total potential perpendicular to the surface is set to zero.

$$\nabla\Phi^* \cdot \mathbf{n} = 0 \tag{3.16}$$

The indirect form is a Dirichlet boundary condition directly specifying the total internal potential referential to a constant value. It can be loosely interpreted as the implicit/integral formulation of the flow-tangency condition.

$$\Phi_i^* = constant \tag{3.17}$$

Although these two forms ultimately result in streamlines tangent to the surface, the implementation effort and the resulting stability of the methods vary. In particular, the induced quantity kernel ($\nabla\Phi$ or Φ) changes depending on the boundary condition enforced at a particular collocation point. These kernels are more or less expensive to evaluate numerically depending on the choice of singularity elements and boundary conditions.

Panel Method with Source Singularities

If the body of interest is assumed non-lifting, source singularity elements can be used. Following [6] and Table 2.1, the Neumann boundary condition is selected. Using this approach, the resolution process follows closely what was presented in section 3.1.1. Yet, the distributed source induced velocity kernel is used instead.

$$\Phi_{source}(x', y', z') = -\frac{\sigma}{4\pi}\iint_S \frac{1}{\sqrt{(x'-x_0')^2 + (y'-y_0')^2 + (z')^2}} dS \tag{3.18}$$

where (x',y',z') forms the local coordinate system of the panel (Figure 3.7). Analytical solutions to the surface integral as well as for the induced velocity $\nabla\Phi$ are detailed in [6] and [8]. Following the resolution of the linear system, the pressure coefficient distribution is computed using the incompressible Bernoulli law.

$$Cp = 1 - \left(\frac{|\nabla\Phi^*|}{|\nabla\Phi_\infty|}\right)^2 \tag{3.19}$$

In addition to the zero-lift assumption, the computation of the loads is a clear disadvantage of using this approach. In fact, the evaluation of $\nabla\Phi^*$ is an $\mathcal{O}(n^2)$ operation and is therefore expensive for high-resolution meshes.

Panel Method with Source-Doublet Singularities

If a combination of source and doublet singularity elements is chosen, the problem can be conveniently formulated as a constrained Dirichlet boundary condition problem. Indeed, as using two singularity elements per panel makes the problem overconstrained ($2N$ unknowns for N collocation points), the value of one of the two singularities must be prescribed in advance.

To formulate a constraint, the singularity strengths can be related to their respective potential jump values normal to the boundary of the body [6].

$$-\mu = \Phi^* - \Phi_i^* \tag{3.20a}$$

$$-\sigma = \frac{\partial\Phi^*}{\partial z'} - \frac{\partial\Phi_i^*}{\partial z'} \tag{3.20b}$$

By selecting the total internal potential Φ_i^* to be equal to the constant freestream value Φ_∞ in (3.17), a constraint for σ is obtained using (3.20b).

$$\frac{\partial\Phi^*}{\partial z'} = \mathbf{V}_\infty \cdot \mathbf{n} = \frac{\partial\Phi_i^*}{\partial z'} - \sigma = \frac{\partial\Phi_\infty}{\partial z'} - \sigma = -\sigma$$

$$\sigma = -\mathbf{V}_\infty \cdot \mathbf{n} \tag{3.21}$$

With σ being known, the linear system created by expanding (3.17) is made of two AICs (**A**

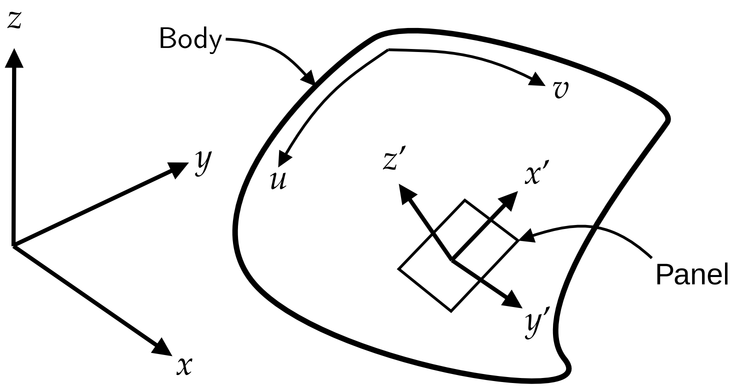

Figure 3.7 Local coordinate system for the evaluation of the induced velocity and potential kernels. z' is perpendicular to the body defined by $(u(x,y,z), v(x,y,z))$

and **B**) and takes the following form.

$$\begin{bmatrix} a_{1\to 1} & a_{2\to 1} & \dots & a_{n\to 1} \\ a_{1\to 2} & a_{2\to 2} & \dots & a_{n\to 2} \\ \vdots & \vdots & \ddots & \vdots \\ a_{1\to n} & a_{2\to n} & \dots & a_{n\to n} \end{bmatrix} \begin{Bmatrix} \mu_1 \\ \mu_2 \\ \vdots \\ \mu_n \end{Bmatrix} = - \begin{bmatrix} b_{1\to 1} & b_{2\to 1} & \dots & b_{n\to 1} \\ b_{1\to 2} & b_{2\to 2} & \dots & b_{n\to 2} \\ \vdots & \vdots & \ddots & \vdots \\ b_{1\to n} & b_{2\to n} & \dots & b_{n\to n} \end{bmatrix} \begin{Bmatrix} \sigma_1 \\ \sigma_2 \\ \vdots \\ \sigma_n \end{Bmatrix} \tag{3.22}$$

with $a_{j\to i}$ and $b_{j\to i}$ are respectively the doublet (3.23) and source (3.18) induced potential kernels.

$$\Phi_{doublet}(x', y', z') = -\frac{\mu}{4\pi} \iint_S \frac{z'}{[(x' - x'_0)^2 + (y' - y'_0)^2 + (z')^2]^{3/2}} dS \tag{3.23}$$

Forces are calculated using an approach similar to the previous method, that is, using (3.19). However, the evaluation of $|\nabla\Phi^*|$ on the boundary is improved by reintroducing potential jump relations (3.20):

$$\nabla\Phi^* = \nabla\Phi_\infty + \nabla\Phi_{doublet}|_{z'=0} + \nabla\Phi_{source}|_{z'=0} = \mathbf{V}_\infty - \left(\begin{Bmatrix} \partial\mu/\partial u \\ \partial\mu/\partial v \\ 0 \end{Bmatrix} + \begin{Bmatrix} 0 \\ 0 \\ \sigma \end{Bmatrix} \right) \tag{3.24}$$

where the gradient of the doublet potential $\nabla\Phi_{doublet}|_{z'=0}$ on the unstructured surface mesh is computed using a Weighted Least-Square (WLS) approach. The advantage of using such a methodology for the calculation of loads is that the operation is $\mathcal{O}(n)$ instead of $\mathcal{O}(n^2)$. This approach also mitigates the instabilities caused by the induced velocity of strong singularities on neighboring collocation points.

The PG correction of Section 3.1.1 can also be applied to panel methods in order to approximate global compressibility effects. Figure 3.8 shows a comparison of the pressure along an ellipsoid for different Mach numbers. It can be seen that the agreement between the combined source-doublet and Euler approaches is good even near the sonic point. This shows that the PG correction is a good approximation for compressible flows on thick bodies, where the critical Mach number is generally closer to unity than for thin ones. Lastly, the source-only panel method tends to present erroneous results (even divergent in Figure 3.8d) as the freestream Mach number increases, showing that the source-doublet combination may be more suitable. Another reason for preferring this version of the panel method is the fact that having a combination of two elements per panel lowers the intensity of the resulting singularities, effectively resulting in a numerically more robust method [8].

3.1.5 Hybrid Formulation

Being of the same nature, the VLM and the panel method can be linked by their respective boundary conditions in order to obtain a hybrid potential flow solver. Figure 3.9 illustrates the rationale of the methodology.

Considering the wing-body configuration of Figure 3.9 proposing a VLM and a source-doublet panel method, the interaction is carried out by calculating the appropriate induced quantity at a given location point. In other words, the required influence kernel (gradient or integral) depends on the body on which the collocation point lies on, while the kernel type depends on the singularity type of the influencing element. This methodology leads to the following block-based linear system of equations.

$$\left[\begin{array}{c|c} \mathbf{A}_{VLM\rightarrow VLM} & \mathbf{A}_{Panel\rightarrow VLM} \\ \hline \mathbf{A}_{VLM\rightarrow Panel} & \mathbf{A}_{Panel\rightarrow Panel} \end{array}\right] \left\{\begin{array}{c} \boldsymbol{\Gamma} \\ \hline \mathcal{M} \end{array}\right\} = -\left\{\begin{array}{c} \{\mathbf{V}_\infty \cdot \mathbf{n}_i\} \\ \hline \mathbf{B}\boldsymbol{\Sigma} \end{array}\right\} \tag{3.25}$$

It is interesting to note that the induced potential and velocity kernels for the doublet and vortex ring elements are the same [6]. This fact simplifies the implementation of the influence kernels, as it reduces the number instances from six to four.

Considerations for Fixed-Wake Wing-Body Configurations

In the particular case of wing-body configurations, special care must be taken in the simplified representation of the fixed-wake mesh. In first approximation, fuselages such as the one depicted in Figure 3.9 are assumed non lifting because of the lack of any sharp trailing edge and thus of resultant vorticity. However, the presence of a fuselage influences the propagation

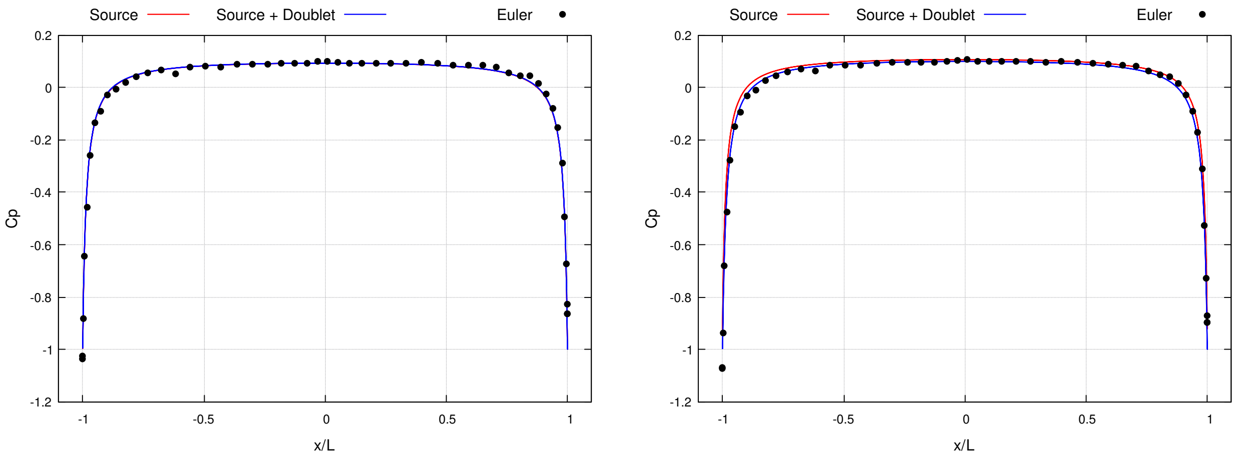

(a) $M_\infty = 0.1$

(b) $M_\infty = 0.5$

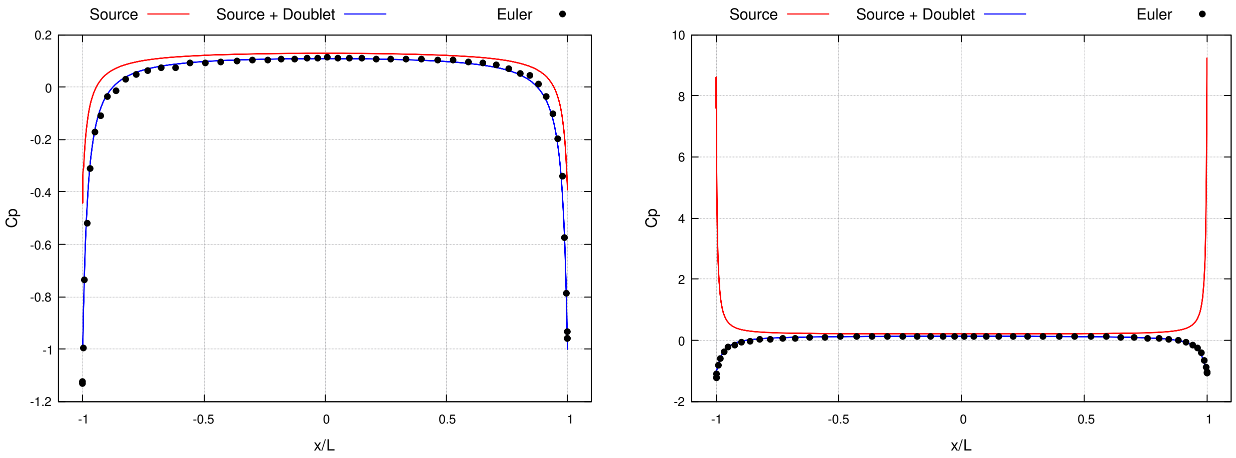

(c) $M_\infty = 0.7$

(d) $M_\infty = 0.9$

Figure 3.8 Pressure distribution along an ellipsoid for different Mach numbers and inviscid flow methods - $\alpha = 0\,\mathrm{deg}$

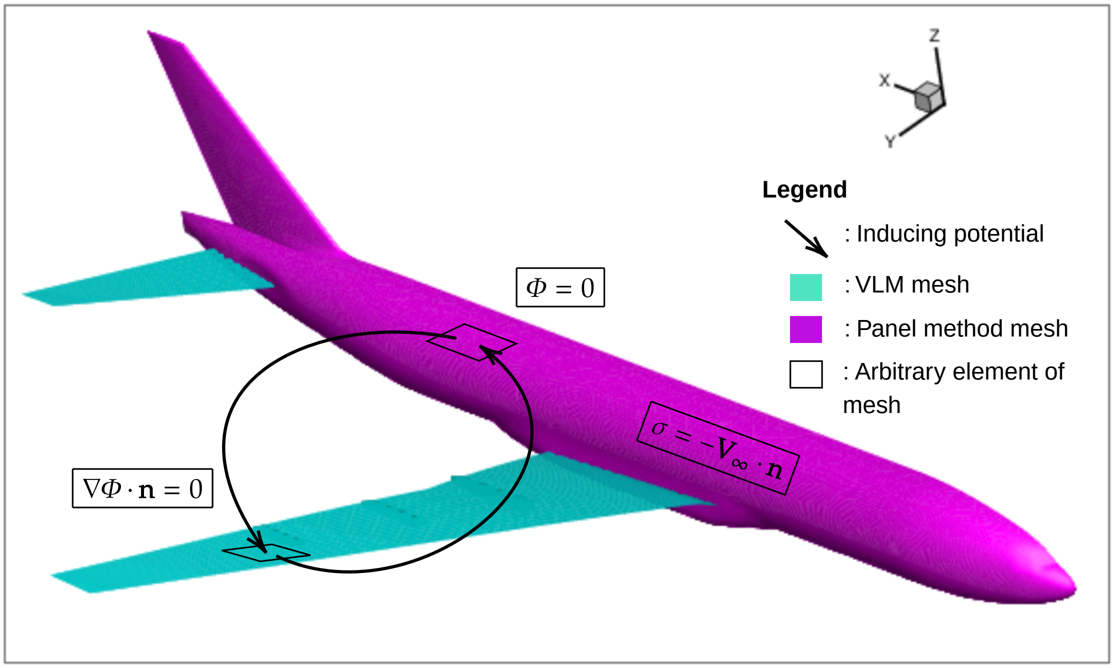

Figure 3.9 Interaction of the VLM and panel methods within the hybrid potential flow solver - [37]

of the local streamlines in the nearfield. Consequently, the orientation of the wake panels are no longer parallel to the freestream, but rather parallel to the local streamlines as shown in Figure 3.10. As suggested by [22], the local velocity distribution along the wake path can be computed iteratively within the potential flow model or in an unsteady fashion. In the current implementation, the Nikolski contraction [22,40] is used for its simplicity. Taking into account local axisymmetric sections of the fuselage, the deviated streamline at $\tilde{y}$ associated with the wing station at y can be calculated according to $\tilde{d}$ and d, the local and trailing edge-aligned fuselage diameters.

$$\tilde{y} = \sqrt{y^2 + \left(\frac{\tilde{d}}{2}\right)^2 - \left(\frac{d}{2}\right)^2} \tag{3.26}$$

This has the effect of extending the wake of the wing to the symmetry plane. However, the effective span length at the farfield $\tilde{b}$ is shorter than the actual full span b of the aircraft. Hence, $\tilde{b}/2$ instead of $b/2$ must be used along with the shifted circulation distribution $\Gamma(\tilde{y})$ when computing the induced drag and lift force at the Trefftz Plane using (3.8) and (3.10).

By following the local streamlines, the wake trailing vortices are essentially *stitched* to the side of the fuselage until the symmetry plane is met at $y = 0$. This can cause strong induced

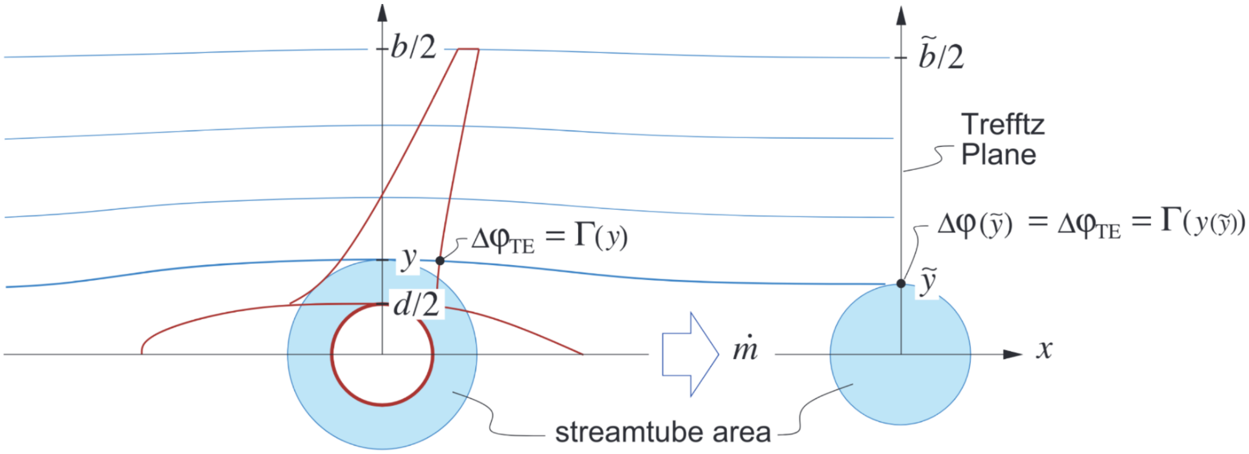

Figure 3.10 Local streamlines for potential flow around a fuselage. The Nikolski contraction assumes constant mass flow through axisymmetric stream tubes. - [22]

velocities on the fuselage, especially in high-lift conditions where the circulation in the wake is significant. In the case of the source-only panel method, this effect can be mitigated by using the Vatista kernel relaxation (3.15) for wake trailing vortices. In the case of the combined source-doublet panel method, the potential jump relations at the boundary (3.20) are not valid across discontinuities in the potential field. Hence, the gradient across any wake or thin vortex-lattice surfaces is neglected. Figure 3.11 illustrates the resulting pressure solution at the wake-fuselage intersection for both methodologies, where numerical artifacts are discernible in the solution from the source-only panel method.

In order to model wake interaction accurately, it is preferable to orient the wake mesh in the direction of the freestream flow. This however becomes challenging for wing-body configurations, since the topology of the wake changes dramatically with the angle of attack and the geometry of the fuselage. In fact, in this particular case, a distinct mesh must be generated for each angle of attack. This step can be automated at runtime using a mesh generation subroutine (Figure 3.12) leveraging an altered home-made version of the original A* algorithm [41] with the cost and heuristic functions at node $n+1$ defined as follows.

$$\mathrm{cost}(n+1) = \mathrm{cost}(n) + w_1 \cdot \mathrm{dist}(n, n+1) + w_2 \cdot \mathrm{deviation}(n+1) \tag{3.27a}$$

$$\mathrm{heuristic}(n+1) = w_1 \cdot \mathrm{dist}(n+1, \mathrm{goal}) + w_2 \cdot \mathrm{deviation}(n+1) \tag{3.27b}$$

where `dist()` is the Euclidean distance, `deviation()` is the deviation from the freestream plane and $w_1 \sim 0.2$ and $w_2 \sim 0.8$ are the weights of the cost function.

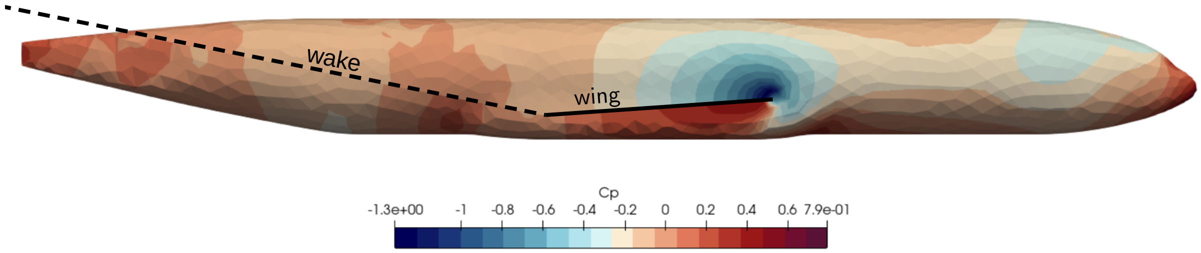

(a) Source-doublet panel method

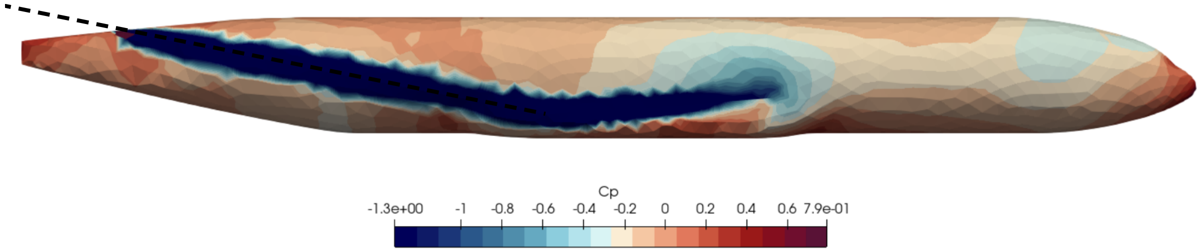

(b) Source-only panel method with Vatista vortex relaxation ($\sigma = 0.1$, $n = 2$)

Figure 3.11 Influence of thin vortex surfaces such as wings and wakes on the fuselage pressure distribution

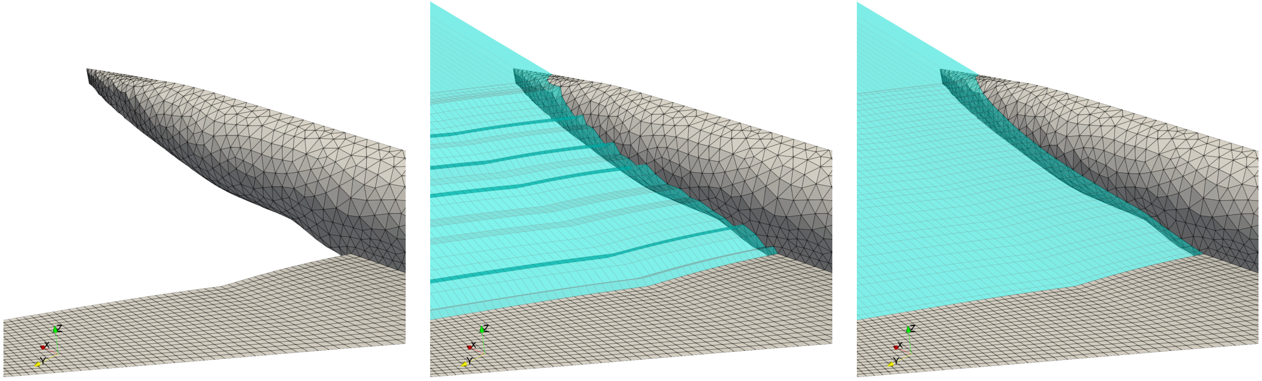

(a) Initial geometry

(b) Calculate path following local flow using A*

(c) Surface mesh is adapted and projected onto the freestream plane

Figure 3.12 Steps for automatic adaptative wake mesh generation for wing-body configurations

3.2 Nonlinear Coupling and Viscous Effects

Nonlinear phenomena for finite wings, including viscous boundary layers and stall, are incorporated into the potential flow solver through an iterative coupling algorithm. Empirical formulations are employed concurrently to represent the viscous drag of non-lifting bodies.

3.2.1 Coupling Algorithm

Van Dam's α-coupling algorithm of Section 2.2.3 is selected as the iterative method for incorporating nonlinear effects for its ability to accurately model stall phenomena with minimal convergence issues. Due to its iterative nature, the α-coupling algorithm with a VLM solver is often denoted as the Nonlinear Vortex-Lattice Method (NL-VLM). A single iteration of the method is implemented as follows:

1. After evaluating the potential flow solver, the distribution of effective angles of attack $\alpha_e(\eta)$ is calculated, where η is a curvilinear coordinate following the dihedral of the wing. The angle of attack correction $\Delta\alpha(\eta)$ is initialized at zero.

   $$\alpha_e = \frac{Cl_{inv}}{dCl/d\alpha} - \Delta\alpha + \alpha_0 \tag{3.28}$$

   The choice of $dCl/d\alpha$ is of capital importance as it significantly influences both the converged solution and the convergence properties of the algorithm itself. This value should be as close as possible to the actual local inviscid lift slope. [19] initially proposed using 2π in coherence with TAT. As this value is inadequate for swept wings [17], $2\pi\cos\phi$ may be used according to infinite swept flow theory. However, these two variations do not take into account the increase in the lift slope due to compressibility effects. In this regard, one can use the derivation proposed by [22] leveraging the normal Mach number and PG constant $\beta_n = \sqrt{1 - M_n^2}$.

   $$\frac{dCl}{d\alpha} = \frac{1}{\beta_n^2}\left(\frac{d\overline{Cl}}{d\overline{\alpha}}\right) = \frac{2\pi\cos\phi}{\sqrt{\beta^2\cos^2\phi + \sin^2\phi}} \tag{3.29}$$

   This formulation implies two requirements: 1) that the PG transformation is also applied to the potential flow model according to Section 3.1.1 and 2) that the local VLM lift slope is corrected for all angles of attack so that the value of 2π is recovered after transformation to PG space (e.g. using (3.1)). This application of the PG correction within the NL-VLM algorithm has been initially proposed by [42] and a better agreement with reference data has been observed in comparison with the usage of the standard 2π slope.

2. The local viscous lift coefficient Cl_{visc} of each streamwise wing sections is interpolated in a high-fidelity data according to the local α_e.
3. An angle of attack correction is formulated according to the difference between the viscous and inviscid lift coefficients.

$$\Delta\alpha^{n+1} = \Delta\alpha^{n} + \frac{Cl_{visc} - Cl_{inv}}{k} \tag{3.30}$$

   where k is generally defined as 2π. This value does not impact the resulting solution as long as none of the underlying wing sections are interpolated at post-stall α_e. After stall, the nonuniqueness of the solution means that slightly different results might be obtained for different values of k.

4. The new angle of attack correction is added to the potential flow solver. A common way to achieve this is to rotate the normals of all panels belonging to a wing section by $\Delta\alpha$ around the $\mathbf{e}_\eta$ axis.

A common approach used to validate this methodology is through the infinite wing case, where $CL = Cl(y) = \mathit{constant}$ for any prescribed sectional lift polar in accordance with the outlined assumptions of (3.29). Results for sectional lift polars, considering variations in linearity, Mach number, and sweep angles, are presented in Figure 3.13. These results demonstrate that the NL-VLM successfully captures the expected changes in the lift slope, thereby confirming that the assumptions defined within the coupling algorithm are satisfied.

3.2.2 High-lift Devices

In the context of modeling high-lift devices and control surfaces, two distinct methodologies can be employed:

1. Meshing control and high-lift surfaces both in the potential flow solver and high-fidelity data.
2. Meshing the clean wing in the potential solver and including deflected wing elements only in the high-fidelity data.

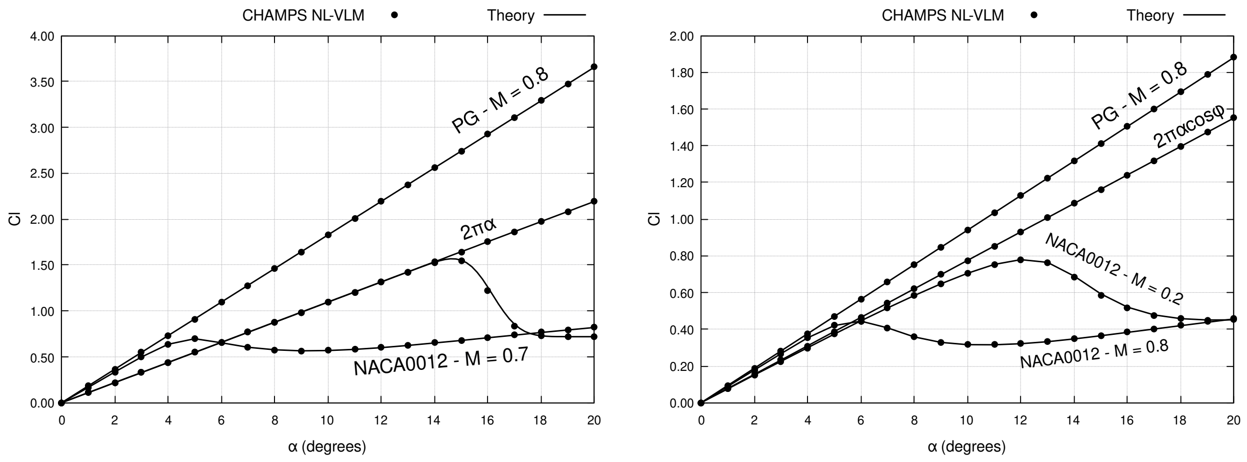

(a) Infinite straight wing (b) Infinite swept wing ($\phi = 45\,\text{deg}$)

Figure 3.13 Verification of the NL-VLM algorithm with the straight and swept infinite wing cases ($AR \sim 1 \times 10^6$)

It was found by [19] that these two approaches lead to similar results, thus categorizing the physical representation of high-lift devices as a second-order effect. Hence, a clear advantage of the second approach is that the potential flow mesh remains identical for all wing configurations of a given aircraft.

3.2.3 Artificial Dissipation

When significant nonlinear behavior is present in the input lift polars (e.g. near Cl_{max}), an artificial dissipation factor is used to obtain better convergence properties. This is done by adding a term to (3.30) [19].

$$\Delta\alpha^{n+1} = \Delta\alpha^n + \omega\left[\frac{Cl_{visc} - Cl_{inv}}{k} + \mu\delta^2(\Delta\alpha^n)\right] \tag{3.31}$$

where $\omega \in [0, 1]$ is a relaxation factor, $\mu \sim 0.1$ is the scalar dissipation factor and δ^2 is the second order central finite-difference operator. This artificial dissipation has the effect of smoothing the resulting lift distribution in cases where $\Delta\alpha$(y) is discontinuous (Figure 3.14), such as in the presence of stall cells or at the junction of high-lift devices with different deployment configurations.

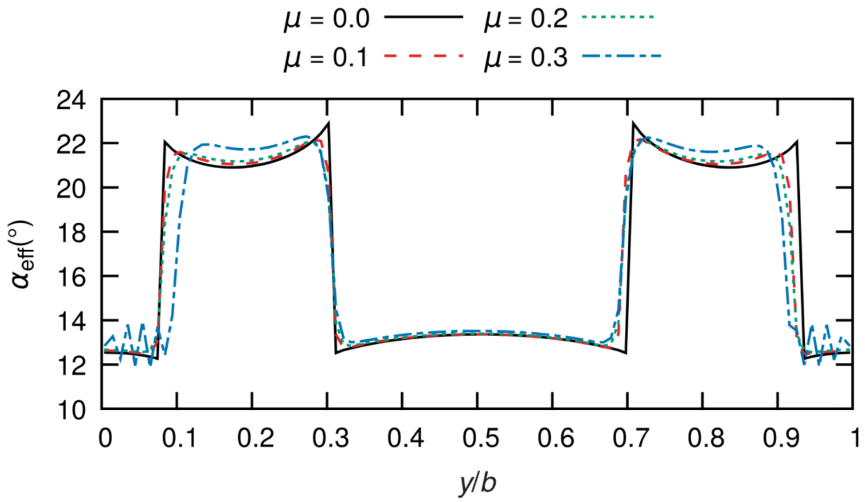

Figure 3.14 Effect of artificial dissipation coefficient μ on the spanwise distribution of effective angles of attack - [20]

3.2.4 Pitching Moment Correction

While local lift coefficients are corrected using the α-coupling algorithm, viscous drag and pitching moment coefficients remain uncorrected. Their corrected values are instead obtained from the converged α_e at the end of the solving process. For cases where the chordwise distribution of the local forces must be known with higher fidelity, the pitching moment can be introduced as a constraint so that the chordwise potential distribution matches the one found in the RANS simulation. In practice, a WLS problem is formulated for each streamwise section following the work of [43].

$$\begin{bmatrix} l_1 & l_2 & \dots & l_n \\ m_{y1} & m_{y2} & \dots & m_{yn} \end{bmatrix} \begin{Bmatrix} 1+\epsilon_1 \\ 1+\epsilon_2 \\ \vdots \\ 1+\epsilon_n \end{Bmatrix} = \begin{Bmatrix} L_{visc} \\ M_{y,visc} \end{Bmatrix} \tag{3.32}$$

where l_i and m_{yi} are the lift force and the pitching moment generated by the ith chordwise vortex-ring while L_{visc} and $M_{y,visc}$ are the total section-wise high-fidelity lift force and pitching moment. This is particularly useful when an accurate representation of the local pitching moment is necessary.

3.2.5 Handling of Fuselage Viscous Effects

As the coupling is not used for quantities on the fuselage, viscous effects are included semi-empirical drag calculations. Assuming fully turbulent flow, the viscous drag for the fuselage is given by the turbulent boundary layer solution multiplied by a user-defined form factor K.

$$C_{Dv} \simeq \frac{0.455K}{(\log Re_L)^{2.58} + (1 + 0.144M^2)^{0.65}} \frac{S_f}{S_{ref}} \tag{3.33}$$

where Re_L is the Reynolds number based on the length of the fuselage, S_f and S_{ref} are respectively the fuselage and reference areas. K may be selected using Hoerner's formula [44].

$$\begin{aligned} K &= 1 + \frac{3}{2}\left(\frac{d}{L}\right)^{3/2} + 7\left(\frac{d}{L}\right)^{3} \\ &\simeq 1.2 \quad \text{for conventional aircraft} \end{aligned} \tag{3.34}$$

3.3 Program Implementation

The nonlinear potential flow solver described in the previous sections is part of the CHAMPS aerodynamic and multidisciplinary framework. CHAMPS is written in the Chapel programming language focusing on native parallel programming and easy interfacing with various C libraries. It is using object-oriented programming principles allowing for the easy addition of modules and models in the framework. Furthermore, recent benchmarks show similar execution time and executable size as well-established programming languages such as C/C++, Fortran and Julia (Figure 3.15). For full aircraft cases, the number of elements/panels can be significant, and the execution time grows quadratically, with the main bottleneck being the calculation and assembly of the dense AIC matrices. In this regard, AIC matrices are subdivided into blocks and computed using the native `forall` directive allowing shared-memory parallelism.

In addition, since the AIC matrix is dense, the inversion of the linear system can take up to 90% of the computational time per iteration. Instead, the matrix can be pre-inverted at the beginning of the coupling algorithm and multiplied by the varying right-hand side at each iteration. This is done concretely by applying a LU factorization to the AIC and storing the result in memory. Hence, the pre-treatment procedure itself becomes slightly more expensive at the benefit of faster execution time per iteration. All linear algebra operations are performed using Chapel bindings of the popular LAPACK C library.

The current implementation of the program is capable of generating a full lift polar solution (ranging from 0° to 20° in 1° increments, computed sequentially) in approximately 20–30

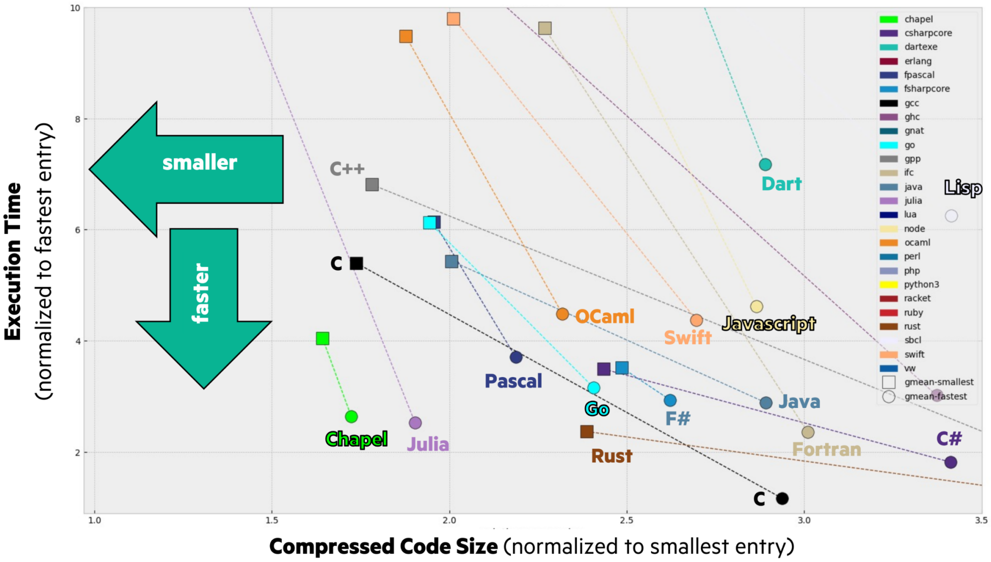

Figure 3.15 Comparison of the execution of most popular programming languages - [45]

seconds for simpler wing-only configurations. For more complex cases involving multiple bodies and/or highly nonlinear flow behaviors, the simulation time may extend up to 10–15 minutes per polar. In contrast, the equivalent simulation using CHAMPS 3D RANS can require up to 1–2 days with half the number of angles of attack. Furthermore, it is to note that the aforementioned results were obtained using an eight-core workstation computer, while the CHAMPS 3D RANS simulations were conducted on a HPC cluster leveraging several hundred computer cores.

3.4 Generation of Sectional High-Fidelity Data

2.5D RANS flow simulations are used as sectional high-fidelity for the coupling algorithm. The RANS module of the CHAMPS solver is used in that regard. It features an unstructured and cell-centered second-order finite-volume approach. The Spalart-Allmaras (SA) model is used for turbulence closure while the Roe approximate Riemann solver is used for the upwinding of the convective fluxes.

The β approach of Figure 2.6b is used for converting two-dimensional airfoils to 2.5D problems. After applying the infinite swept flow transformation given by (2.11), the 2.5D problem is formulated as follows.

$$\left\{\begin{array}{c} x' \\ y' \\ z' \end{array}\right\} = \left\{\begin{array}{c} x \\ y \\ z/\cos\phi^* \end{array}\right\} \tag{3.35}$$

$$\begin{cases} \tan\alpha' & = \tan\alpha/\cos\phi^* \\ \sin\beta' & = \cos\alpha\sin\phi^* \\ Re' & = (Re/\cos\phi^*)\frac{c}{c_{ref}} \end{cases} \tag{3.36}$$

In the case of tapered wings, the effective sweep angle ϕ^* used in the definition of the infinite swept flow problem is taken at the quarter-chord or half-chord points.

Figure 3.16 shows a verification of CHAMPS 2D/2.5D flow solver for basic airfoils. The NACA0012 validation case [46] is used as the baseline for the assessment of the flow solver, whereas the swept ONERA D airfoil [24, 47] is investigated for assessing the integration of sweep in the numerical solver using the β approach. For the low-speed straight NACA0012 ($M = 0.2$; $Re = 6 \times 10^6$), it is seen that CHAMPS is in good agreement with both numerical and experimental reference data. In the case of the transonic swept ONERA D airfoil ($M = 0.78$; $Re_{c_\perp} = 2.5 \times 10^6$), the 2.5D solutions are in excellent agreement with wind tunnel measurements at $\alpha = 0$.

The process of extracting sectional data from the three-dimensional geometry of an aircraft can be cumbersome, time-consuming and error-prone. For this matter, the pre-processing steps are automatized using a wrapper script written in Python. This program handles the following steps:

1. Discretization and extraction of the geometry in N wing sections (including multi-element/high-lift sections)
2. Preparing the geometry for CFD (sections are untwisted and normalized to unit chord)
3. Scripted unstructured quad-based mesh generation using the Pointwise software (a mesh example is given in Figure 3.17)
4. Automatic batch job submission in parallel to the HPC node (including post-processing and data retrieval)

3.5 Validation Results

The implementation of the hybrid nonlinear potential flow solver described previously is assessed in the following sections using a combination of high-lift and high-speed cases. First, a configuration build-up on the NASA Common Research Model (CRM) [48] in low-speed conditions is performed in order to assess the baseline accuracy of the solver as well as the impact of the addition of auxiliary aircraft components in the aerodynamic model.

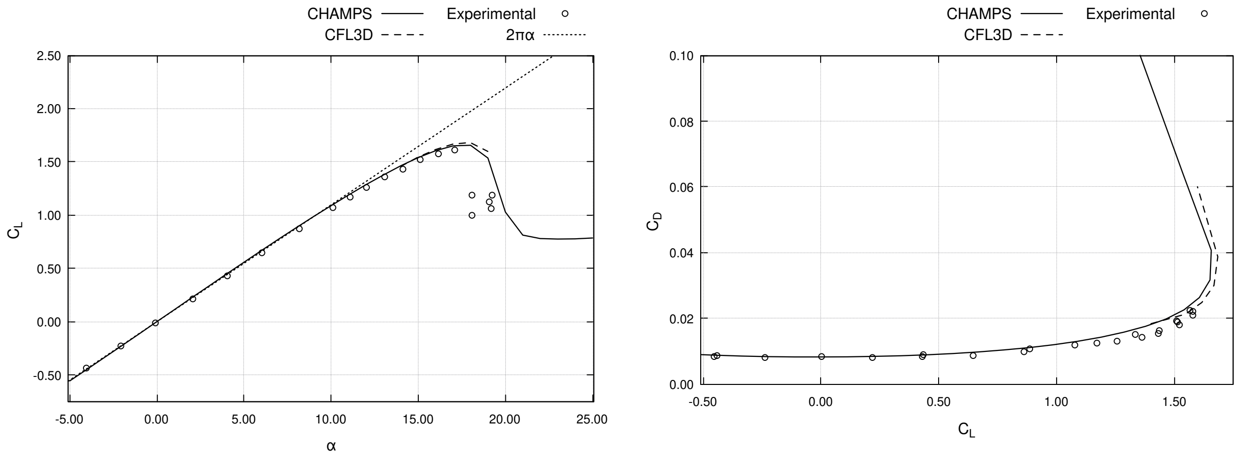

(a) 2D lift polar (NACA0012)

(b) 2D drag polar (NACA0012)

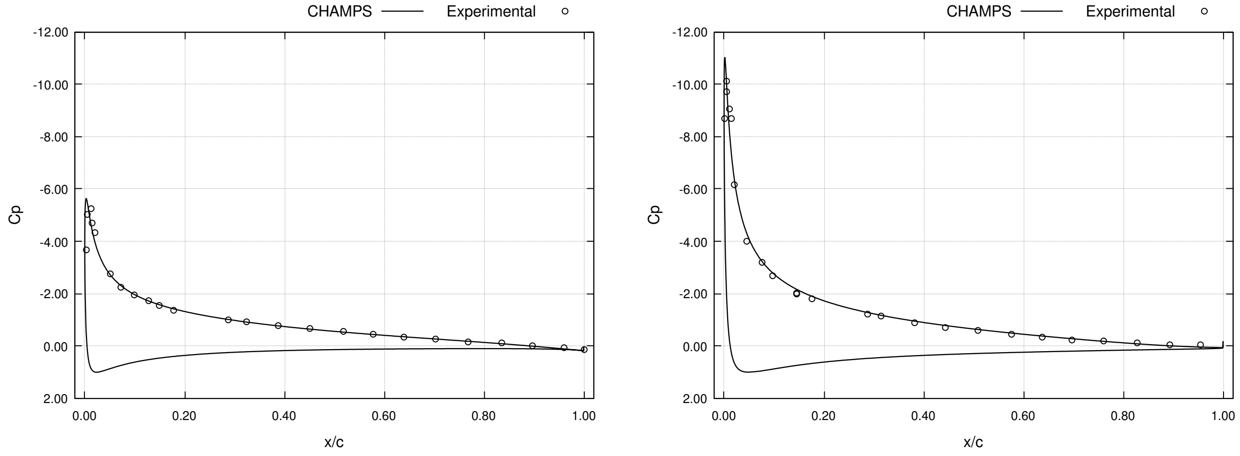

(c) 2D Cp (NACA0012) - $\alpha = 10\,\text{deg}$

(d) 2D Cp (NACA0012) - $\alpha = 15\,\text{deg}$

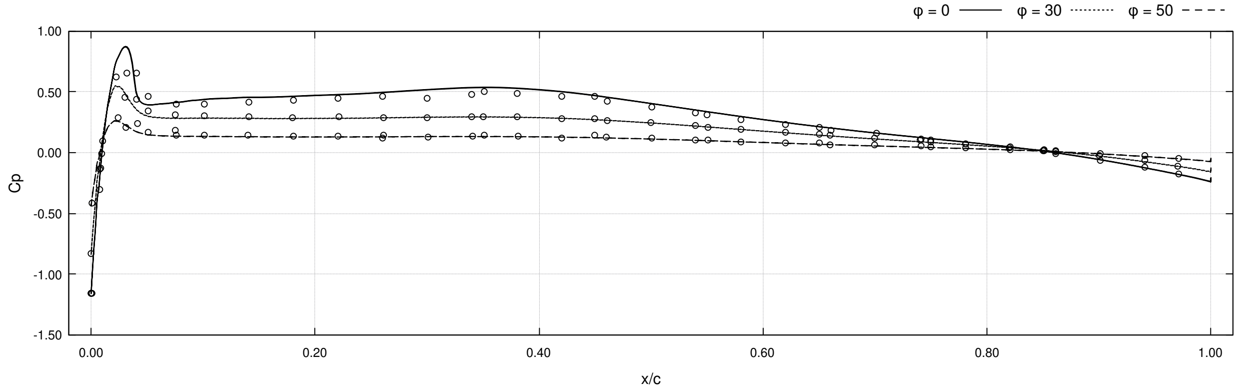

(e) Transonic 2.5D Cp (ONERA D) - $\alpha = 0$ - $\phi = 0, 30, 50\,\text{deg}$

Figure 3.16 Verification/Validation of CHAMPS 2D/2.5D flow solver. A straight airfoil is denoted 2D, whereas a swept airfoil is denoted as 2.5D.

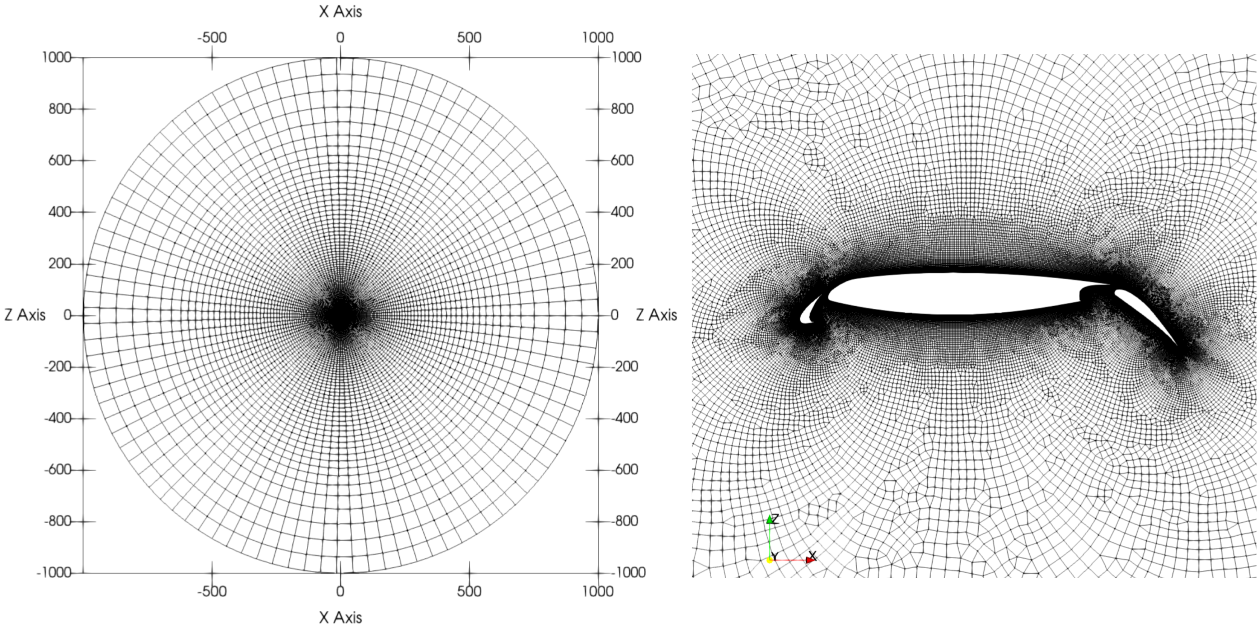

Figure 3.17 Example of β approach automatic 2.5D mesh generation using the Pointwise mesh solver. The farfield boundary is located at a distance of $1000c$ from the origin.

High-speed cases are also included for the investigation of the accuracy of the model in the upper range of the flight envelope. Results are compared with three-dimensional CFD data as well as with wind tunnel measurements provided publically within the Fifth High-Lift Prediction Workshop (HLPW5) [49] and the Sixth Drag Prediction Workshop (DPW6) [50]. For all following cases, lifting surfaces are discretized using 23 linearly-interpolated 2.5D wing sections.

3.5.1 High-Lift Common Research Model Configuration Build-Up

The investigation of the CRM in low-speed conditions is proposed in this section. The CRM is the standard configuration used in the HLPW5. The clean wing-body configuration is shown in Figure 3.18. A configuration build-up is performed at $M_\infty = 0.2$, $Re_\infty \simeq 5 \times 10^6$ based on the reference chord $c_{ref} = 275.8\, in$. The half wing span and reference area of the CRM are about $1157 in$ and $297360 in^2$, resulting in an effective aspect ratio of approximately 9.0.

Isolated Wing

The clean CRM isolated wing is first investigated as baseline results. The wing present a *Yehudi* break at around 40% of the wing span. The sectional data generated with CHAMPS

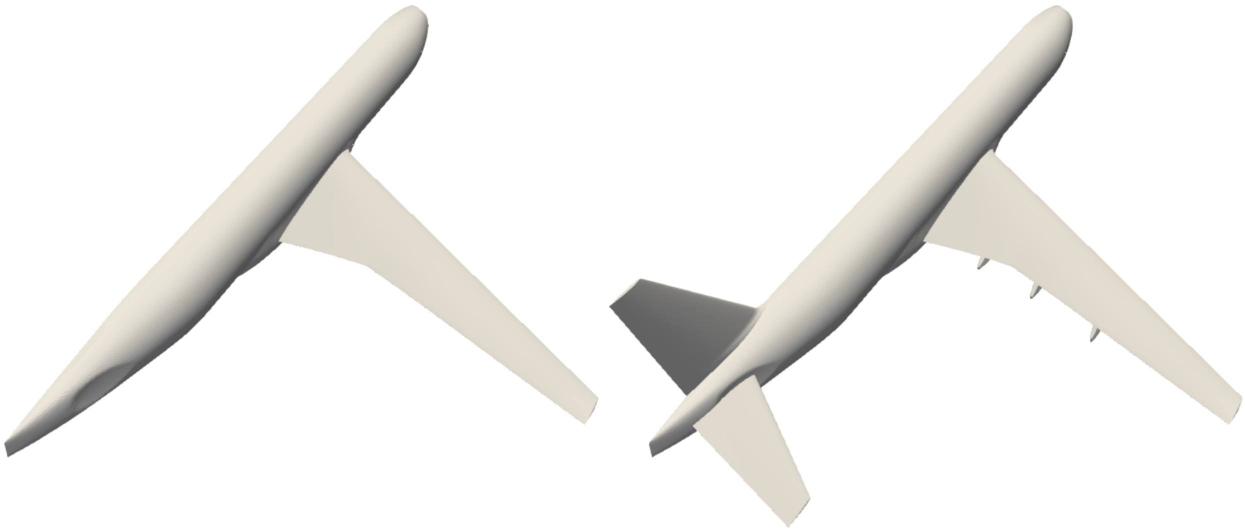

Figure 3.18 Clean CRM wing-body geometry

2.5D solver are presented in Figure 3.19. As this case is not officially part of the required cases of the HLPW5, the results are compared using in-house 3D RANS simulations performed with the TAU [51] solver on a grid of approximately 30 million cells. The VLM wing is discretized using approximately one panel per ten inches using a cosine distribution that provides increased clustering near the wing-tip, where the discretization error is generally more significant.

It is found from Figure 3.20 that the NL-VLM coupled with local 2.5D data yield good agreement with three-dimensional simulations, as pointed out by similar studies in the scientific literature. Quantitative agreement is observed in mostly linear flow conditions (i.e. $\alpha <\sim 13\,\mathrm{deg}$), while qualitative agreement is observed once $C_{L,max}$ is reached. More signifi-

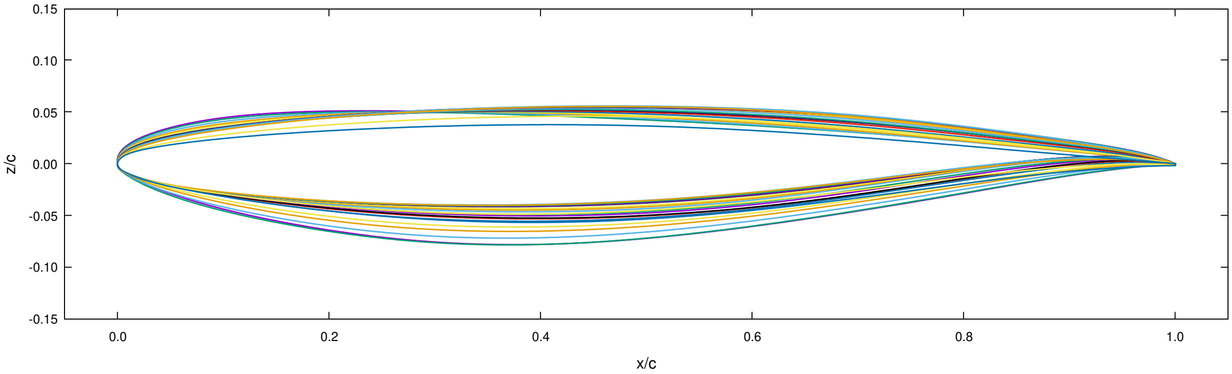

Figure 3.19 Normalized CRM wing sections used as input for the α-coupling algorithm

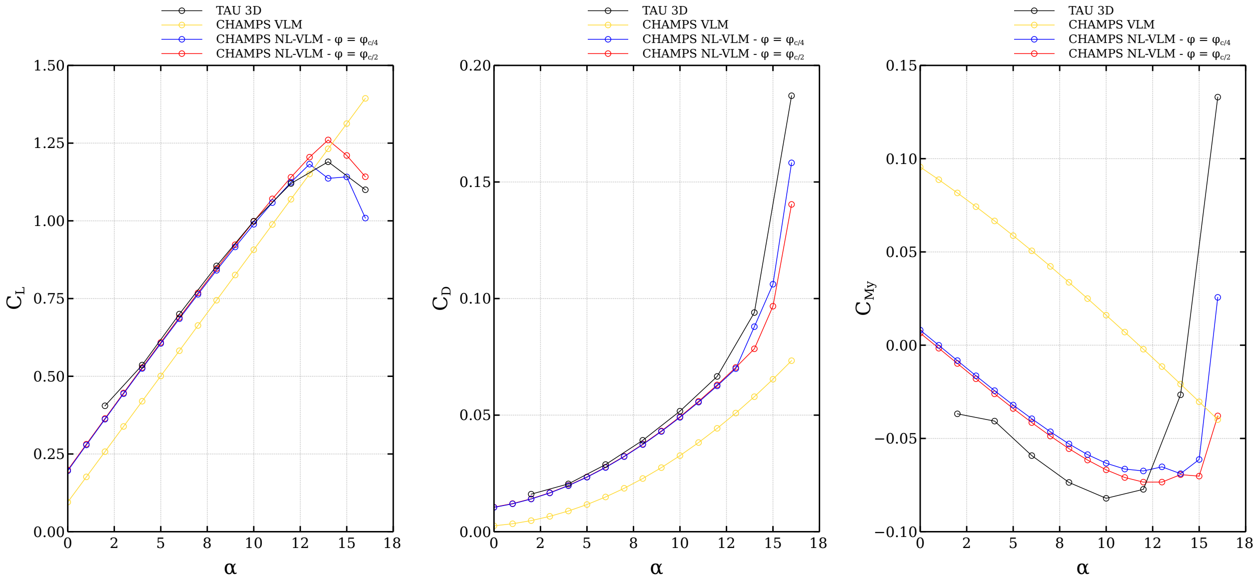

(a) (b) (c)

Figure 3.20 Force and moment coefficients on the low-speed CRM isolated wing

cant discrepancies are observed for the pitching moment, yet it still remains quite representative of the general behavior of the curve. Besides, depending on the chosen effective sweep angle, some variations in the solution is observed. In this particular case, it would seem that the effective sweep angle leading to the best agreement would be taken between the quarter-chord and half-chord points, or taken as a linear function of the two. This case proves once more that the NL-VLM can capture nonlinear phenomenons such as high-angle-of-attack low-speed flow as long as the hypothesis of locally infinite swept flow is verified.

By taking a closer look at the spanwise lift distribution, the impact of local discrepancies can be assessed more clearly. Figure 3.21 shows the propagation of stall cells in near and post stall conditions in comparison with three-dimensional RANS. As expected, good agreement with RANS is obtained in the absence of massive flow separation. However, at the predicted $C_{L,max}$ (around $\alpha \sim 14\,\text{deg}$), the NL-VLM predicts a larger separation zone than what is predicted by higher-fidelity methods at the 40% wing-span mark. This explains the underestimated value of the $C_{L,max}$ in Figure 3.20a. Nonetheless, the separation bubble appearing at the wing-tip appears to be captured with good accuracy. A similar conclusion can be taken for $\alpha = 16\,\text{deg}$, where the propagation of the stall region from the tip towards the root is overestimated.

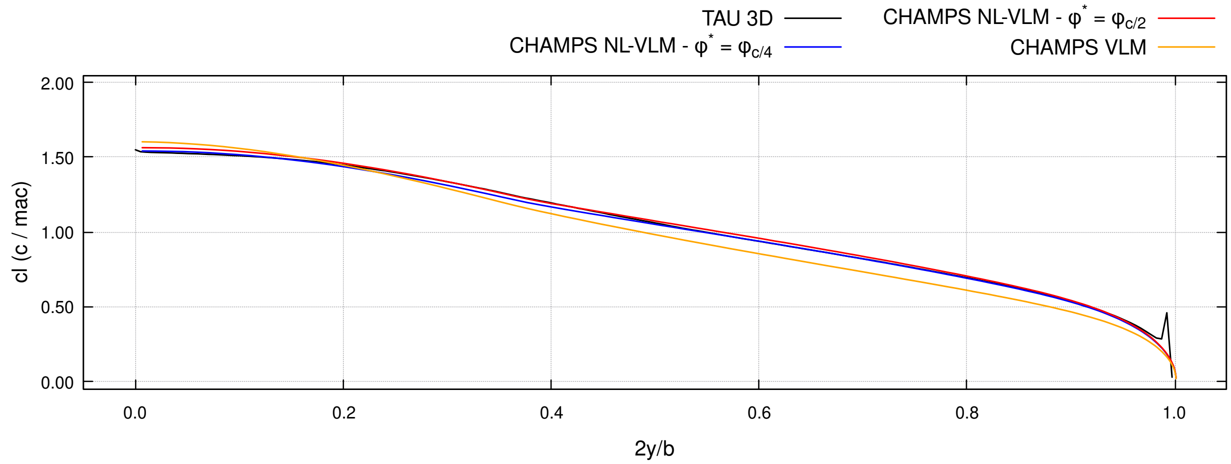

(a) $\alpha = 10.0\,\text{deg}$

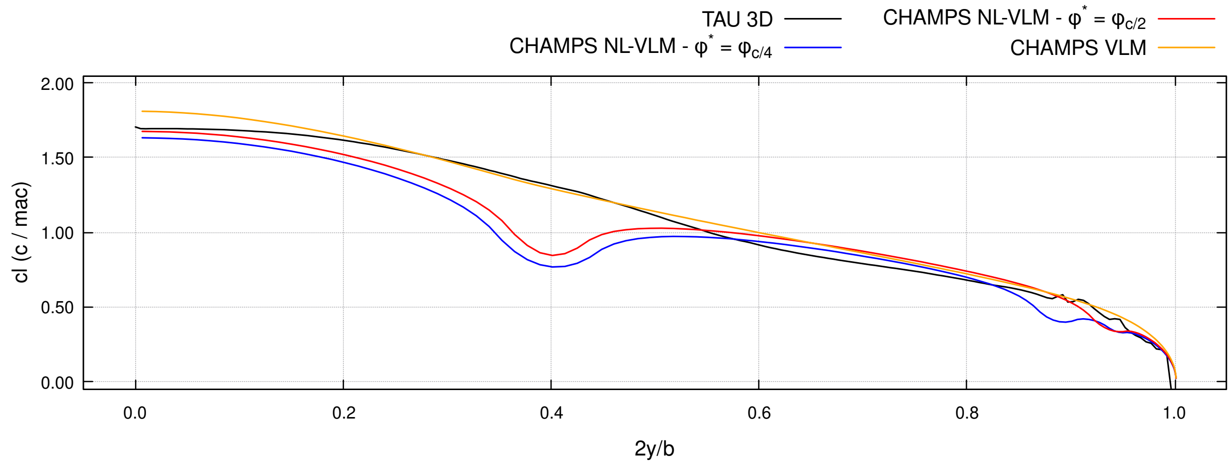

(b) $\alpha = 14.0\,\text{deg}$

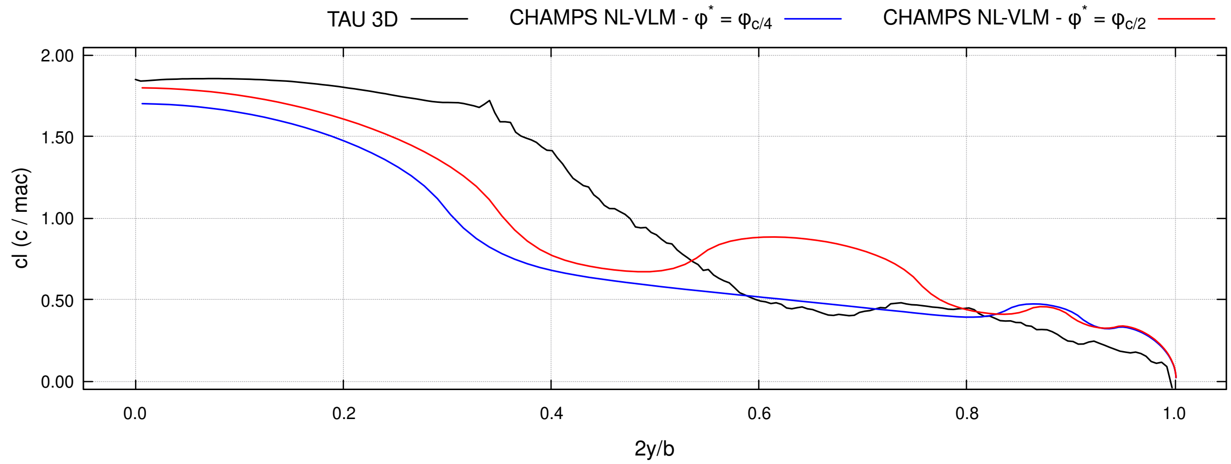

(c) $\alpha = 16.0\,\text{deg}$

Figure 3.21 Local spanwise lift coefficient on the low-speed CRM isolated wing

Wing-Body

The very first case of the HLPW5 is the study of the clean Wing-Body (WB) configuration of the CRM. For this case, participants were asked to provide a mesh refinement study at $\alpha = 11.0\,\text{deg}$ and at the same flow conditions as the previous case. The hybrid NL-VLM-Panel Method proposed in this work is leveraged for this specific problem. The fuselage is discretized using about 3000 isotropic triangles.

The global force coefficients obtained with CHAMPS NL-VLM are presented in Table 3.2 along with results provided by other participants of the workshop. As no experimental data is available as this time, the highest resolution simulation (participant W-005) is taken as the reference for the calculation of the relative error. It can be concluded from the error values that the NL-VLM yields results comparable to other higher-fidelity solutions. However, all three force coefficients are found to be underestimated. The pitching moment discrepancy as well as a significant dependency on the selected effective sweep angle are still present in this case. Yet, the error remains within a similar margin as the RANS solvers. Oddly, it would also seem that the NL-VLM results are more inline with the Wall-Modeled Large-Eddy Simulation (WMLES) results than the RANS results. It is however unclear at this stage if this difference is simply fortuitous or if a more subtle discretization/modeling mechanism is at play.

In order to understand the impact of the 2.5D hypothesis on the solution, streamwise cuts of the local forces are shown in Figure 3.22 at 17%, 61% and 95% of the wing span. This figure clearly highlights the fact that the accuracy of infinite swept flow is excellent in the mid-span region (Figure 3.22c, 3.22d), while it is degraded near the wing root (Figure 3.22a, 3.22b) where both fuselage and taper effects are non-negligible. In fact, Figure 3.22a shows erroneous values of the pressure at the stagnation point because the actual leading edge sweep angle ϕ_{LE} is larger than both $\phi_{c/4}$ and $\phi_{c/2}$ due to the non-negligible taper ratio inboard of the Yehudi. Finally, a significant discrepancy is observed near the wing tip (Figure 3.22e, 3.22f) due to the presence of a separated region that appears in the NL-VLM at a slightly larger angle of attack (see Figure 3.21).

Horizontal and Vertical Tail Planes

The following case in the HLPW5 is the CRM Wing-Body-HTP-VTP (WBHV), which consists in the addition of horizontal and vertical tail planes to the geometry as shown on the right-hand side of Figure 3.18. Furthermore, three Flap Track Fairings (FTFs) are added to the main wing. The effect of the modeling of these components in the context of the NL-VLM

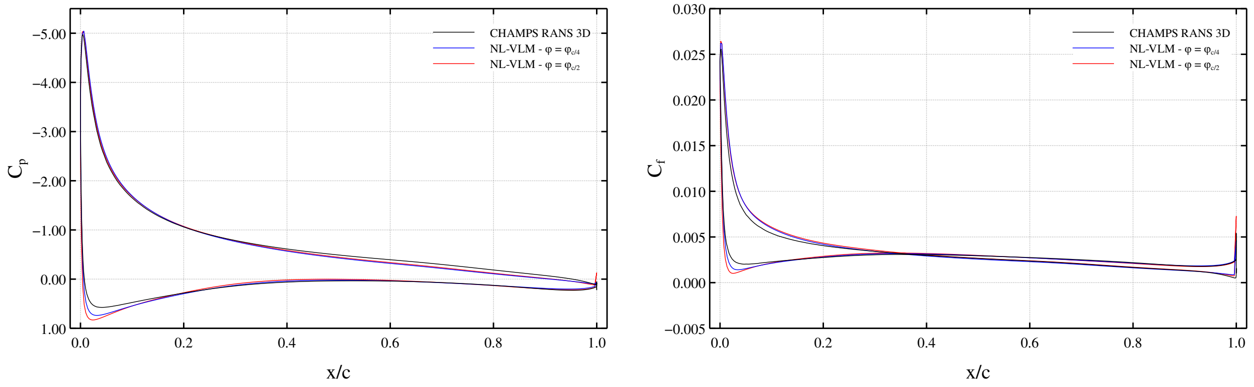

(a) Cp - $\eta = 0.17$

(b) Cf - $\eta = 0.17$

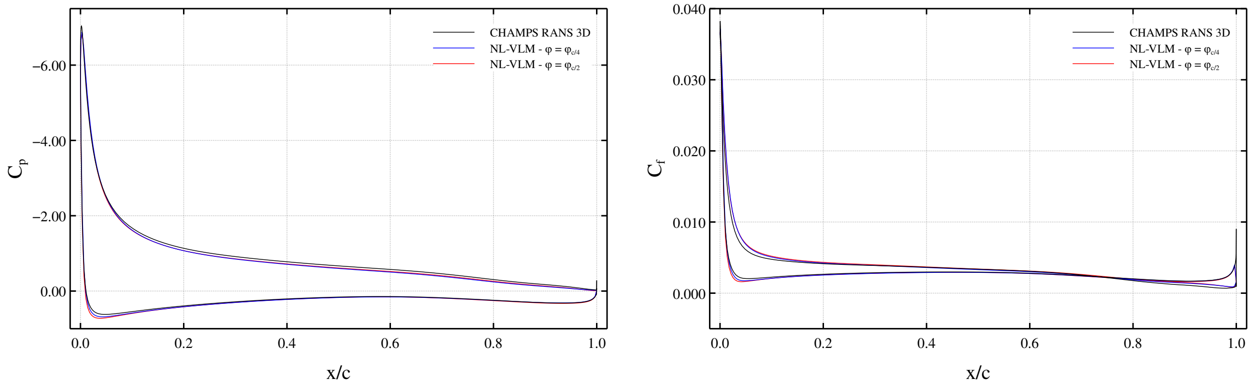

(c) Cp - $\eta = 0.61$

(d) Cf - $\eta = 0.61$

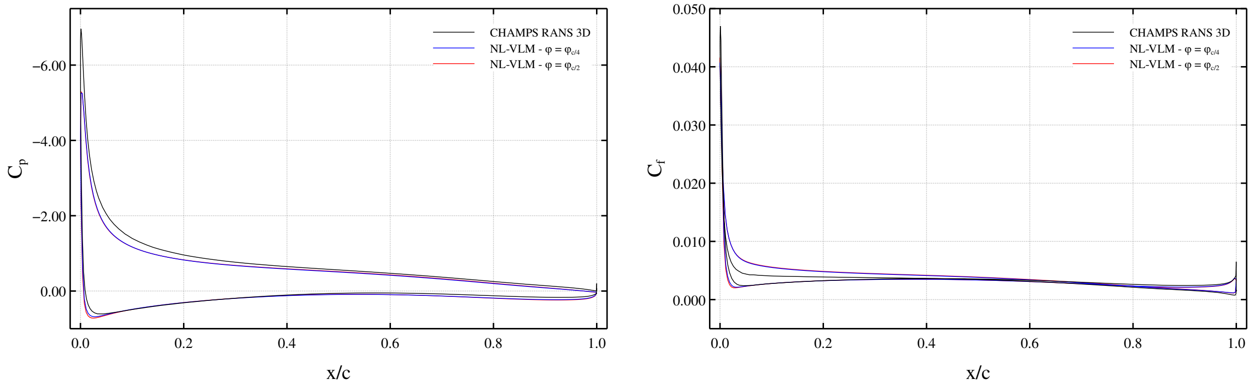

(e) Cp - $\eta = 0.95$

(f) Cf - $\eta = 0.95$

Figure 3.22 Chordwise load distribution on the clean CRM WB at $\alpha = 11.0\,\text{deg}$ and $M = 0.2$ - $\eta = 2y/b$

Table 3.2 Force coefficients on the clean configuration of the CRM WB at $\alpha = 11.0\,\text{deg}$ and $M = 0.2$. W-005 is taken as the reference for the calculation of the error.

Source	**Mesh Size**	C_L		C_D		C_{My}	
		Value	**Error**	**Value**	**Error**	**Value**	**Error**
NL-VLM - $\phi_{c/4}$	-	1.0246	-2.01%	0.0602	-4.14%	-0.0267	-39.59%
NL-VLM - $\phi_{c/2}$	-	1.0386	-0.67%	0.0607	-3.34%	-0.0353	-20.14%
RANS R-011	232 403 516	1.0762	2.93%	0.0637	1.43%	-0.0649	46.83%
RANS R-021	370 545 701	1.0785	3.15%	0.0679	8.12%	-0.0645	45.93%
WMLES W-012	228 885 243	1.0500	0.42%	0.0607	-3.34%	-0.0432	-2.26%
WMLES W-005	1 422 917 806	1.0456	-	0.0628	-	-0.0442	-

framework is briefly assessed in this section. The Horizontal Tail Plane (HTP) is coupled with 2.5D RANS while the Vertical Tail Plane (VTP) is only modelled for viscous drag using empirical formulas. The 2.5D RANS data on the HTP are performed at an effective sweep angle defined at the quarter-chord point.

Naturally, including the HTP and VTP introduces additional three-dimensional and nonlinear effects that are captured in a limited way due to the 2.5D hypothesis. Consequently, additional discrepancies in the solution are expected. In fact, Figure 3.23a shows different values of C_{L0}, resulting in a constant underestimation of the lift throughout the whole angle of attack range (the correct lift slope is recovered). Another important discrepancy resides in the slope of the pitching moment coefficient. These two observations informs that other phenomenons are at play that are not captured by the solver. One possibility is that the fixed-wake hypothesis does not hold for complex wing-tail interactions. On the other hand, it is possible that the mesh resolution used in the higher-fidelity simulations is not appropriate for the capture of this interaction. Despite these differences, good agreement is still obtained considering the simplifications of the hybrid-NL-VLM model. Indeed, the evolution of the drag coefficient (3.23c) accurately follows the trend of the higher-fidelity methods, meaning that the NL-VLM can be used to model the induced drag of complex lifting systems subject to viscous flow.

The chordwise pressure distribution along the mid-span of the HTP for various angles of attack are shown in Figure 3.24. Good agreement is observed at $\alpha = 10.0\,\text{deg}$ (Figure 3.24b), where the wing-tail interaction is moderate. At $\alpha = 6.0\,\text{deg}$ (Figure 3.24a), the fixed-wake topology intersects the HTP and causes a tighter interaction. Finally, at $\alpha = 14.0\,\text{deg}$ (Figure

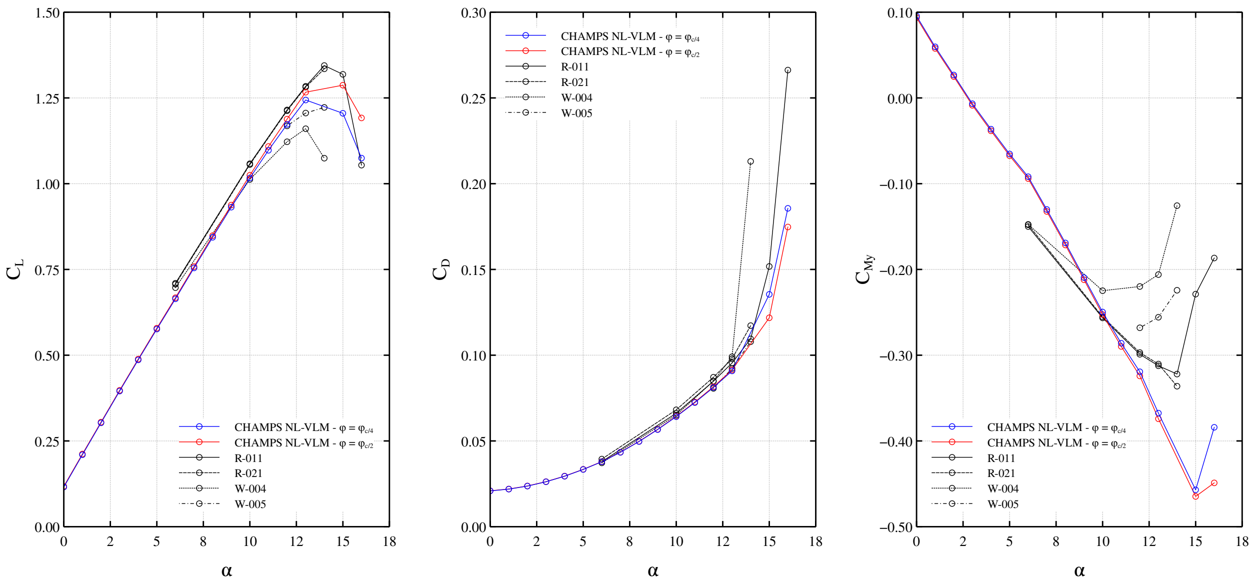

(a) (b) (c)

Figure 3.23 Force and moment coefficients on the low-speed CRM WBHV

3.24c), 3D RANS predicts heavy separation on the HTP, while the NL-VLM predicts its stall at around 16 deg. This explains the discrepancy in the pitching moment of Figure 3.23c at high angles of attack, as the loading of the HTP has a major influence on it.

Lastly, the impact of the addition of the three FTFs is considered for this case. In this regard, Figure 3.25 shows the expected jumps across each of the three FTFs. However, the infinitely thin approximation inherent to the VLM underestimates this difference when compared to three-dimensional RANS. Nonetheless, the characteristic inboard upwash and outboard downwash effects are still captured, indicating that such an approach could be used for the design or analysis of the FTFs. It is also worth mentioning that the change in local effective angle of attack caused by the FTFs creates more significant changes with the appearance of stall cells (Figure 3.25c). This could indicate that thin vertical surfaces could be used to characterize stall propagation in cases where the effect of these components is non-negligible.

High-Lift Devices

The effect of deployed high-lift devices is now investigated. The considered case is the CRM Wing-Body-Slat-HTP-VTP (WBSHV) geometry. In addition to the FTFs, this geometry includes sixteen brackets that are joining the slats to the main wing (Figure 3.26). The effect

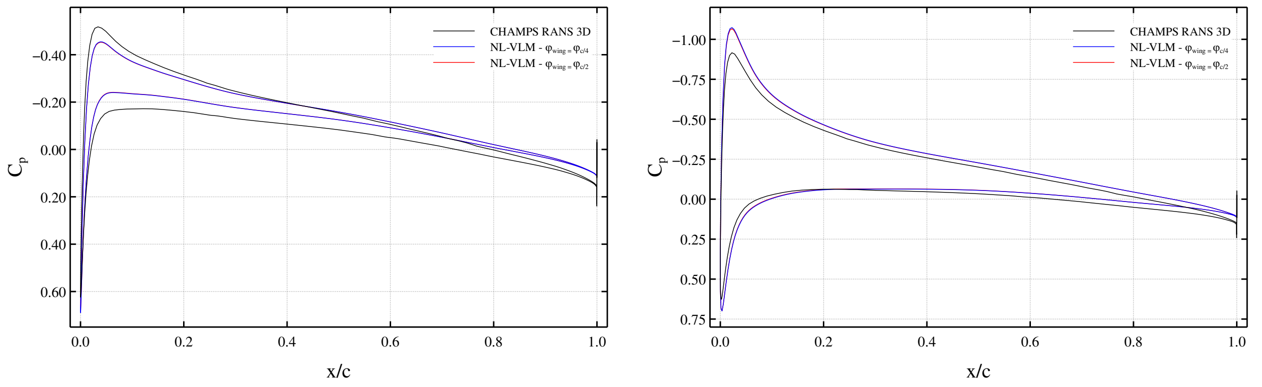

(a) $\alpha = 6.0\,\mathrm{deg}$

(b) $\alpha = 10.0\,\mathrm{deg}$

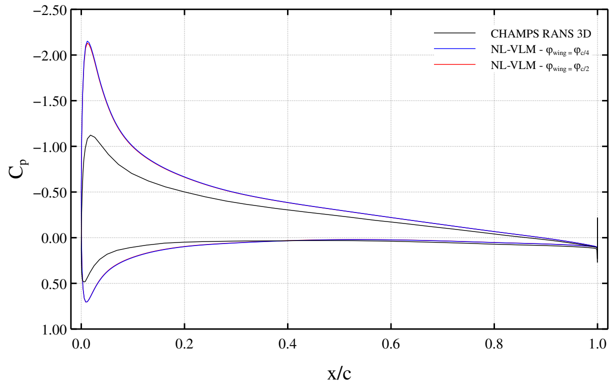

(c) $\alpha = 14.0\,\mathrm{deg}$

Figure 3.24 Chordwise pressure coefficient distribution along the low-speed CRM HTP at $\eta = 2y/b = 0.5$

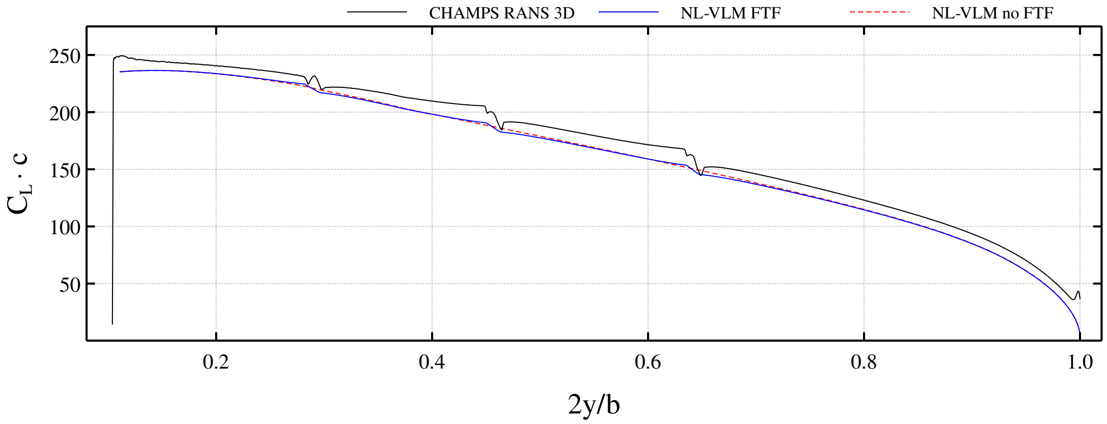

(a) $\alpha = 6.0\,\text{deg}$

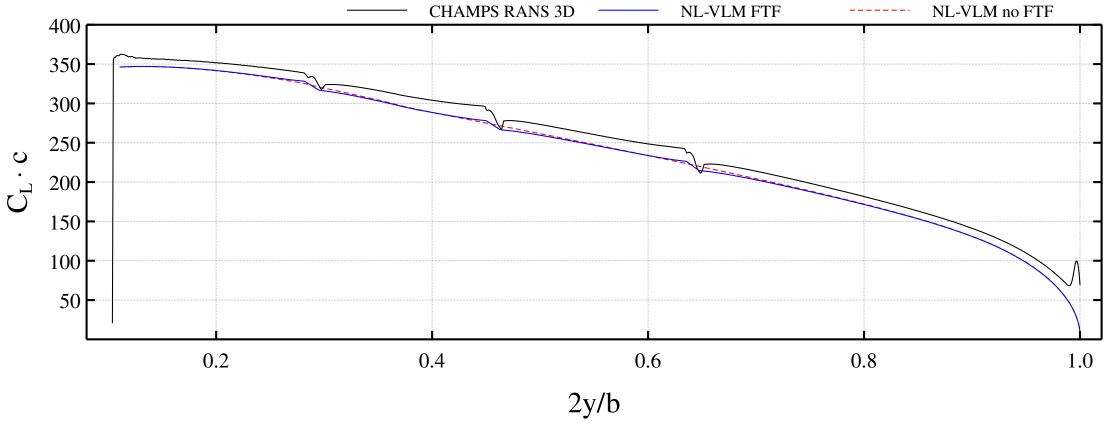

(b) $\alpha = 10.0\,\text{deg}$

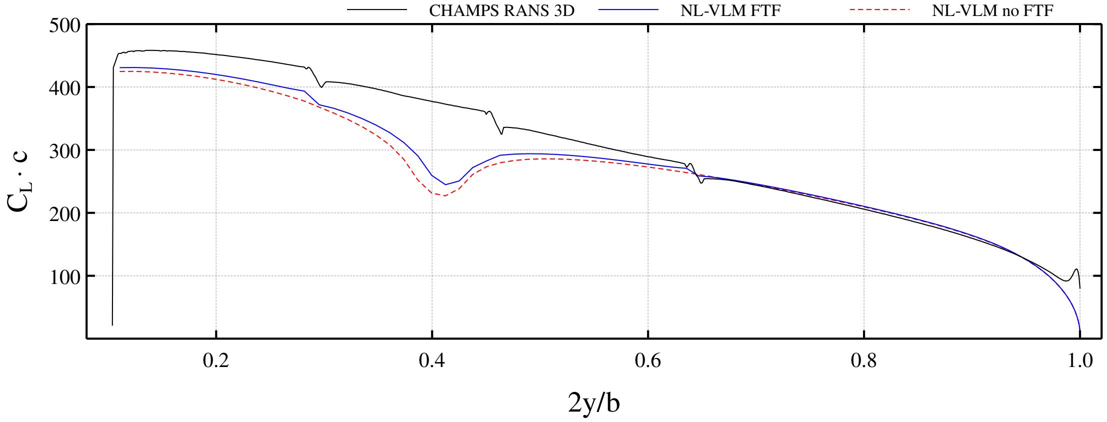

(c) $\alpha = 14.0\,\text{deg}$

Figure 3.25 Comparison of the spanwise lift coefficient with and without FTFs for the low-speed CRM WBHV of these components within the NL-VLM framework is also assessed in this section.

The results of this case are compared with RANS data from other participants as well as with wind tunnel data provided by the HLPW5 committee. Figure 3.27 illustrates this comparison for the overall forces on the aircraft. Similar conclusions as the precedent cases can be drawn. In addition, it can be noticed that the NL-VLM is in better agreement with the experimental data than 3D RANS at high angles of attack. This difference is likely due to the fact that the meshing strategies used in RANS and the NL-VLM differ significantly. In fact, the quality of meshes used in the HLPW5 was brought up many times during the workshop, where flow solutions were observed to be highly dependent on the discretization throughout the whole range of angles of attack. As the NL-VLM ultimately only require two-dimensional meshes, it is generally much easier to obtain a high quality mesh, causing the issue of discretization errors to become less significant.

A more important discrepancy can be observed in the drag polar shown in Figure 3.27b, where the drag coefficient is underestimated at higher angles of attack compared to both 3D RANS and wind tunnel measurements. By taking a closer look at RANS solutions, it was found that the presence slat brackets induces trailing vortices that cause cones of separated flow (referred to as *pizza slices* in the literature). The hypothesis is that these increased separation zones at higher angles of attack are responsible for this deviation in the drag coefficient, as shown in Figure 3.28a and 3.28d.

An attempt at modelling the effects of slat brackets using thin vertical surfaces within the NL-VLM as been performed, and the impact on the local skin friction coefficient is shown in Figure 3.28. In comparison to RANS, it seems that the effect of the slat brackets is underestimated, although some subtle discontinuities in the spanwise distribution of the C_f

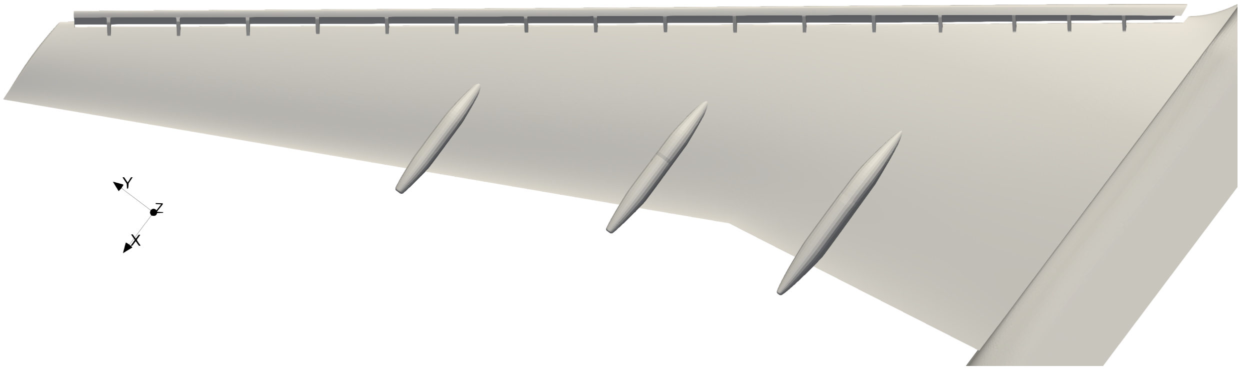

Figure 3.26 Representation of the sixteen slat brackets on the CRM WBSHV. These brackets can be approximated as thin vertical surfaces in the context of the NL-VLM.

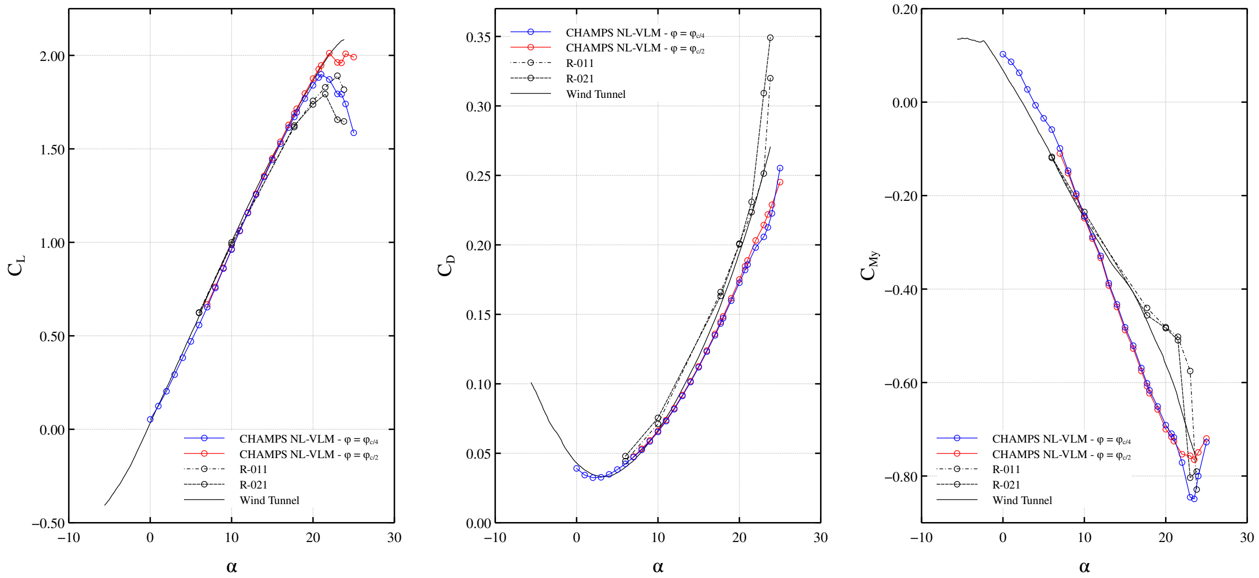

(a) (b) (c)

Figure 3.27 Force and moment coefficients on the low-speed CRM WBSHV

can be observed where the brackets are present. The locations of stalled regions also differ, as the separation zones are not captured in the same way. This difference is explained by the fact that the coupling data is not aware of the presence of the slat brackets. Consequently, although the streamwise 2.5D RANS sections are interpolated at a slightly altered effective angle of attack, the separated flow zone behind the brackets does not exist in the pre-generated database. The influence of the brackets on the local velocity field would need to be taken into account at the time of generating the 2.5D database for the effect be captured similarly as 3D RANS.

Landing Configuration

In this last section concerning the HLPW5, the CRM in landing configuration with nacelles and pylons is investigated. The pylon is modelled as a thin vertical surface, similarly to the previous cases, while the nacelle is modelled as a panel shell made of a few thousand triangles. The full surface mesh for the potential flow simulation is shown in Figure 3.29.

Figure 3.30 illustrates the global forces obtained for the full landing configuration. At first glance, a significant discrepancy for all three aerodynamic coefficients can be noticed between the results of the NL-VLM and the high-fidelity measurements and calculations. The exact origin of this discrepancy is unknown due to the lack of available local data for comparison.

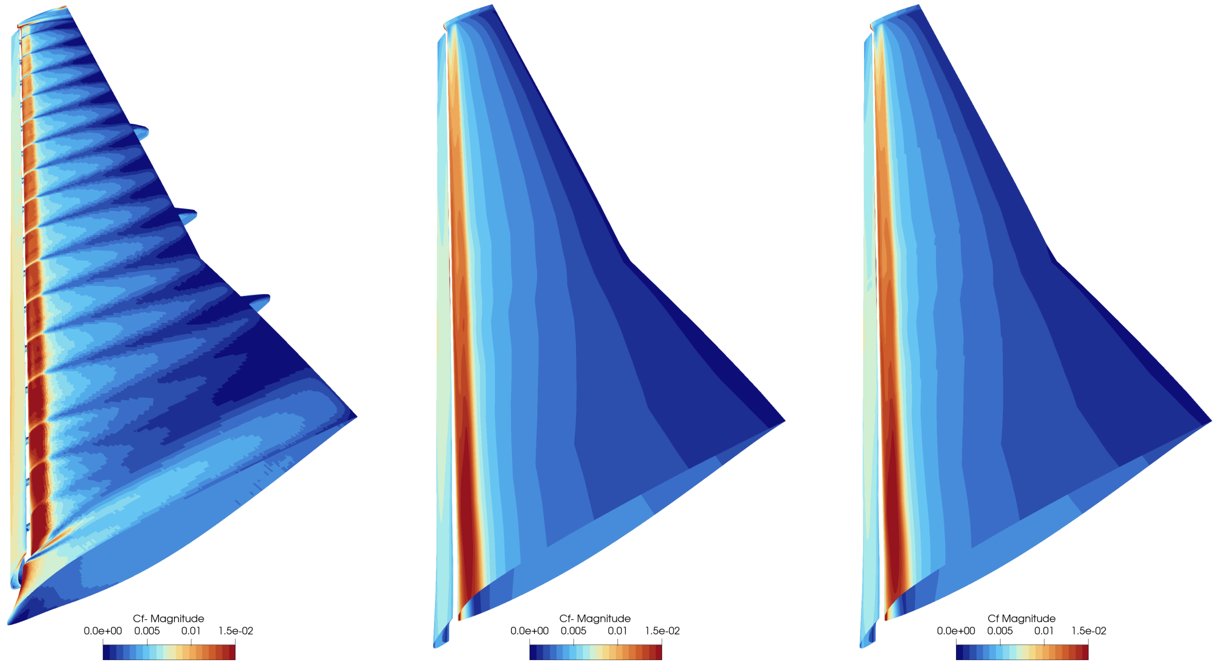

(a) 3D RANS - $\alpha = 10.0\,\text{deg}$ (b) NL-VLM brackets OFF - $\alpha = 10.0\,\text{deg}$ (c) NL-VLM brackets ON - $\alpha = 10.0\,\text{deg}$

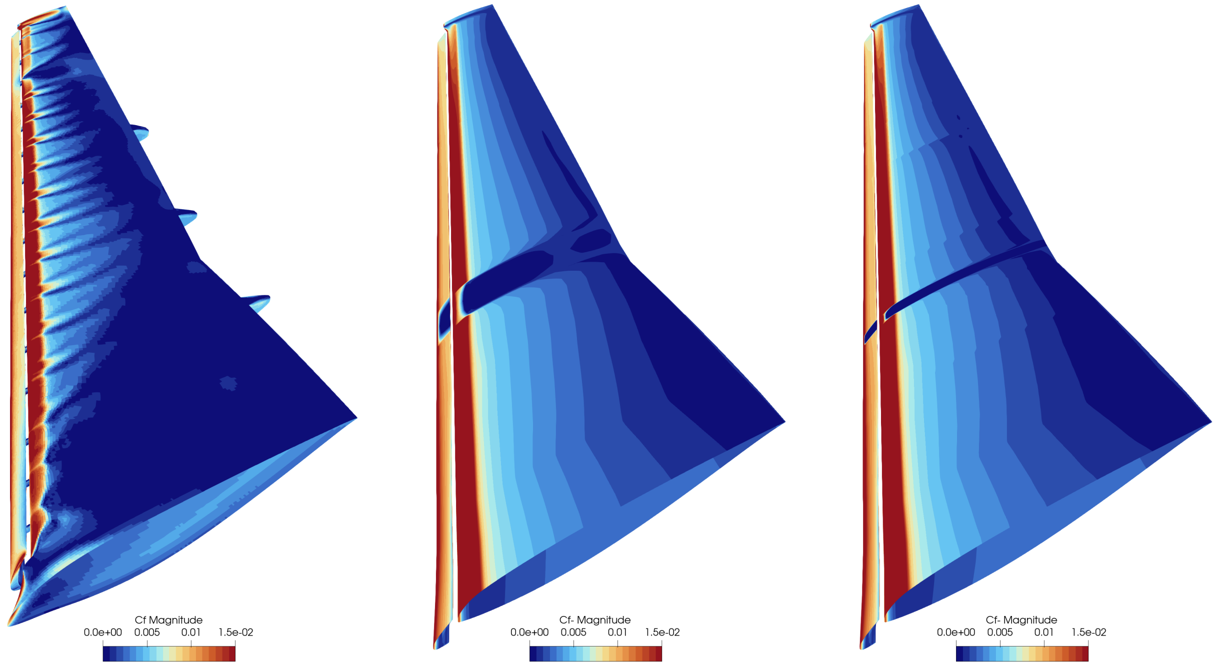

(d) 3D RANS - $\alpha = 23.0\,\text{deg}$ (e) NL-VLM brackets OFF - $\alpha = 23.0\,\text{deg}$ (f) NL-VLM brackets ON - $\alpha = 23.0\,\text{deg}$

Figure 3.28 Effects of the modeling of slat brackets on the skin friction forces of the CRM WBSHV

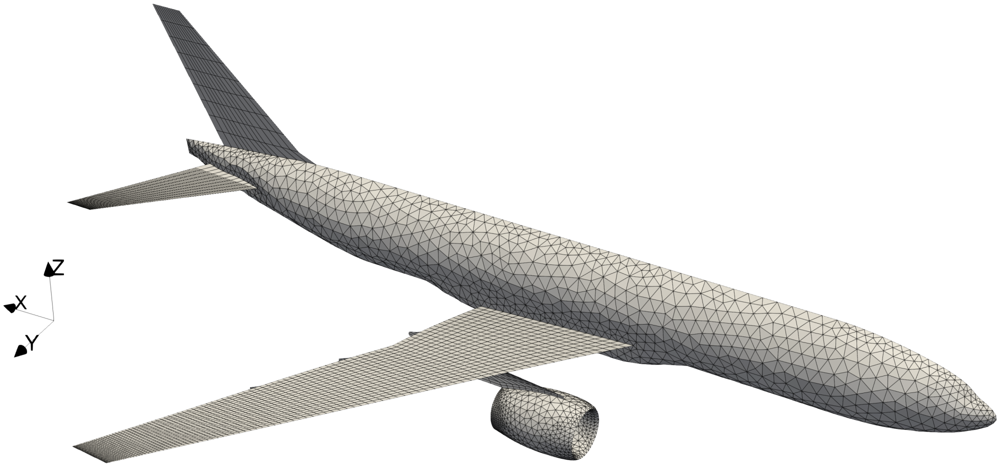

Figure 3.29 Full surface mesh used in the hybrid NL-VLM method

A plausible explanation is that the complex interaction between the strong vortex induced by the flaps with the fuselage lead to underestimated lift, and therefore underestimated induced drag. Nonetheless, this difference is mostly constant throughout the whole angle of attack range for all three curves, indicating that most of the flow physics are well captured.

Figure 3.31 illustrates a comparison between the same quantities with the constant gap removed. In this graph, it is possible to see that most of the features shown in the experimental measurements are also well captured by the NL-VLM. The correct lift slope (Figure 3.31a) is once again adequately estimated, while the $C_{L,max}$ is slightly overestimated but within an acceptable range. Some nonlinear characteristics present in Figure 3.31b and 3.31c are also present. For example, a slight inflexion point in the evolution of the drag coefficient at $\alpha \sim 20\,\text{deg}$ seems to be well modelled when taking the effective sweep at the quarter-chord point. This phenomenon is also present in the pitching moment curve. Lastly, similar conclusions as the precedent case concerning the increase in drag at higher angles of attack due to the slat-bracket-induced flow separation can be drawn.

3.5.2 High-Speed Common Research Model Configuration Increment

In this section, a validation of the current model in transonic conditions is performed. The CRM Wing-Body-HTP (WBH) and Wing-Body-HTP-Nacelle-Pylon (WBHNP) with pre-calculated aeroelastic deflections are investigated as stated in the second case of the DPW6. The simulation is carried out at $M = 0.85$, $Re = 5\times10^6$ and at a target $C_L = 0.5000\pm0.0001$, where the target is achieved iteratively using a bisection algorithm. The main objective of the case is to measure the drag increment caused by the addition of the nacelle and pylon

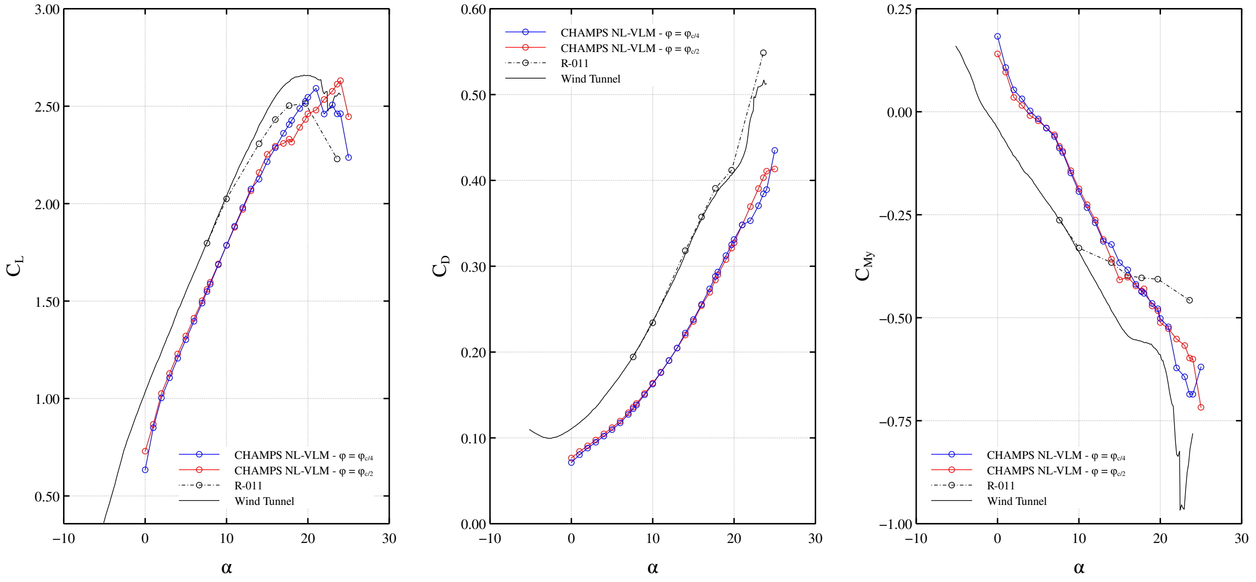

(a) (b) (c)

Figure 3.30 Force and moment coefficients on the low-speed CRM in landing configuration

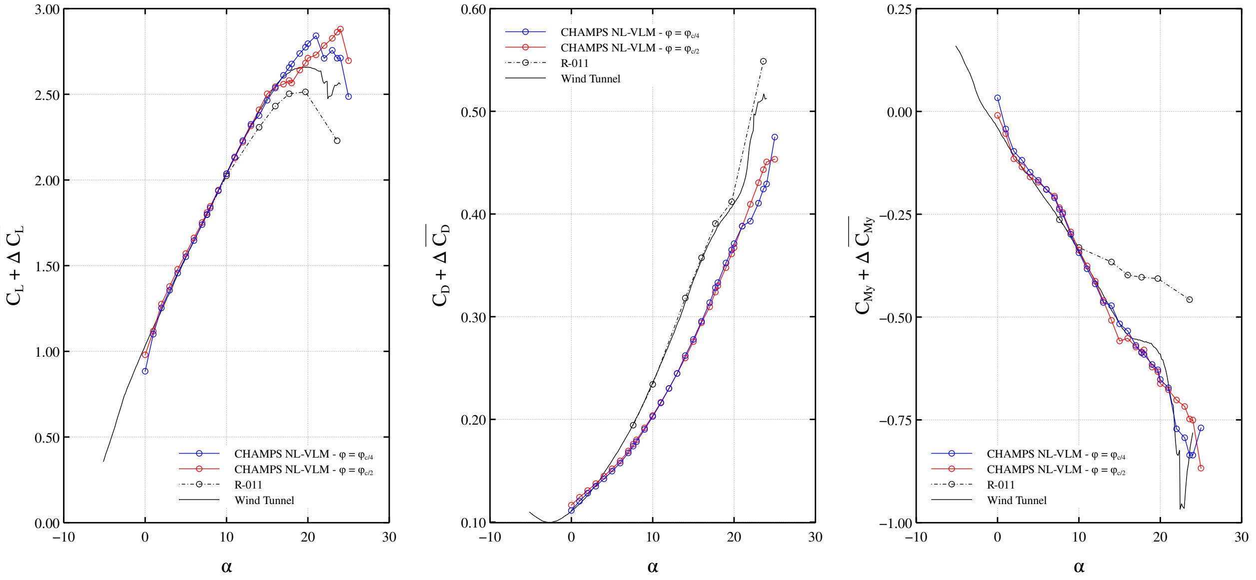

(a) (b) (c)

Figure 3.31 Corrected force and moment coefficients on the low-speed CRM in landing configuration. $\bar{C}L$, $\bar{C}D$ and $C\bar{M}y$ are added to the NL-VLM results based on the constant mean difference between the two methods.

to the aircraft. 3D RANS simulations as well as wind tunnel data provided publically in the context of the workshop are used as reference data.

Table 3.3 shows a comparison of the absolute and relative values of the drag and pitching moment coefficients for the NL-VLM and reference sources. While a non-negligible difference exists between the absolute values of the drag and pitching moment coefficients, the increment between the two configurations seems in good agreement with the reference. For example, a delta of seven drag counts is found between the results of the best NL-VLM results and wind tunnel measurements.

Streamwise cuts of the surface pressure field explain the discrepancy observed in the absolute values of the drag and pitching moment coefficients. Indeed, Figure 3.32 illustrates how the 2.5D hypothesis fails near the wing root. Figure 3.32b shows that the strength of the shock is largely overestimated despite its accurate location, while Figure 3.32a indicates massively detached flow at the wing-body junction. It is interesting to note that this separation pattern at the root is also present in 3D RANS solutions, but at a larger angle of attack.

Furthermore, choosing the effective angle of attack at the mid-chord point yields better agreement with both 3D RANS and experimental measurements than at the quarter-chord point. This is in agreement with the three-dimensional solution, where the main shock follows the mid-chord point throughout the most part of the wing. Finally, the shape of the pressure distribution at 73% of the wing-span (Figure 3.32c) shows that the 2.5D hypothesis remains mostly valid for negligible wing taper and root/tip effects.

Table 3.3 Force coefficients on the CRM WBH and WBHNP at $C_L = 0.5000 \pm 0.0001$ and $M = 0.85$. Δ represents the increment of a value after the addition of the nacelle and pylon.

Source	C_D WBH		ΔC_D		C_{My} WBH		ΔC_{My}	
	Value	**Error**	**Value**	**Error**	**Value**	**Error**	**Value**	**Error**
NL-VLM $\phi_{c/2}$	0.0292	12.31%	0.0030	0.0007	-0.1795	77.02%	0.0366	0.0304
NL-VLM $\phi_{c/4}$	0.0315	21.15%	0.0051	0.0028	-0.1036	2.17%	0.0543	0.0481
TAU 3D RANS	0.0260	-	0.0022	-0.0001	-0.1014	-	0.0062	-
Wind Tunnel	-	-	0.0023	-	-	-	-	-

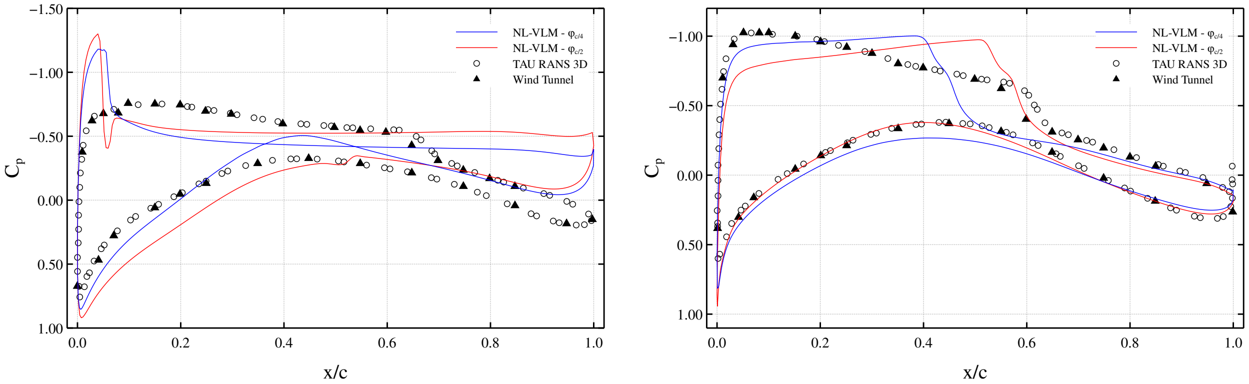

(a) $\eta = 0.131$

(b) $\eta = 0.283$

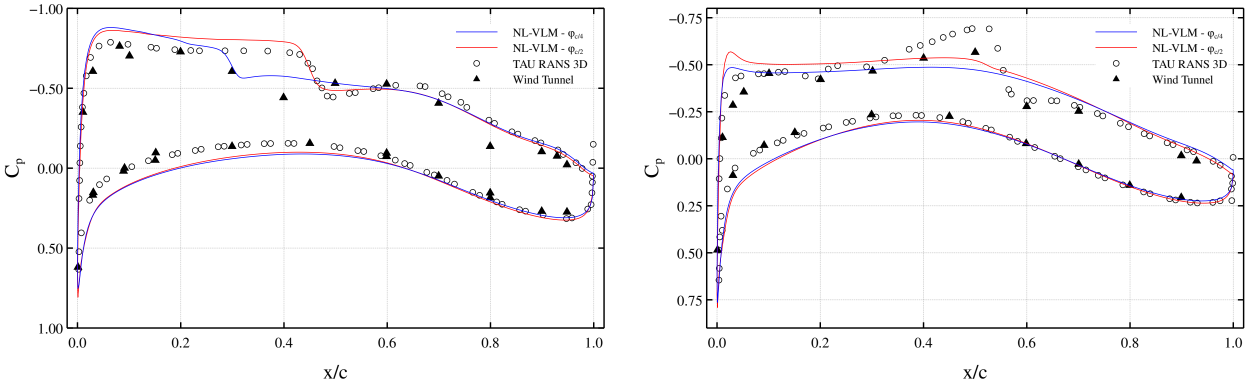

(c) $\eta = 0.727$

(d) $\eta = 0.950$

Figure 3.32 Chordwise pressure coefficient distribution along the CRM WBH at $C_L = 0.5$ and $M = 0.85$

3.6 Discussion

In the precedent sections, the medium-fidelity solver proposed in this work has been put to the test in various flow conditions and configurations. In most cases, excellent agreement was observed with both three-dimensional flow solvers and wind tunnel experiments. These cases prove that nonlinear potential flow methods are suitable for the study of complex aircraft configurations in low-speed high-angle-of-attack as well as in transonic conditions. The addition of a fuselage, HTP and VTP as well as other aircraft components allowed to recover most of the physics of interest. These results are particularly impressive considering that the entirety of the cases presented in this work can be run serially under an hour on most personal workstations, while the 3D RANS equivalent would take several days of runtime on a HPC cluster.

Nonetheless, certain limitations were highlighted in the validation process.

1. The fixed-wake hypothesis was shown to yield discrepancies when the wing-tail interaction was noneligible. Most of the differences were found on the pitching moment polar, while the influence on drag was more subtle.

2. The modelling of slat brackets and thin vertical surfaces was shown to yield inadequate predictions of the skin friction forces. Coupling the velocity field induced by these components at the time of generating the 2.5D database could help to introduce additional three-dimensional effects to the model.

3. A significant dependency on the chosen effective sweep angle was observed in the presence of highly nonlinear phenomenons (e.g. near-stall and transonic conditions).

The latter is a significant limitation of the NL-VLM, as choosing the wrong effective sweep angle can lead very poor accuracy. This is mostly due to the fact that multiple flow topologies each happen according to the orientation of the local isobars. For example, it is impossible to capture correctly a leading edge stagnation line at the same time a shock at the mid-chord point, as both of these phenomenons are characterized and are highly dependent on different sweep angles in the case of a tapered wing. An attempt at solving this issue is addressed in the following chapter.

CHAPTER 4 DEVELOPMENT OF A 2.75D FLOW SOLVER ACCOUNTING FOR TAPER EFFECTS

It was noticed in previous sections that the Infinite Swept Flow Theory reaches its limit when non-negligible taper is introduced in the geometry of interest. As a remedy, an effective sweep angle ϕ^* had to be assumed in order to obtain an approximate result. However, as mentioned previously, using this approach only approximate flow topologies (Figure 2.5). This approximation is quite significant in transonic flow conditions, where the location and orientation of the main shock depends heavily on the prescribed ϕ^*, which is dependent on the case.

The objective of this section is to attempt to extend a 2.5D infinite swept flow RANS solver to include the effects of taper (2.75D). This alternate solver is based on the conical flow assumption, which assumes a null flux along rays emanating from the apex created by the convergence point of a wing's leading and trailing edges (Figure 2.8).

4.1 Governing Equations

Similarly to the 2.5D method, the proposed 2.75D method is built directly by simplifying the three-dimensional compressible Navier-Stokes system (given as a reference in (1.1)). Furthermore, in order to simplify the equations according to the conical flow assumption, a coordinate transform must first be defined so that the proper flux terms can be cancelled out when necessary.

4.1.1 Coordinates Transformation

First, an arbitrary frame of reference (ξ, η, ζ) is defined according to the following potentially nonlinear transformation.

$$\begin{Bmatrix} dx \\ dy \\ dz \end{Bmatrix} = \mathbf{J}(\xi, \eta, \zeta) \cdot \begin{Bmatrix} d\xi \\ d\eta \\ d\zeta \end{Bmatrix} \tag{4.1a}$$

$$\mathbf{J} \equiv \frac{\partial(x, y, z)}{\partial(\xi, \eta, \zeta)} \tag{4.1b}$$

$$J \equiv \det(\mathbf{J}) \tag{4.1c}$$

Applying this transformation directly to the Navier-Stokes equations using the chain rule and after expanding the dyadic product $\mathbf{V} \otimes \mathbf{V}$, the conservative contravariant form of the

Navier-Stokes system is obtained (using Einstein notation)

$$\frac{\partial(J\rho)}{\partial t} + \partial_i(J\rho U_i) = 0 \tag{4.2a}$$

$$\frac{\partial(J\rho U_j)}{\partial t} + \partial_i(J\rho U_j U_i + p\delta_{ij}) - \partial_i(J\tau^{ji}) = J(S_j^{1c} + S_j^{1v}) \tag{4.2b}$$

$$\frac{\partial(J\rho E)}{\partial t} + \partial_i(J\rho U_i H) - \partial_i(J\tau^{ji}u_i) = JS^{2v} \tag{4.2c}$$

with the transformed contravariant velocity defined as the following.

$$\mathbf{U} \equiv \mathbf{J}^{-1}\mathbf{V} \tag{4.3}$$

The contravariant metric tensor g^{ij} defining the metric quantities of the transformed coordinate system is obtained from the inverse of the covariant metric tensor g_{ij}, which in turn is related to the differential arc length ds in the transformed coordinate system.

$$ds^2 = g_{ij} d\xi_j d\xi_i \tag{4.4}$$

Lastly, the expansion of covariant derivatives in a non-Euclidean space also generate additional terms, which are shown in the right-hand side of (4.2b) and (4.2c) as S^1 and S^2. These terms are function of the Christoffel Symbols of the second kind Γ^j_{ik}, which are specific to a given coordinate system and are obtained from the following general relation.

$$\Gamma^j_{ik} = \frac{1}{2}\sum_m g^{jm}\left(\frac{\partial g_{mi}}{\partial \xi_k} + \frac{\partial g_{mk}}{\partial \xi_i} - \frac{\partial g_{ik}}{\partial \xi_m}\right) \tag{4.5}$$

Convective Source Term

The convective source term appears after the expansion of the dyadic product in the momentum equations. Furthermore, the conservative formulation of the pressure flux, obtained by including $p\delta_{ij}$ in the divergence term, creates additional terms in the momentum equation. Using the chain rule as well as the covariant derivative definition, the following formula is obtained.

$$S_j^{1c} = -\rho\Gamma^j_{ik} U_k U_i - S_j^p \tag{4.6}$$

where S_j^p is the pressure flux term and is dependent on the metrics of the chosen frame of reference.

Viscous Flux and Source Terms

The viscous source term appears in the momentum and energy equations due to the divergence of the viscous stress tensor. Additionally, the stress tensor itself includes covariant derivatives as well as divergences of the velocity vector. Consequently, its formulation is significantly more involved than its counterpart in cartesian coordinates.

For a general coordinate system, the covariant Newtonian viscous stress tensor is defined from the following relation

$$\tau_{ij} = \mu(\nabla_j u_i + \nabla_i u_j) + \lambda g_{ij} \partial_i U_i \tag{4.7}$$

where ∇_i and u_i are the covariant derivative and covariant velocity vector, respectively. μ and $\lambda = -2\mu/3$ are the dynamic and second viscosity coefficients. Expanding the covariant derivatives once more, the covariant viscous stress tensor takes the following form.

$$\tau_{ij} = \mu(\partial_j u_i + \partial_i u_j - 2\Gamma^k_{ij} u_k) + \lambda g_{ij} \partial_i U_i \tag{4.8}$$

The contravariant viscous stress tensor is obtained using a double contraction with the contravariant metric tensor.

$$\tau^{ij} = g^{ik} g^{jl} \tau_{kl} \tag{4.9}$$

Finally, the covariant derivative (i.e. divergence) of τ^{ij}, a contravariant second order tensor, is given as follows.

$$\nabla_j \tau^{ij} = \partial_j \tau^{ij} + \Gamma^k_{mj} \tau^{mj} + \Gamma^j_{mj} \tau^{km} \tag{4.10}$$

The first term in (4.10) is the viscous momentum flux term, while the other ones are part of the momentum source term.

$$S^{1v}_j = -(\Gamma^k_{mj} \tau^{mj} + \Gamma^j_{mj} \tau^{km}) \tag{4.11}$$

As for the viscous work terms, a similar procedure is performed and the following flux and source terms are obtained.

$$\nabla_j (\tau^{ji} u_i) = \partial_j (\tau^{ji} u_i) + \Gamma^j_{mj} \tau^{mi} u_i + \Gamma^i_{mj} \tau^{mj} u_i - \tau^{ji} \Gamma^m_{ij} u_m \tag{4.12}$$

$$S^{2v} = \tau^{ji} \Gamma^m_{ij} u_m - \Gamma^j_{mj} \tau^{mi} u_i - \Gamma^i_{mj} \tau^{mj} u_i \tag{4.13}$$

Due to the inherent complexity of the viscous fluxes, their effects are neglected in the scope of this work. Consequently, the following sections are focused on the discretization of the Euler equations.

4.1.2 Conical Flow Transformation

In order to apply the assumption of conical flow, the fluxes along the radial component originating from the apex of the tapered wing must be zero. Consequently, the spherical coordinate system (r,θ,ϕ) is selected as the transformation basis. After derivation, the following metric quantities are found for the spherical frame of reference.

$$\begin{Bmatrix} x \\ y \\ z \end{Bmatrix} = \begin{Bmatrix} r\sin\theta\cos\phi \\ r\sin\theta\sin\phi \\ r\cos\theta \end{Bmatrix} \tag{4.14a}$$

$$\mathbf{J} = \begin{bmatrix} \sin\theta\cos\phi & r\cos\theta\cos\phi & -r\sin\theta\sin\phi \\ \sin\theta\sin\phi & r\cos\theta\sin\phi & r\sin\theta\cos\phi \\ \cos\theta & -r\sin\theta & 0 \end{bmatrix} \tag{4.14b}$$

$$J = r^2\sin\theta \tag{4.14c}$$

$$g_{ij} = \begin{bmatrix} 1 & 0 & 0 \\ 0 & r^2 & 0 \\ 0 & 0 & r^2\sin^2\theta \end{bmatrix} \tag{4.14d}$$

$$\Gamma^r = \begin{bmatrix} 0 & 0 & 0 \\ 0 & -r & 0 \\ 0 & 0 & -r\sin^2\theta \end{bmatrix} \tag{4.14e}$$

$$\Gamma^\theta = \begin{bmatrix} 0 & 1/r & 0 \\ 1/r & 0 & 0 \\ 0 & 0 & -\sin\theta\cos\theta \end{bmatrix} \tag{4.14f}$$

$$\Gamma^\phi = \begin{bmatrix} 0 & 0 & 1/r \\ 0 & 0 & \cot\theta \\ 1/r & \cot\theta & 0 \end{bmatrix} \tag{4.14g}$$

After applying the transformation, the physical meaning of the additional terms is now more obvious. In fact, they are akin to forces appearing in a rotating frame of reference. For example, the equivalent centripetal acceleration term V^2/r is recovered by inserting (4.14e) into (4.2b). Similarly, the other terms appearing in the polar (4.14f) and azimuthal (4.14g) momentum equations act as Coriolis-like forces.

Lastly, the conical flow assumption is applied by forcing $\partial/\partial r = 0$ when expanding the divergence terms in (4.2). This last trick is the key to reduce the three-dimensional Navier-Stokes system to a geometrically two-dimensional case.

4.2 Discretization of the Governing Equations

The equations are discretized using a finite volume method. The finite volume framework already implemented in the CHAMPS solver is reused and extended to account for the additional terms and altered fluxes of (4.2). The computational domain used for the simulation is shown in Figure 4.1. This approach can be considered as a mix between the sheared-cell and β approaches of Figure 2.6. It is however important to stress that a purely two-dimensional computational domain is defined.

4.2.1 Convective Fluxes

According to the finite volume paradigm, the convective and inertial terms are discretized according their integral formulations.

$$\frac{d}{dt}\int_{\Omega_\xi} J\mathbf{W}dV + \oint_{\delta\Omega} J(\mathbf{F}_c - \mathbf{F}_v)dA = \int_{\Omega} J(\mathbf{S}_c + \mathbf{S}_v)dV \tag{4.15}$$

with $\mathbf{W}$, $\mathbf{F}$ and $\mathbf{S}$ are respectively the conservative variables, the fluxes and the source terms, while V and $\mathbf{A}$ are the volume and surface vector of control volume Ω.

$$\mathbf{W} = \begin{Bmatrix} \rho \\ \rho U \\ \rho V \\ \rho W \\ \rho E \end{Bmatrix} \tag{4.16a}$$

$$\mathbf{F_c} = \begin{Bmatrix} \rho U^* \\ \rho U^* U + p n_x^j \\ \rho U^* V + p n_x^j \\ \rho U^* W + p n_x^j \\ \rho U^* H \end{Bmatrix} \tag{4.16b}$$

$$\mathbf{S_c} = \begin{Bmatrix} 0 \\ \rho r(U^2 + W^2 \sin^2\theta) + \frac{2p}{r} \\ \rho\left(W^2 \sin\theta\cos\theta - 2\frac{UV}{r}\right) + \frac{p\cot\theta}{r} \\ -2\rho\left(UW\cot\theta + \frac{VW}{r}\right) \\ 0 \end{Bmatrix} \tag{4.16c}$$

where $U^* = U_i n_\xi^i$.

The cancellation of the flux term in the r direction is applied by setting the surface vector as $d\mathbf{A}_\xi = \mathbf{n}_\xi dA_\xi = (0, dA_{\xi,\theta}, dA_{\xi,\phi})$ (assuming the normal vector is still of unit length). Modifications to the Roe dissipation flux and spectral radii must also be taken into account, as the resulting eigenvalues of the convective flux Jacobian are altered.

4.2.2 Source Term

The extra terms appearing in the non-Euclidean formulation of the Navier-Stokes system accumulate in the form of a source term. The convective source terms affecting the momentum equations are discretized implicitly as suggested in [52] in the case of stiff source terms. The

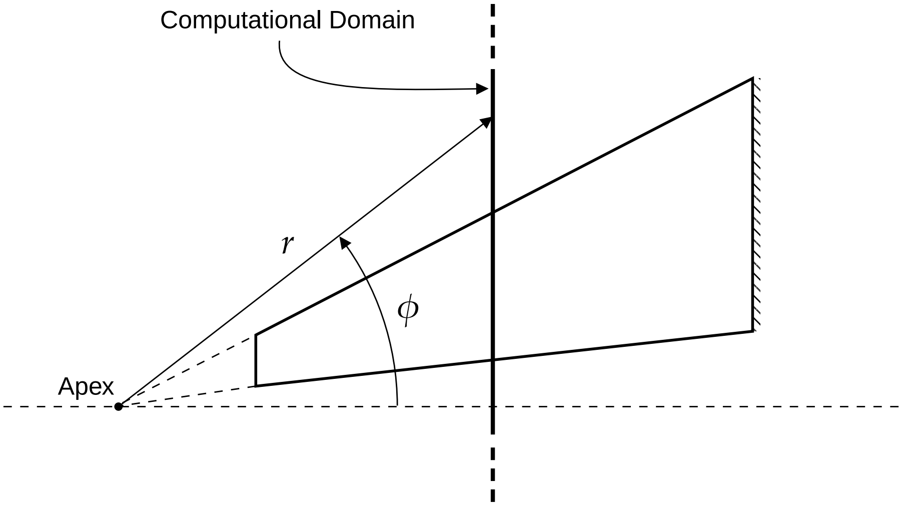

Figure 4.1 Computational domain used for 2.75D simulations. The polar angle θ is defined perpendicular to the page.

Jacobian of this term is defined as follows.

$$\frac{d\mathbf{S}^c}{d\mathbf{W}} = \frac{d\mathbf{S}^c}{d\mathbf{U}}\frac{d\mathbf{U}}{d\mathbf{W}} = \frac{1}{r}\begin{bmatrix} 0 & 0 & 0 & 0 & 0 \\ A & B & C & D & 2(\gamma-1) \\ \frac{E}{2} & F & G & \frac{H}{2} & (\gamma-1)\cot\theta \\ I & J & -2w & K & 0 \\ 0 & 0 & 0 & 0 & 0 \end{bmatrix} \tag{4.17}$$

with

$$q \equiv u^2 + r^2v^2 + r^2w^2\sin^2\theta \tag{4.18a}$$

$$A \equiv \gamma q - rq \tag{4.18b}$$

$$B \equiv 2u(-\gamma + r^2 + 1) \tag{4.18c}$$

$$C \equiv 2r^2v(1-\gamma) \tag{4.18d}$$

$$D \equiv 2r^2w(2-\gamma)\sin^2\theta \tag{4.18e}$$

$$E \equiv -r^2w^2\sin(2\theta) + 4ruv + (\gamma-1)q\cot\theta \tag{4.18f}$$

$$F \equiv -u(\gamma-1)\cot\theta - 2v \tag{4.18g}$$

$$G \equiv -rv(\gamma-1)\cot\theta - \frac{2u}{r} \tag{4.18h}$$

$$H \equiv rw(-\gamma r + r + 2)\sin(2\theta) \tag{4.18i}$$

$$I \equiv 2w(u\cot\theta + \frac{v}{r}) \tag{4.18j}$$

$$J \equiv -2rw\cot\theta \tag{4.18k}$$

$$K \equiv -\frac{2ru}{\tan\theta} - 2v \tag{4.18l}$$

In addition to stiffening the temporal scheme, the presence of a stiff source term can hinder the definition of the Roe dissipation flux. In fact, the presence of this source term affects the balance of the approximate Riemann solver by altering the strength of the waves [53]. Similarly, this term affects the treatment of the characteristic-based farfield boundary conditions used in subsonic flows. Both of these effects, are neglected in the scope of this work.

4.3 Results

In the goal of assessing the finite volume implementation of the spherical coordinates form of the Euler equations, simple canonical cases are considered.

4.3.1 Recovery of Two-Dimensional Flow

In this first case, the recovery of two-dimensional flow solutions is investigated using the spherical form of the Euler equations. Indeed, by setting $r \to \infty$, the system of equations is expected to converge asymptotically to the standard two-dimensional formulation. In this limit case, $\mathbf{e}_r \to \mathbf{e}_y$, $\mathbf{e}_\theta \to -\mathbf{e}_z$ and $\mathbf{e}_\phi \to \mathbf{e}_x$. The geometry of interest is the NACA0012 at $M = 0.2$ and $M = 0.8$ where $r = 1 \times 10^6 c$. The solutions are compared with standard CHAMPS two-dimensional flow module.

As observed in Figure 4.2, the conical/spherical form of the Euler equations allows recovering two-dimensional flow when $r \to \infty$ and $\phi \to -\pi/2$. As the source term is very close to zero as r tends to infinity, similar convergence properties between the two solvers are observed.

4.3.2 Recovery of Infinite Swept Flow

Similarly, by setting $\phi \to -\pi/4$ and $r \to \infty$, the system of equations is expected to converge asymptotically to the infinite swept flow case with a sweep angle of 45 deg.

Once again, the 2.75D method recovers the infinite swept flow case when $r \to \infty$ and $\phi \to -\pi/4$ as observed in Figure 4.3. However, higher discrepancies are observed for higher angles of attack. The source of this discrepancy was found to be in the discretization of

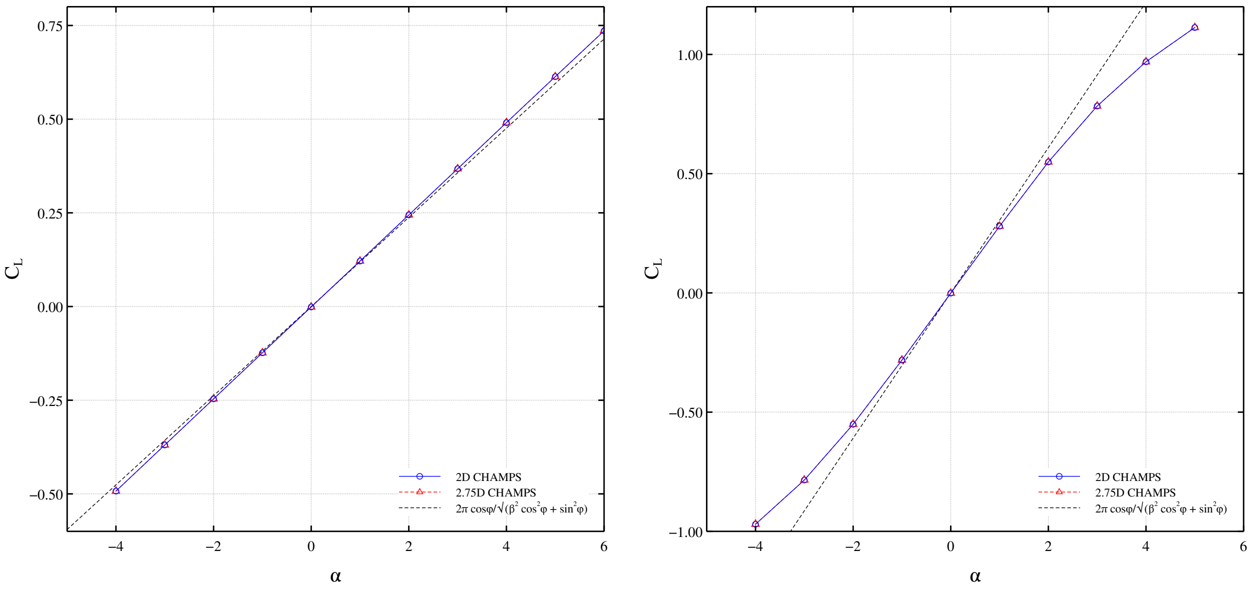

(a) $M = 0.2$ (b) $M = 0.8$

Figure 4.2 Lift polar for the NACA0012 obtained with the spherical form of the Euler equations when $r \to \infty$ and $\phi \to -\pi/2$ to recover two-dimensional flow

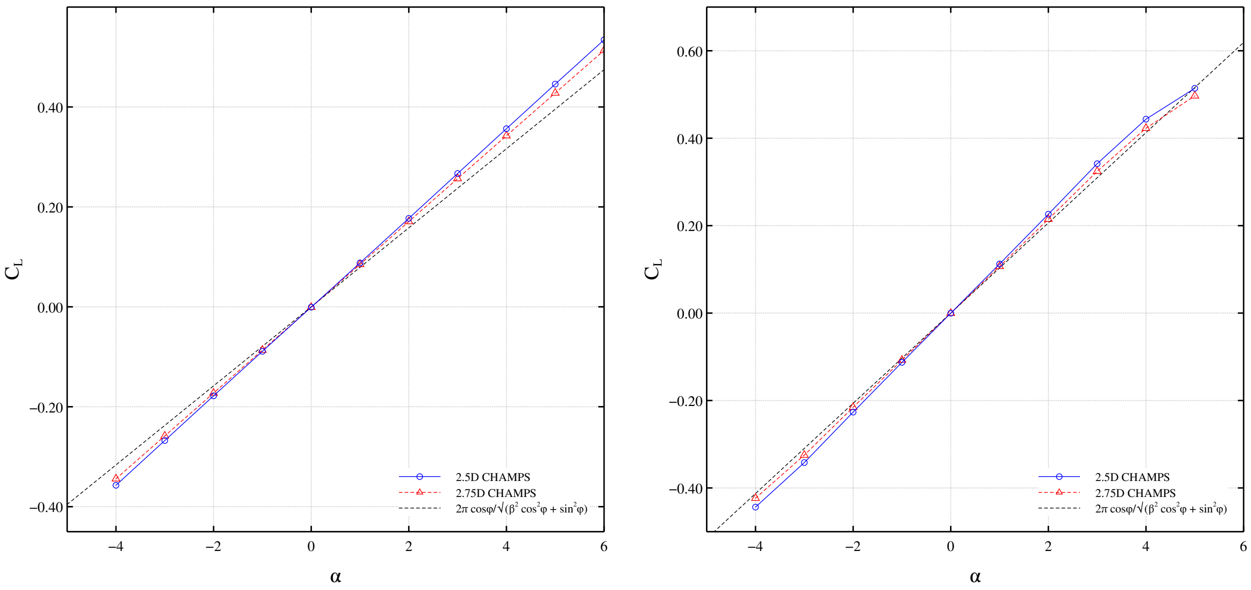

(a) $M = 0.2$ (b) $M = 0.8$

Figure 4.3 Lift polar for the NACA0012 obtained with the spherical form of the Euler equations when $r \to \infty$ and $\phi \to -\pi/4$ to recover infinite swept flow the upwinding flux of the Roe scheme, where reorientation of the fluxes with the spherical coordinates metrics introduces additional dissipation (see Section 4.2.2). Furthermore, the expected constant crossflow along the swept isobars is recovered for this case, as shown in Figure 4.4.

4.3.3 Discussion Concerning Tapered Cases

Unfortunately, although the limit cases have been recovered, the application of the solver to any geometries of non-negligible taper leads to either highly nonphysical results or to penalizing convergence problems. As mentioned previously, the main issue of this 2.75D approach is the treatment of the conical boundary conditions far from airfoil's surface. As a result, the solver is unable to recover the expected flow topologies. It is also possible that the source term as a leading role in the convergence of the solver when non-negligible taper is introduced. Investigating the impact of the source term on the upwinding of the Roe fluxes and on the characteristic-based boundary conditions in subsonic flow is a possible future research avenue. These facts however indicate that a 2.75D approach for hyperbolic solvers such as the Euler or RANS equations may not be suitable for most applications. Alternatives that could be considered in the scope of this work are as follows:

- Use/Define an empirically-defined distribution of the effective sweep angle along the span of the wing to capture the primary flow features. As it was previously observed, a reduced sweep near the wing root often leads to best agreement with higher fidelity methods.

- Introduce additional coupling terms between the NL-VLM and the RANS data generation so that the database generation procedure becomes *aware* of the presence of the aircraft. This could help introduce the reduction in crossflow caused by the proximity to a symmetry plane or a fuselage at the wing root.

- Replace 2.5D RANS by a coupled panel method and 2.75D compressible boundary layer approach. As boundary layers are mainly parabolic and thus do not require the resolution of the farfield, the 2.75D assumption is better defined.

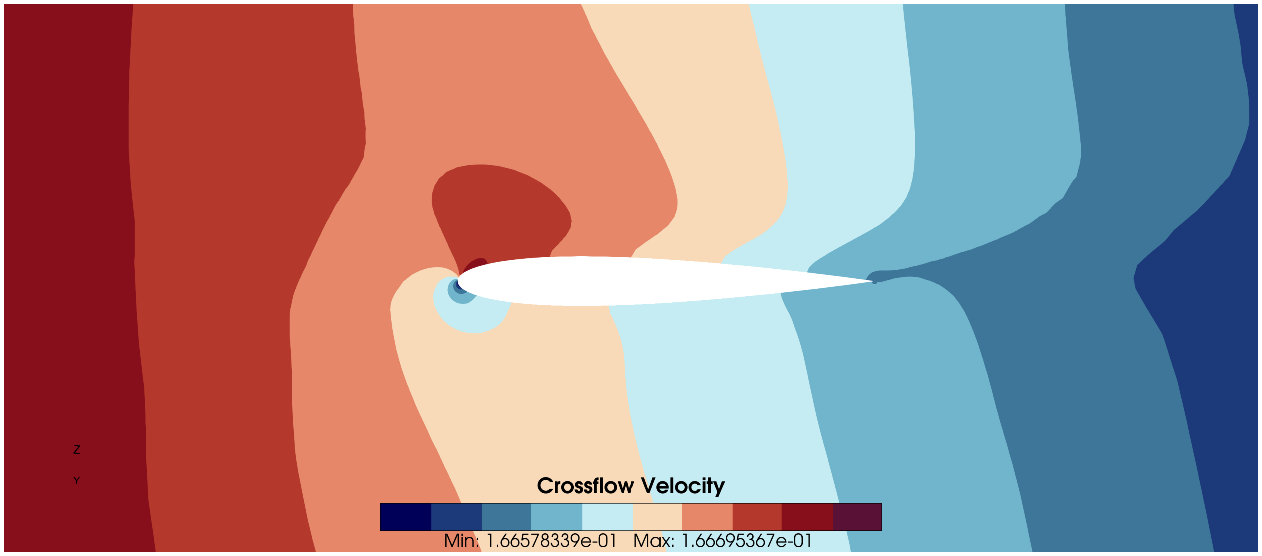

Figure 4.4 Constant crossflow velocity recovered by the 2.75D solver in spherical coordinates

CHAPTER 5 CONCLUSION

The precedent sections presented in this work detailed and investigated a medium-fidelity aerodynamic framework based on nonlinear potential flow. This section aims to summarize the observations and to highlight the perspective of such methods for preliminary design and analysis.

5.1 Summary of Works

The main objective of this work was to develop, to investigate and to put in application a medium-fidelity methodology for the analysis of general and complex aircraft geometries. Throughout the development of the solving procedure, a compromise between accuracy and computational efficiency was sought.

First, the introduction of additional aircraft components other than the main wing in a hybrid VLM-panel method approach was investigated in the goal of increasing the complexity of the cases to be modelled within the framework. It was shown that the coupled effects of such lifting and non-lifting systems can be captured adequately by the proposed approach. The inclusion of auxiliary lifting surfaces such as empennages and pylons showed non-negligible impacts on the spanwise loading of wings, and it was shown that potential flow solvers are able to capture such effects.

The hybrid potential flow framework was put to the test for various configurations of the CRM in varying flow conditions. First, it was shown that the expected accuracy of the NL-VLM for isolated wings was recovered for low-speed flows in near-stall conditions. Furthermore, the inclusion of fuselage and tailplane effects showed excellent agreement with RANS and wind tunnel measurements. In fact, most of the calculations performed in this work were in similar error margins as other state-of-the-art RANS solvers when compared to experimental data. Similar conclusions were drawn for the high-lift devices case, although the inclusion of slat brackets in the model led to discrepancies in regions of separated flow. The application of the model to transonic flow conditions also showed that the formulation used in this work can predict quite accurately the increment in the drag coefficient caused by the addition of nacelle and pylon components. However, poor prediction of the shock location and strength was observed near the root of the wing, where the 2.5D hypothesis failed, leading to a poor estimation of the absolute values of the drag and pitching moment coefficients.

An attempt at introducing taper effects in the generation of the local database was detailed in the precedent sections. Although the solver was able to recover limit cases, such as the two-dimensional and infinite swept flow cases, prohibiting convergence issues were observed as soon as non-negligible taper was introduced. Consequently, an alternative approach may have to be considered for increasing the fidelity and accuracy for highly tapered wings.

The overall results obtained throughout this work highlights the potential of the framework for preliminary design and analysis of complex aircraft geometries. The reasonable accuracy and exceptional computational efficiency of the solver makes it also a promising candidate for coupled full-aircraft multi-physics simulations, where higher fidelity methods show limited applicability in an industrial context. In fact, the absence of volumetric meshing makes the method ideal for cases where changes in geometry are expected, as three-dimensional automatic re-meshing can lead to poor quality meshes and thus to suboptimal solutions.

5.2 Limitations

As mentioned during the analysis of the validation cases, simplifying assumptions have been made in order to keep the complexity and execution time of the solver low. These simplifying assumptions however introduced discrepancies in some of the results. The pinpointed limitations are as follows:

- The fixed-wake approach lead to poorer agreement with high-fidelity solutions for the wing-tail interaction case. Although the downwash created by the main wing was well captured, nonlinear interactions near stall lead to less accurate predictions, especially of the pitching moment.

- Since singularity-based methods are elliptical, the simulation time necessary for meshes of increasing size is proportional to the square of the number of panels. This makes the simulation of complex aircraft configurations considerably more expensive than isolated wings. It however still remains several orders of magnitudes faster than an equivalent three-dimensional RANS simulation.

- Viscous effects for thick bodies such as fuselages are taken into account using basic semi-empirical formulas. Consequently, complex boundary layer interactions are not solved for nor modelled.

- The sectional RANS simulations composing the viscous database are generated in open air. Consequently, the influence of other aircraft components on the local velocity field is ignored.

5.3 Future Research

An assessment of the aforementioned limitations could help understand the potential of the framework for future applications. Some avenues of research in this regard are as follows:

- Remove the assumption of fixed-wake in order to account for complex wing-tail interactions. A hybrid vortex particle approach as used in [54] could be considered as a way to achieve a robust and physically-accurate solver. However, as the problem would become unsteady, an increase in the computational cost is expected.
- Introduce viscous effects of fuselage using a coupled panel-method/boundary-layer approach. This could potentially be beneficial for capturing complex viscous interactions, such as at wing-fuselage junctions.
- Include the sectional RANS simulations in the nonlinear potential flow solver in a tightly-coupled manner, i.e. by generating the sectional data as part of the iterative NL-VLM process. This way, the actual velocity field perturbations induced by the aircraft could be included in the RANS simulations so that additional three-dimensional effects could be captured. This research avenue could be an interesting successor to the 2.75D approach.

REFERENCES

[1] D. Lee, D. Fahey, and al, “The contribution of global aviation to anthropogenic climate forcing for 2000 to 2018,” *Atmospheric Environ.*, vol. 244.

[2] J. D. Anderson, *Fundamentals of Aerodynamics.* McGraw-Hill, 2001.

[3] I. M. Kroo, “Minimum Induced Drag of Canard Configurations,” *Journal of Aircraft*, vol. 19, no. 9, pp. 792–794, Sep. 1982.

[4] J. Weissinger, “The Lift Distribution of Swept-Back Wings,” *Zentrale fuer Wissenschaftliches Berichtswesen der Luftfahrtforschung des Generalluftzeugmeisters*, no. 1553, Mar. 1947.

[5] J. A. Blackwell, “A finite-step method for calculation of theoretical load distributions for arbitrary lifting surface arrangements at subsonic speeds,” Jul. 1969.

[6] J. Katz and A. Plotkin, *Low-Speed Aerodynamics.* Cambridge University Press, Feb. 2001.

[7] J. L. Hess and A. M. O. Smith, “Calculation of Nonlifting Potential Flow About Arbitrary Three-Dimensional Bodies,” *Journal of Ship Research*, vol. 8, no. 04, pp. 22–44, Sep. 1964.

[8] B. Maskew, *Program VSAERO Theory Document: A Computer Program for Calculating Nonlinear Aerodynamic Characteristics of Arbitrary Configurations.* National Aeronautics and Space Administration, 1987.

[9] A. E. P. Veldman, “New, quasi-simultaneous method to calculate interacting boundary layers,” *AIAA Journal*, vol. 19, no. 1, pp. 79–85, Jan. 1981.

[10] M. Drela and M. B. Giles, “Viscous-inviscid analysis of transonic and low Reynolds number airfoils,” *AIAA Journal*, vol. 25, no. 10, pp. 1347–1355, Oct. 1987.

[11] I. Tani, *A Simple Method of Calculating the Induced Velocity of a Monoplane Wing.* Aeronautical Research Institute, Tokyo Imperial University, 1934.

[12] J. C. Sivells and R. H. Neely, “Method for calculating wing characteristics by lifting-line theory using nonlinear section lift data,” Jan. 1947.

[13] W. R. Sears, “Some Recent Developments in Airfoil Theory,” *Journal of the Aeronautical Sciences*, vol. 23, no. 5, pp. 490–499, May 1956.

[14] J.-J. Chattot, “Analysis and Design of Wings and Wing/Winglet Combinations at Low Speeds,” in *42nd AIAA Aerospace Sciences Meeting and Exhibit.* Reno, Nevada: American Institute of Aeronautics and Astronautics, Jan. 2004.

[15] P. R. Spalart, “Prediction of Lift Cells for Stalling Wings by Lifting-Line Theory,” *AIAA Journal*, vol. 52, no. 8, pp. 1817–1821, Aug. 2014.

[16] C. E. Lan and J. B. Tseng, “Calculation of aerodynamic characteristics at high angles of attack for airplane configurations,” Feb. 1987.

[17] M. Parenteau, “Aerodynamic Optimization of Aircraft Wings Using a Coupled VLM-2.5D RANS Approach.”

[18] C. Van Dam, “The aerodynamic design of multi-element high-lift systems for transport airplanes,” *Progress in Aerospace Sciences*, vol. 38, no. 2, pp. 101–144, Feb. 2002.

[19] S. Gallay, “Algorithmes de couplage RANS et écoulement potentiel,” phd, École Polytechnique de Montréal, Feb. 2016.

[20] F. Plante, E. Laurendeau, and J. Dandois, “Stall Cell Prediction Using a Lifting-Surface Model,” *AIAA Journal*, vol. 60, no. 1, pp. 213–223, Jan. 2022.

[21] M. Parenteau and E. Laurendeau, “A transonic, viscous nonlinear frequency domain Vortex Lattice Method for aeroelastic analyses,” *Journal of Fluids and Structures*, vol. 107, p. 103406, Nov. 2021.

[22] M. Drela, *Flight Vehicle Aerodynamics.* MIT Press, Feb. 2014.

[23] D. Küchemann, “A Simple Method for Calculating the Span and Chordwise Loading on Straight and Swept Wings of any Given Aspect Ratio at Subsonic Speeds,” Aeronautical Research Council Reports and Memoranda, London, Technical Report 2935, 1952.

[24] S. Bourgault-Côté, S. Ghasemi, A. Mosahebi, and E. Laurendeau, “Extension of a Two-Dimensional Navier–Stokes Solver for Infinite Swept Flow,” *AIAA Journal*, vol. 55, no. 2, pp. 662–667, Feb. 2017.

[25] R. C. Lock, “An equivalence law relating three- and two-dimensional pressure distributions,” 1962.

[26] T. Zhao, Y. Zhang, H. Chen, Y. Chen, and M. Zhang, “Supercritical wing design based on airfoil optimization and 2.75D transformation,” *Aerospace Science and Technology*, vol. 56, pp. 168–182, Sep. 2016.

[27] Z.-M. Xu, Z.-H. Han, and W.-P. Song, “An improved 2.75D method relating pressure distributions of 2D airfoils and 3D wings,” *Aerospace Science and Technology*, vol. 128, p. 107789, Sep. 2022.

[28] P. Bradshaw, G. A. Mizner, and K. Unsworth, “Calculation of compressible turbulent boundary layers on straight-tapered swept wings,” *AIAA Journal*, vol. 14, no. 3, pp. 399–400, Mar. 1976.

[29] K. Kaups and T. Cebeci, “Compressible laminar boundary layers with suction on swept and tapered wings,” *Journal of Aircraft*, vol. 14, no. 7, pp. 661–667, Jul. 1977.

[30] H. P. Horton and H.-W. Stock, “Computation of compressible, laminar boundary layers on swept, tapered wings,” *Journal of Aircraft*, vol. 32, no. 6, pp. 1402–1405, Nov. 1995.

[31] T. Streit, G. Wichmann, F. Von Knoblauch Zu Hatzbach, and R. Campbell, “Implications of Conical Flow for Laminar Wing Design and Analysis,” in *29th AIAA Applied Aerodynamics Conference.* Honolulu, Hawaii: American Institute of Aeronautics and Astronautics, Jun. 2011.

[32] V. Liguori, F. Moens, J. Peter, and E. Laurendeau, “Aircraft fuselage effects on transonic wing pressures via Non-Linear Vortex lattice Method,” in *57th 3AF International Conference on Applied Aerodynamics 2022*, Toulouse, France, Mar. 2023.

[33] M. Parenteau, S. Bourgault-Cote, F. Plante, E. Kayraklioglu, and E. Laurendeau, “Development of Parallel CFD Applications with the Chapel Programming Language,” in *AIAA Scitech 2021 Forum.* VIRTUAL EVENT: American Institute of Aeronautics and Astronautics, Jan. 2021.

[34] D. Callahan, B. Chamberlain, and H. Zima, “The cascade high productivity language,” in *Ninth International Workshop on High-Level Parallel Programming Models and Supportive Environments, 2004. Proceedings.*, Apr. 2004, pp. 52–60.

[35] T. Melin, A. T. Isikveren, and M. I. Friswell, “Induced-Drag Compressibility Correction for Three-Dimensional Vortex-Lattice Methods,” *Journal of Aircraft*, vol. 47, no. 4, pp. 1458–1460, Jul. 2010.

[36] A. Kontogiannis and E. Laurendeau, “Adjoint State of Nonlinear Vortex-Lattice Method for Aerodynamic Design and Control,” *AIAA Journal*, vol. 59, no. 4, pp. 1184–1195, Apr. 2021.

[37] C. Le Pailleur and E. Laurendeau, “Towards using Medium-Fidelity Nonlinear Potential Methods for Full Aircraft Configurations,” Orléans, France, Mar. 2024.

[38] L. Prandtl, “Induced drag of multiplanes,” Feb. 1924.

[39] G. H. Vatistas, V. Kozel, and W. C. Mih, “A simpler model for concentrated vortices,” *Experiments in Fluids*, vol. 11, no. 1, pp. 73–76, Apr. 1991.

[40] A. A. Nikolski, *On Lift Properties and Induced Drag of Wing-fuselage Combination.* National Aeronautics and Space Administration, 1959.

[41] R. Dechter and J. Pearl, “Generalized best-first search strategies and the optimality of A*,” *Journal of the ACM*, vol. 32, no. 3, pp. 505–536, Jul. 1985.

[42] V. Liguori and E. Laurendeau, Private communication, 2025.

[43] M. Parenteau, “A Non-Linear Frequency Domain Potential Flow Model for Compressible, Transonic and Viscous Aeroelastic Analyses,” PhD Thesis, Polytechnique Montréal, May 2021.

[44] Sighard F. Hoerner, *Fluid-Dynamic Drag*, 1965.

[45] B. Chamberlain, “Making Parallel Computing as Easy as Py(thon), from Laptops to Supercomputers,” Apr. 2022.

[46] W. J. Mccroskey, “A critical assessment of wind tunnel results for the NACA 0012 airfoil,” Oct. 1987.

[47] F. Manie and J. Raynald, “Transonic Meaurements on the ONERA AFV D Variable Sweep Wing in the ONERA S2 MA Wing Tunnel,” AGARD Advisory Rept., Neuilly-sur-Seine, Tech. Rep. AR-138, 1979.

[48] D. S. Lacy and A. M. Clark, “Definition of Initial Landing and Takeoff Reference Configurations for the High Lift Common Research Model (CRM-HL),” in *AIAA AVIATION 2020 FORUM.* VIRTUAL EVENT: American Institute of Aeronautics and Astronautics, Jun. 2020.

[49] L. Wang, “5th AIAA CFD High Lift Prediction Workshop (HLPW-5),” Aug. 2024.

[50] J. H. Morrison, “6th AIAA CFD Drag Prediction Workshop,” Mar. 2021.

[51] D. Schwamborn, T. Gerhold, and R. Heinrich, “THE DLR TAU-CODE: RECENT APPLICATIONS IN RESEARCH AND INDUSTRY,” Netherlands, 2006.

[52] J. Blazek, *Computational Fluid Dynamics: Principles and Applications.* Elsevier, May 2001.

[53] R. Mohanraj, Y. Neumeier, and B. T. Zinn, “Characteristic-Based Treatment of Source Terms in Euler Equations for Roe Scheme,” *AIAA Journal*, vol. 37, no. 4, pp. 417–424, Apr. 1999.

[54] V. Proulx-Cabana, M. T. Nguyen, S. Prothin, G. Michon, and E. Laurendeau, “A Hybrid Non-Linear Unsteady Vortex Lattice-Vortex Particle Method for Rotor Blades Aerodynamic Simulations,” *Fluids*, vol. 7, no. 2, p. 81, Feb. 2022.